Anisotropic stress softening and viscoelasticity in rubber like materials and architectured materials

Marie Rebouah

UNIVERSITÉ DE GRENOBLE

THÈSE

Pour obtenir le grade de

DOCTEUR DE L'UNIVERSITÉ DE GRENOBLE

Spécialité : **Matériaux, Mécanique, Génie Civil, Electrochimie**

Arrêté ministériel : 7 août 2006

Présentée par

Marie REBOUAH

Thèse dirigée par **Gregory CHAGNON**

préparée au sein du **Laboratoire TIMC-IMAG**
et de **l'école doctorale IMEP2**

Anisotropic stress softening and viscoelasticity in rubber like materials and architectured materials

Thèse soutenue publiquement le **23 septembre 2014**,
devant le jury composé de :

M. Laurent CHAZEAU
Professeur, MATEIS, INSA de Lyon, Président
Mme. Estefania PENA
Professor, University of Zaragoza, Rapporteur
Mme. Julie DIANI
Directeur de recherche, PIMM, Arts et Metiers Paris Tech, Rapporteur
M. Erwan VERRON
Professeur, GEM, Ecole Centrale de Nantes, Examinateur
M. Gregory CHAGNON
Maître de conférence HDR, TIMC-IMAG, Université de Grenoble, Directeur de thèse

Abstract

This work thesis present a contribution to the modeling and understanding of filled silicone rubber and soft tissues. Rubber like materials parts are designed using finite element code in which more and more precise and robust constitutive equations are implemented. In general, constitutive equations developed in literature to represent the anisotropy induced by the Mullins effect present analytical forms that are not adapted to finite element implementation. The present paper deals with the development of a constitutive equation that represents the anisotropy of the Mullins effect using only strain invariants. The efficiency of the modeling is first compared to classical homogeneous experimental tests on a filled silicone rubber. Second, the model is tested on a complex structure. In this aim, a silicone holey plate is molded and tested in tension, its local strain fields are evaluated by means of digital image correlation. The experimental results are compared to the simulations from the constitutive equation implemented in a finite element code. Global measurements (i.e. force and displacement) and local strain fields are successfully compared to experimental measurements to validate the model.

Many rubber like materials present a phenomenon known as Mullins effect. It is characterized by a difference of behavior between the first and second loadings and by a permanent set after a first loading. Moreover, this phenomenon induces anisotropy in an intially isotropic material. A new constitutive equation is proposed in this paper. It relies on the decomposition of the macromolecular network into two parts: chains related together and chains related to fillers. The first part is modeled by a simple hyperelastic constitutive equation whereas the second one is described by an evolution function introduced in the hyperelastic strain energy. It contributes to describe both the anisotropic stress softening and the permanent set. The model is finally extended to soft tissues mechanical behavior that present also stress softening but with an initially anisotropic behavior. The two models are successfully fitted and compared to experimental data.

In this paper, an extension of two classical viscoelastic models adapted in large deformation for incompressible rubber like materials or soft tissues is proposed. These models are built by using a three dimensional homogeneization by means of a sphere unit approach. Thus several comparisons between classical formulations and homogeneization on a sphere unit formulation is proposed. An adaptation of those models to describe

anisotropy is proposed. Finally an extension of those models to take into account stress softening is described.

The main objective of this study is to generate anisotropic membranes stretched in their plane able to endure large deformations. In this perspective, different crenellated membranes were designed with a filled silicone rubber. The aim of this work is to build a constitutive equation which describes the mechanical behavior of such architectured membranes, by means of a simple decompostion of the strain energy.
Since a filled silicone is used to make the architectured membrane, some non linear effects influence also the mechanical behavior of the structure. The main phenomenon is the Mullins effect and must be taken into account in the modeling. An equivalent constitutive equation is built for the architectured membrane by taking into account the mechanical behavior of the silicone and the geometrical parameters of the crenellated membrane. Firstly, a constitutive equation is chosen to describe the core of the membrane. Second, this equation is adapted to the behavior of the crenels and thirdly a coupling term describing the interactions between the crenels and the core of the membrane is developed. The implementation of the equivalent constitutive equation into a finite element code is finally validated on experimental data.

Key words: Filled silicone, Mullins effect, permanent set, viscoelasticity, architectured materials,finite element implementation

Aknowledgement

This manuscript presents the work of three years of thesis that took place at the TIMC-IMAG laboratory of Grenoble and at the laboratory 3SR. I would like to thank all the peoples that permit me to do this work for three amazing years.

First, I thank all my jury's members. Pr Laurent Chazeau who agreed to be the president of the committee. A particular thank to my both reviewers, Pr Julie Diani for the rigorous review and all the interesting questions about the work I have done and the Pr Estephania Pena who made a long travel to participate as a jury member. I also thank Pr Erwan Verron who was the examiner and who had these two interesting questions that lead to a large discussion.

Of course, I thank Gregory Chagnon who was my only supervisor thesis. Thank you for all the things that you learned to me, all the discussions and your patience. I guess I was not every day so easygoing... Nevertheless I will enjoy these years working with you and also all your human qualities that make my day so nice. I obviously never done such a work without you. I hope that we will work again together.

I also would like to thank all the team that had to support me every day. First a great thank to Denis Favier who gives me so many valuables advises during me thesis. I also thank Nathanael Conesson who was always available if needed and ready to help and thank Thierry Alonso for its permanent good mood.

Thank you to all Phd student and post doctorant for the great ambiance among the team. First I would like to thank all the peoples whith who I shared my office: Sylvie I spend two amazing years with you thank you for everything and particularly for your smile and your kindness ! Thank you to Camille my MAM , for all the jokes that we share, thank to Vincent for the office and all the years that we spent laughing in the team and in the office and thank to Quentin to support me for this last year of thesis. And finally I also thank Gabriel (my favorite "petit bezo"), Christopher (don't be so mad) and Francois and Guilherme.

I also want to thank all the people who help for experimental tests and discussion during the thesis. Thank you to Francois Rouillard from the LRCCP, to Pierre Charier from Trelleborg and to Jean Benoit Le Cam for you advice and help.

Finally thank to all my family and friends that support me during all these years. My parents of course, my sister and brother and also Caro, Louise, Caro, Chou, Anthony, Mathieu, David,.... And thank you to Thierry whith who I shared these years at work and at home, you are always here for me...

Thank to all of those that were with me or close during this thesis and to all the peoples that I forgot to quote...

Contents

General introduction

The context

This thesis work, was realized thanks to a ministerial grant aid at the TIMC-IMAG "Techniques de l'Ingénierie Médicale et de la Complexité - Informatique, Mathématiques et Applications, Grenoble" (TIMC-IMAG) laboratory. It took place in the "Biomedical and Mechanical engineering of Materials" (BioMMat) team, where the main area of research is the study of living materials and materials that present biomedical applications (NiTi shape memory alloys and rubber like materials). In this context, this thesis work focuses on soft materials, and in particular on rubber like materials.

The objectives

The development of new prosthesis or scaffolds is a current challenge. To mimic the living soft materials, most of these implants are made of biocompatible rubber like materials as the silicone. If the mechanical behavior of these materials is well known and predicted, the prosthesis design becomes more efficient. In this way, this thesis work aims to propose new constitutive equations that can take into account the non linear phenomena that are observed in soft materials submitted to large deformations. To that aim experimental, theoretical and numerical studies are lead on rubber like materials. In this research field, researchers currently start on rubber like materials before to extend the in-house knowledge to soft tissues. Firstly the use of different rubber like materials allows to isolate each phenomenon and to build robust models before using it on living materials. Indeed it enables to take into account stress softening, induced anisotropy, permanent set and viscous effects in models.
Moreover, having a good set of experimental data on rubber like materials is easier. On the opposite, the experimental data on soft tissues are more difficult to set up and the number of samples is often limited. Thus, the non linear phenomena are more difficult to be properly quantified. Besides, due to the presence of fibers in their structure inducing an initial anisotropy soft tissues present rarely an isotropic behavior. In order to have

this other non-linear phenomenon considered it is proposed to use architecture rubber like materials.

The scientific content

To reach the aims of this thesis, the work can be divided in several parts. In this way, each chapter focuses on an objective.
The first section presents the rubber like materials and the soft tissues. A description of their structure is proposed, and first similarities are highlighted. Both materials are submitted to large deformations and cyclic loadings. Simple mechanical tests are performed on the materials and compared to classical literature observations. Both materials present a similar mechanical behavior and several non linear phenomena such as: stress softening, permanent set and viscoelasticity. The major difference between the both materials is that most of the soft tissues present an initially anisotropic behavior compared to rubber like materials. In this way, the main basis equation of a hyperelasticity framework are recalled, and the main modeling theories (micro mechanics based models or phenomenological models) are presented. Then a quick bibliography of the preexistent models is proposed. Finally, architectured materials are presented, first according to the soft tissues that are naturally considered as architectured due to their microstructure and then by means of geometrical assumption or by means of composites.
The Chapter 2 focuses on two dependent non linear phenomena: stress softening and induced anisotropy. To isolate these two phenomena, a filled silicone rubber (RTV3428) is used. Indeed, this material does not present permanent set or viscous effect at slow and moderate strain rates. Moreover, this material presents an initially isotropic behavior. The chapter presents an experimental study with classical mechanical tests and tensile tests according to different orientations to highlight the influence of the loading direction. Then a new model based on a micro spherical approach is proposed and validated on the experimental data. A numerical implementation of the model is also proposed to test the robustness of the model.
In Chapter 3, another non linear phenomenon is added to the previous proposed model : the permanent set. To validate the model experimental data are performed on a Hot Temperature Vulcanization (HTV) filled rubber that presents stress softening, induced anisotropy and permanent set. Then the model is extended to soft tissues and adapted to take into account the initial anisotropy of material.
Chapter 4 focuses on the viscoelasticity of the rubber like materials. In this way, a first part, presents a theoretical study to take into account the viscoelastic behavior of materials based on two main theories. Classical models of the literature are adapted to a microspherical approach and comparisons with classical formulations are proposed. The second section of this chapter proposes a comparison of several models extend to microspherical approach to experimental data performed on a Nitril Butadien Rubber (NBR). Stress softening, induced anisotropy and viscoelasticity are thus taken into account.
Finally, the chapter 5 presents two kinds of architectured materials. A geometrical architectured material made of filled silicone rubber RTV3428 and two microstructural architectured materials made of Thermoplastic Elastomer (TPE) or of filled silicone rubber

RTV3428 with preferential orientations of chains impose during the process. The microstructure of those material can be partially controlled to induce an initial anisotropy to the materials. In this way, all the non linear phenomena observed experimentally in the first section are taken into account in a model. All parts of the previous models are regrouped to take into account the global behavior of soft materials with initial isotropy in large deformation.

Chapter

1 Bibliography

Contents

1.1 Introduction

This thesis work focuses on the mechanical behavior of materials submitted to large deformations. All materials have different structures and thus a particular mechanical behavior that defines its functions and its applications. Large deformations are observed on

structural materials which are made of huge molecular arrangement, and they are called macromolecules for polymers. They are made up of many small, simple chemical units, joined together, they can exists naturally or being synthetically created. Among all the polymers, this study focus more precisely on rubber like materials. A second group of materials that can endured large deformations and that is made of long molecules are the soft tissues. They are composed of collagen fibers that confer them their mechanical behavior. Collagen are very long structural proteins often considered as fibers, when they are joined, and that award a mechanical resistance to the tissue. Rubber like materials and soft tissues present a lot of similarities that are highlighted throughout this bibliography and in the following chapters.
The aim of this chapter is to present both materials and their mechanical behavior in the view to build an efficient predictive model. Indeed, even if rubber like materials are widely used in many industrial applications their prediction is still an open issue. First, a brief description of the rubbers like materials and soft tissues is proposed. Then, simple mechanical tests are performed to highlight the mechanical behavior and the non linear phenomena associated to both materials. Similarities between both materials are pointed by means of the experimental observations. Then the basis of constitutive equations to represent the material behavior are recalled. Finally, a quick bibliography of the proposed models in literature to take into account the phenomena is presented.

1.2 Rubber like materials and soft tissues

1.2.1 Composition of the rubber like materials and Network

Rubber like materials are widely used in industrial applications such as car, aeronautics or civil engineering. More and more industries get interest into a better understanding and modeling of the mechanical behavior of such materials. The Natural Rubber (NR) is one of the most important elastomer used in the industry. It is extracted from the Hévéa Brasilien tree, which is principally cultivated in Asia and Africa. Since the second World War, the synthetic rubbers have been developed, thus many industrial applications use also synthetic ones as Styrene Butadien Rubber (SBR), Nitrile Butadiene Rubber (NBR) or Ethylene Propylene Diene Monomer (EPDM) for example. Even if the composition of synthetic elastomer and NR are different, the structure is similar. Indeed, polymers materials are composed of a particular atomic group that can be denoted as (A), this basic unit is called structural unit or monomer unit. These units are repeated many times and take the form (A-A-A-A-) to create a macromolecule. The numbers of unit in a sequence defined the degree of polymerization, usually a material is called a polymer for a degree superior at 100 units. Different monomers can exist in a same structure, in this case the obtained macromolecule is a copolymer. All the materials used in this work contain fillers, that means that monomer chains are also linked to fillers, and that the mechanical behavior is different from an unfilled rubber [Mullins, 1948; Rigbi, 1980]. Most of the rubber like materials are organic compound, the macromolecule is made of carbonated chain, nevertheless some are inorganic. For instance, for the silicone, which is mainly used in this thesis work, the macromolecule is made of Silicon-Oxygen (Si-O) chain. Even if

their composition is different these materials present still a similar mechanical behavior. A basic representation of these material is represented in Fig.1.1, where it is considering that chains can be linked either to other chains either to fillers.

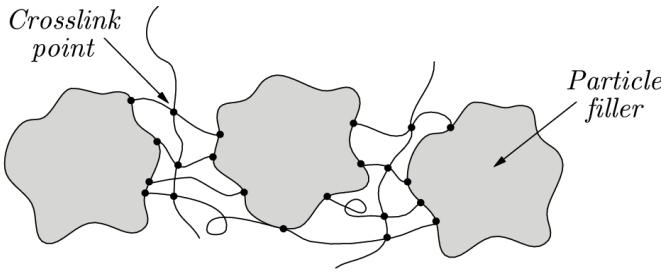

Figure 1.1: Representation of filled rubber like material with chains linked to chains and chains linked to fillers. [Machado, 2011]

1.2.2 Description of soft tissues

Soft tissues are composed of several layers, each one of these layers have different compositions. It is considered that there exists four typical tissues: epithelial tissue, connective tissue, muscular tissue and neuronal tissue [Marieb and Hoehn, 2010]. For the mechanical studies on soft tissues the connective tissues are often considered as the most important from a mechanical point of view [Epstein and Munderloh, 1975; Marieb and Hoehn, 2010; Natali *et al.*, 2009]. They are composed of cells and of extra cellular matrix. The extra cellular matrix is composed of ground substance and of three types of fibers: collagen, reticular and elastic fibers. Collagen fibers are much important than other particularly because of their large size and represent most of the mechanical behavior. The reticular fibers, which are thin collagen fibers with different chemical properties, allow to create ramifications with the collagen fibers. Finally the elastic fibers mainly composed of elastin present a purely elastic behavior and are also linked to the collagen fibers. The elastic properties of a soft tissues are mainly due to these fibers.
For instance, Fig.1.2 represents an arterial wall made of three layers. The intima consists of a single layer of endothelial cells, this layer is very thin for a healthy subject and its contribution to the mechanical behavior can be neglected. Then the media, which is a connective tissue, is a complex three-dimensional network of smooth muscle cells, elastin and oriented collagen fibrils form helix. This structure rearrangement is very important from a mechanical point of view. Finally, the last layer of the arterial wall is the adventia, composed of cells that product collagen and elastin. Collagen fibrils, that regroup to create collagen fibers, are also arranged in helical structure. This layer is mechanically important for high pressure [Holzapfel *et al.*, 2000]. For a more detailed review of mechanical characteristic of arterial component see for example [Rhodin, 1980; Silver F.H. and Buntin, 1989]
Other tissues, as esophageal [Natali *et al.*, 2009] are composed of several layers: mucosa, submucosa, muscularis externa and adventia as represented in Fig1.3. As for the arteries, these layers present all a different function and a different mechanical behavior. The ad-

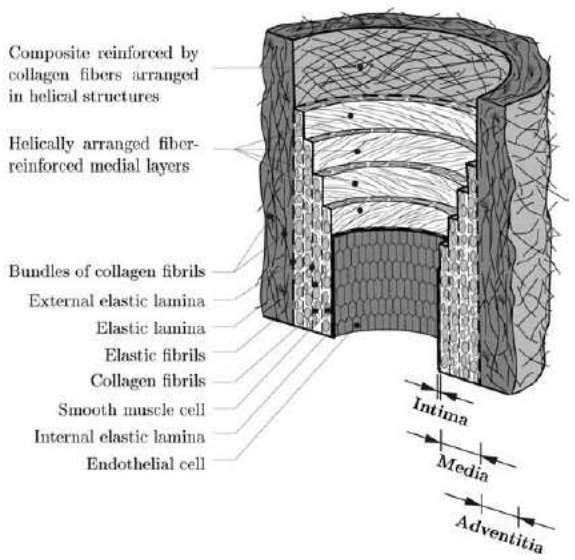

Figure 1.2: Representation of an arterial wall, Holzapfel *et al.* [2000]

ventia is similar to the one of the arterial wall, the mucosa is mostly composed of epithelial cells and the muscularis externa of muscle cells. For oesophageal tissues the submucosa (connective tissue) is the layer that presents the most mechanical resistance due to very high number of collagen fibrils that regroup into thick fibers. The fibers are also arranged according to a helix and two main directions of fibers can be defined. It is important to note that there exist different types of collagen, some are more resistant than other, according to the type of collagen presents in the studied tissue. For instance collagen is also present in cartilage and bones [Lakes, 1993].
Only two types of soft tissues have been presented, but the composition is similar for many other tissues. In the following parts, the structure of soft tissue will be simplified, thus it is considering that a soft tissue can be represented only by collagen fibers that allow a reinforcement of the structure in a matrix. The orientation of the fibers in the matrix induces an initial anisotropy.

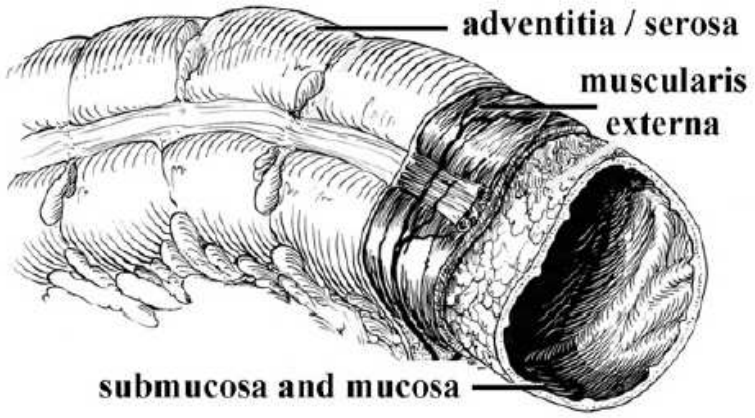

Figure 1.3: Representation of oesophageal tissue, [Natali *et al.*, 2009]

1.3 Mechanical behavior: experimental observations

1.3.1 Hyperelasticity and cyclic behavior

Mechanical behavior of soft tissues and rubber like materials present similarities. The most important, are that the materials are characterized by the ability to endure large deformations and present a highly non linear response. Their behaviors are thus represented by hyperelastic laws. It is proposed in this part to highlight the non linear effects endured by both materials by means of experimental observations. First, the mechanical behavior of both material is represented when they are submitted to large deformations and cyclic loadings. The Fig.1.4(a) highlights the mechanical behavior of a Hot Temperature Vulcanization rubber like material for a cyclic tensile test and the Fig.1.4(b) highlights the mechanical behavior for two orthogonal samples of aortic porcine arteries submitted to a cyclic tensile test [Rebouah, 2011]. For both materials, the Cauchy stress endured is represented in function of the elongation λ, which represents the actual length of the sample over its initial length. Several phenomena can be observed for both materials: the stress softening, the permanent set, initial anisotropy and hysteresis. Each one of these phenomena are more precisely defined in the following sections.

1.3.2 Initial isotropy or anisotropy

A first major information that can be obtained from tensile tests on these materials is to define if they are initially isotropic or anisotropic. Indeed, the behavior of rubber like materials depends on their manufactured. For instance, many industrial rubber like materials present an initially anisotropy due to their manufactured in calendared plate [Laraba-Abbes, 1998; Robisson, 2000; Diani *et al.*, 2004]. In this section, a Hot Temperature Vulcanization filled rubber is studied, its process does not induced initially anisotropic behavior.

However, most of the soft tissues present an initially anisotropic behavior due to the oriented collagen fibers that composed the tissue. Arteries are one of the most studied tissue and many authors highlighted their initial anisotropy [Holzapfel *et al.*, 2000; Raghavan

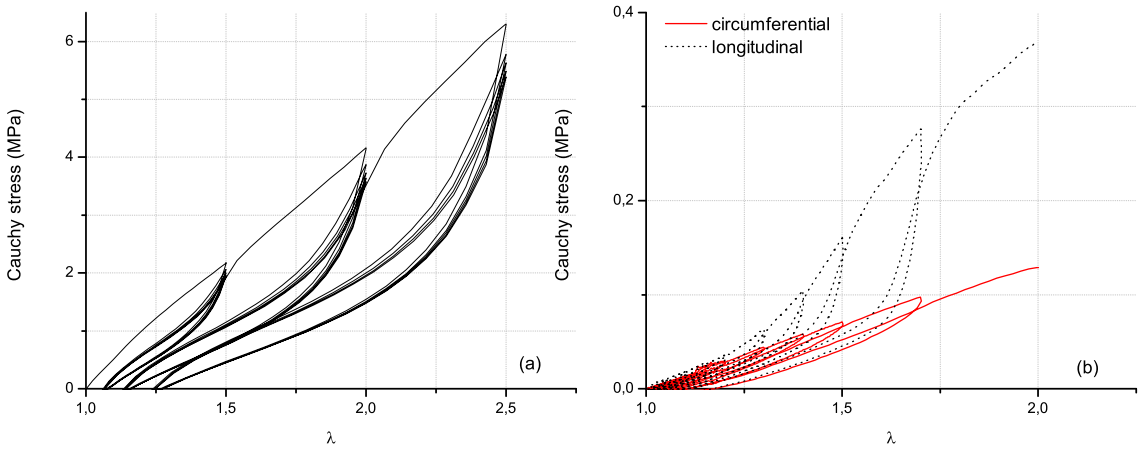

Figure 1.4: Stress-Strain curve of a Hot Temperature Vulcanization (a) and on circumferential and longitudinal porcine arteries samples (b)

et al., 1996; Zulliger *et al.*, 2004; Vande Geest *et al.*, 2006; Maher *et al.*, 2012], however many others tissues as oesophagus [Natali *et al.*, 2009], vaginal tissue [Peña *et al.*, 2011], etc... present also an initial anisotropy. Due to the presence of collagen fibers, it is rare to find soft tissues that are initially isotropic, excepted for instance for brain tissue [Miller and Chinzei, 1997; Kaster *et al.*, 2011]. Fig.1.4(b) highlighted the mechanical behavior for two orthogonal samples of porcine arteries, as show in literature it appears that this soft tissue presents an initial anisotropy.

1.3.3 Stress softening

The performed cyclic test presented in Fig.1.4 permits to highlight another classical phenomenon observed in rubber like materials and soft tissues: the stress softening. It was observed for the first time by Bouasse and Carrière [1903] and then strongly studied by Mullins [1948, 1969] and is now commonly called the Mullins effect. For both material it appears that there is a stress softening after the first loading. This phenomenon can be characterized by four main properties:

- The stiffness of a material decreases after the first loading for strain state inferior to the maximal strain imposed during the first loading.
- The material is not softened for strain state superior to the first loading, indeed once the material overtake the maximal strain reached during the first loading, the curve comes back to the primary loading.
- Most of the softening is obtained for the first cycle, it is often considered that after three or four cycles the mechanical behavior is stabilized.
- After the first cycle and near to the maximal strain reached during the first cycle the material presents a stress hardening before coming back on the primary curve.

In this thesis work, it is considered that the stress softening occurs between the first and the second loading. Many authors studied this phenomenon, and the literature is very well

documented, especially for rubber like material [Gurtin and Francis, 1981; Simo, 1987; Miehe, 1995; Ogden and Roxburgh, 1999; Chagnon, 2003; Diani *et al.*, 2009; Machado, 2011; Merckel, 2012]. Most of soft tissues present also an important stress softening as experimentally observed by Alastrué *et al.* [2008]; Natali *et al.* [2005]; Calvo *et al.* [2009]; Peña and Doblaré [2009]; Peña *et al.* [2011]; Maher *et al.* [2012].
Another important point is that, many new experimental data are proposed in the literature to emphasize that the Mullins effect is strongly anisotropic [Muhr *et al.*, 1999; Park and Hamed, 2000; Pawelski, 2001; Besdo and Ihlemann, 2003; Laraba-Abbes *et al.*, 2003; Diani *et al.*, 2006a; Hanson *et al.*, 2005; Itskov *et al.*, 2006; Machado *et al.*, 2012b; Dorfmann and Pancheri, 2012; Lion *et al.*, 2013; Diani *et al.*, 2006a; Merckel *et al.*, 2013, 2012]. Indeed, successive tensile test according to different orientations highlight that the Mullins effect induces anisotropy.

1.3.4 Permanent set

According to Fig.1.4(a) for a Hot Temperature Vulcanization filled rubber like material and Fig.1.4(b) for porcine arteries, it appears that both materials present a permanent set. Indeed, when a material is submitted to large deformations it is very common to observe experimentally a residual strain. However this residual strain can be considered in two different ways. A part that is considering as permanent and that could not be totally recovered in time. The second part of the residual strain is due to viscous effect and can be easily recovered in time. The amount of permanent set depends on several parameters as presented in several studies [Lion, 1996; Dorfmann and Ogden, 2004; Diani *et al.*, 2009]:

- The amount of fillers in the material for a rubber like materials if a filled rubber like material is considered. The composition of the connective tissue, the orientation of collagen fibrils and their type for a soft tissue.
- The maximal strain state reached during the loading for both materials.
- The strain rate applied to the material when it presents viscous effects. More the strain rate applied is important more the residual strain is important too.

Even if the amount of fillers influence the amount of residual strain, there exists also some rubber like materials, as for example the Room Temperature Vulcanization 3428 filled silicone rubbers that presents no residual strain as presented in Fig.1.5. The permanent set for soft tissue has also been observed experimentally, the damages that the tissues have endured induce the permanent set observed, most of the observation are similar to the rubber like materials [Peña, 2011; Maher *et al.*, 2012]. Nevertheless the recovery of the tissue is most difficult to evaluate since most of the experimental data are lead on ex vivo samples.

1.3.5 Viscoelastic behavior

After the initial anisotropy, the Mullins effect and the permanent set, one of the last phenomenon observed for rubber like materials and soft tissues is the viscoelasticity. Indeed,

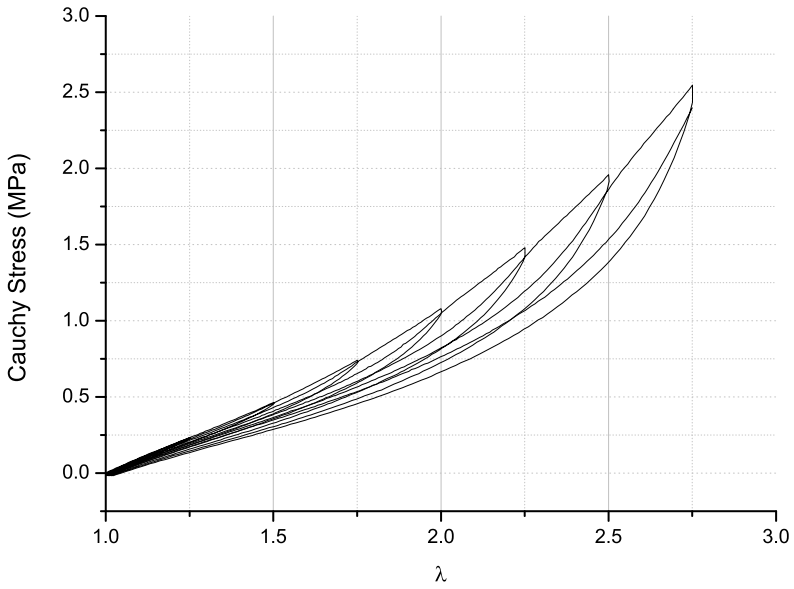

Figure 1.5: Cyclic stress-strain curve on a RTV3428 filled silicone

the viscoelasticity of a material is characterized by several phenomena. To highlight them several tests can be carried out. First the Fig.1.6 highlights the viscoelastic behavior of a NBR submitted to a cyclic tensile test at different strain rates. It appears that the mechanical behavior of the material is sensitive to the strain rate applied. More the strain rate is important more the stress state reached is important for a same strain state. In the same way, it also appears that the viscous effects influence also the permanent set. For the same imposed loading but at different strain rate the permanent set is different. More the strain rate is important more the permanent set is important too. The Fig.1.7(b) represents the same loading on the same material at a strain rate of $0.01s^{-1}$. This curve permits to highlight the viscous effects during cyclic loading. There is an important stress softening between the first and the second loadings due to the Mullins effect and then the stress is decreasing for every following cycle due to viscous effects. The Fig.1.7(a) represents two loading cycles on the same material where relaxation time (30minutes) are imposed a different strain states. It appears that the stress decreases for each relaxation time until reached a stabilized stress. These points permit to define "equilibrium curves". Once again an important stress softening is observed between the first and the second loading due to Mullins effect and thus equilibrium curves for first and second loadings are different. It appears that the equilibrium curves are not overlapping it means that this material presents simultaneously an hysteretic behavior due to viscous effect (well highlighted in Fig.1.7(b)) and a permanent hysteretic behavior. The recovery is not completed in 30 minutes, nevertheless if the recovery time is enough long (several days), the material should not presented any permanent hysteretic permanent behavior. These experimental observations have also been tackled in literature as proposed by Tobolsky *et al.* [1944].

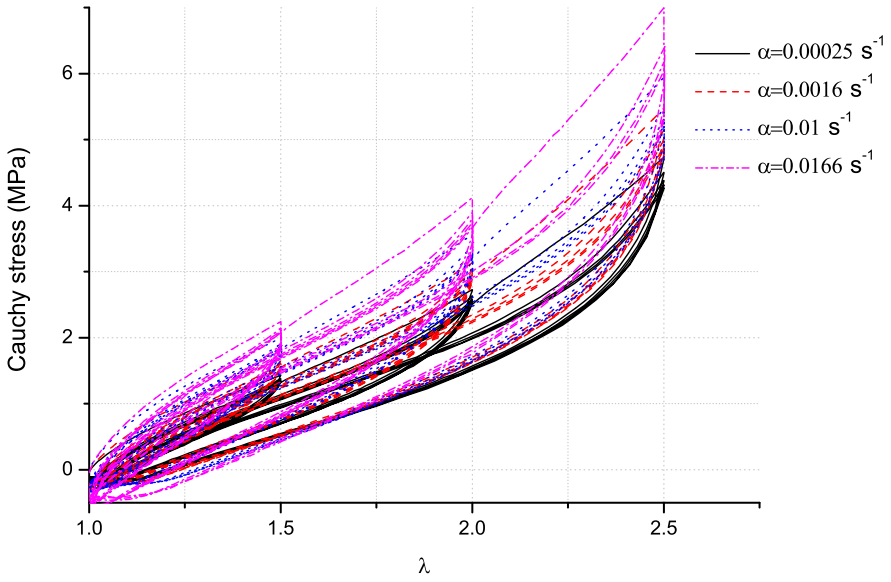

Figure 1.6: Cyclic stress-strain curve at different strain rate for a NBR (a)

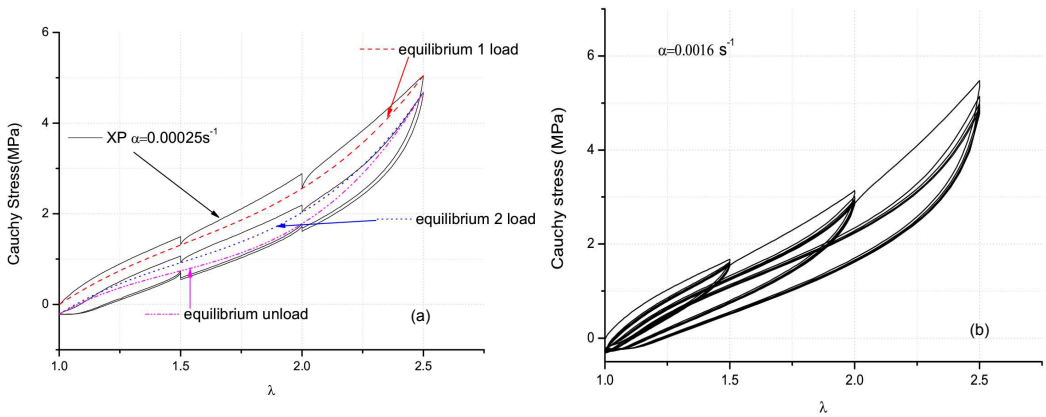

Figure 1.7: Cyclic loadings with imposed relaxation times of 30 minutes on a NBR at a strain rate of $0.00025s^{-1}$ (a). Cyclic loading on the NBR at a strain state of $0.01s^{-1}$ (b)

Viscoelasticity has also been observed for many soft tissues as iliac arterial segments [Papageorgiou and Jones, 1988], ligament and tendon [Pioletti *et al.*, 1998], internal organs Schwenninger *et al.* [2011], vaginal tissue [Peña *et al.*, 2010].

1.4 Material behavior modeling

This section presents the main points that permit to build a predictive model for both materials presented in last section. The main equations to respect, the useful tensorial expressions and the needed tools (the invariants of the deformation) are presented.

1.4.1 Hyperelastic law

As rubber like materials and soft tissues may undergo large deformations and present highly non linear strain stress responses, it is chosen to use the hyperelastic framework. All the constitutive equations presented in this work are developed in an incompressible framework. Models are expressed by means of the strain energy $\mathcal{W}$ from which the stress derives. The deformation gradient $\mathbf{F}$ allows describing the deformation of the material from its initial configuration to its current configuration. The strain energy is often expressed by means of a the strain tensor, either the right Cauchy Green strain tensor $\mathbf{C} = \mathbf{F}^T\mathbf{F}$ or the left Cauchy Green strain tensor $\mathbf{B} = \mathbf{F}\mathbf{F}^T$.
The stress endured by the material can be defined either on the initial configuration by means of the second Piola Kirchoff stress tensor $\mathbf{S}$, either on the current configuration by means of the Cauchy stress tensor $\boldsymbol{\sigma}$, or an intermediary configuration by means of the first Piola Kirchoff stress tensor $\boldsymbol{\pi}$. For an incompressible material and according to the law of thermodynamics, the Clausius Duhem inequality for an isothermal process permits to deduce the second Piola Kirchoff stress:

$$\mathbf{S} = 2\frac{\partial \mathcal{W}}{\partial \mathbf{C}} \tag{1.1}$$

Where p is the hydrostatic pressure. According to the incompressibility assumption the Cauchy stress can be expressed as:

$$\boldsymbol{\sigma} = 2\mathbf{F}\frac{\partial \mathcal{W}}{\partial \mathbf{C}}\mathbf{F}^T - p\mathbf{I} \tag{1.2}$$

Models are defined by the strain energy used, there exists as much expression of strain energy as authors working on the subject of the modeling of rubber like materials. Nevertheless two main theories can be distinguished: micro mechanic based model and phenomenological model.

1.4.2 Micro mechanical based models

The micro mechanics based models are built on physical assumptions. Authors described the mechanical behavior of a macromolecular chain. These models assumed that a strain energy can be defined for each chain. Indeed the material is considered as a network constituted of random long molecular chains. According to mechanics statistic, the entropy of a single chain can be defined by [Mayer and Mayer, 1940] as:

$$s = k\ln P(r) \tag{1.3}$$

where s is the entropy of a chain, k the Boltzmann's constant, P the probability of end to end chain distance and r represents the length of the chain segment. To determine the density probability two theories are proposed. First a Gaussian theory proposed by Guth and Mark [1934]:

$$P(r) = \frac{b^3}{\pi^{\frac{3}{2}}} \exp(-b^2 r^2) \tag{1.4}$$

Where $b^2 = 3/2Nl^2$ and N represents inextensible segments of length l. This probability depends only on the distance end to end of the chains. Treloar [1943] did the hypothesis that the chains deformed homogeneously in the material and finally deduced a simple strain energy

$$\mathcal{W} = \frac{1}{2} N k \theta (I_1 - 3) \tag{1.5}$$

This is the Neo Hookean model, where θ represents the temperature and I_1 is the first strain invariant (it will be explained in paragraph 1.4.3). Unfortunately, a Gaussian theory does not allow a good prediction of the mechanical behavior at large deformations.
The second theory, proposed by Kuhn and Grün [1942], define the probability end to end chain distance as a non Gaussian theory which takes into account the orientation between the different segment of chains and their maximal extension. At the opposite of the Gaussian theory the extension of the chains is limited.

$$\ln P(r) = N \left[\frac{r}{Nl} \beta + \ln \left(\frac{\beta}{\sin \beta} \right) \right] \tag{1.6}$$

Where $\beta = \mathcal{L}^{-1} \left[\frac{r}{\sqrt{Nl}} \right]$ and $\mathcal{L}$ is the Langevin function defined as

$$\mathcal{L}(\beta) = \coth(\beta) - \frac{1}{\beta} \tag{1.7}$$

The global strain energy is obtained by summation of all the contribution to be the full network [Treloar and Riding, 1979]. Wu and Giessen [1993] proposed also a full network by using a statistical distribution of the chains in every directions of space. Many models were built according to a specific number of considered chain directions, James and Guth [1943] proposed the three chains model oriented along the three principal directions where the density is equal for each directions. Then, Flory [1944] and Treloar [1946] proposed the four chains model where the four directions that linked the center of a tetrahedron and its summits are represented by the same density. Arruda and Boyce [1993] proposed the eight chains model where the density of the chains is equally distributed along the diagonal of a cube. Also based on micro mechanics, Heinrich and Kaliske [1997] proposed a model where they considered that a chain could move only into a virtual tube constitute by the other chains. Thus the chain is confined near its initial position. Later Miehe *et al.* [2004]; Göktepe and Miehe [2005]; Miehe and Göktepe [2005] used also the theory of tube constrained by considering that a single polymer chain in a constrained environment is defined by two micro-kinematic variables: the stretch of the chain and the contraction of the cross section of a micro-tube that contains the chain. The probability used is based on the one proposed by Doi and Edwards [1986]. It is to note that Miehe *et al.* [2004]; Göktepe and Miehe [2005]; Miehe and Göktepe [2005] proposed a repartition of chain in space by using a micro spherical approach. The micro spherical approach

is a mathematical formulation initially proposed by Bazant and Oh [1986] that used a repartition of i directions in space to integer a sphere. Many authors used this repartition to build hyperelastic laws [Diani *et al.*, 2006a; Machado *et al.*, 2012b; Merckel *et al.*, 2013; Lion *et al.*, 2013], and most of them used a 42 directions repartition. A quarter of the sphere discretized with 42 directions is represented in Fig.1.8. The Annex 1 presents these directions and the different weights associated. As any discretization, the approximation can induce an anisotropy, Gillibert *et al.* [2010] present a study of this induced anisotropy according to the number of directions use.

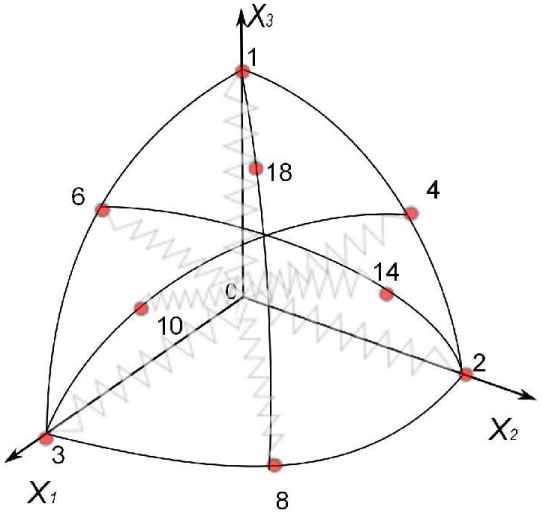

Figure 1.8: Representation of a quarter of the micro sphere with a spatial repartition of 42 directions proposed by Bazant and Oh [1986]

1.4.3 Phenomenological models

1.4.3.1 Isotropy

At the opposite of the micro mechanical based model the phenomenological model are built without any physical considerations. These models are based on mathematical formulations and depend mainly of the strain invariants.

$$I_1 = tr\mathbf{C} \tag{1.8}$$

$$I_2 = \frac{1}{2}\left[(tr\mathbf{C})^2 - tr\mathbf{C}^2\right] \tag{1.9}$$

$$I_3 = det\mathbf{C} \tag{1.10}$$

It is to note that in the incompressible assumption $I_3 = 1$. One of the most used model has been proposed by Mooney [1940] who proposed a strain energy as a linear function of the two first invariants:

$$\mathcal{W} = C_1(I_1 - 3) + C_2(I_2 - 3) \tag{1.11}$$

Where C_1 and C_2 are material parameters. It is to note that if $C_2 = 0$ this model is equivalent to the Neo Hookean.
Many others phenomenological models have been proposed, for a review it is proposed to refer to Charlton *et al.* [1994]; Seibert and Schöche [2000]; Chagnon [2003]; Vahapoglu and Karadeniz [2006]. Some comparisons of models are proposed in Boyce and Arruda [2000]; Marckmann and Verron [2006]. It is to note that phenomenological models can also be integer according to a micro spherical approach [Machado *et al.*, 2012b; Lion *et al.*, 2013; Machado *et al.*, 2014]. That means that any non linear spring can be put in a micro spherical approach and that this approach is note only applied to micro mechanic based models.

1.4.3.2 Definition of directions

Phenomenological models can also be used to describe initially anisotropic material behavior, for instance soft tissues. According to the biological composition of the tissue it is often considered that there exists two different oriented fibers, anyway, at least, there is on fiber direction. Let considered a parallel fiber reinforcement in a material. It is considered that the initial direction is defined by $\mathbf{A}^{(i)}$. Due to the deformation of the material, the orientation of the fiber is evolving in the deformed state. The current orientation is defined by:

$$\mathbf{a}^{(i)} = \mathbf{F}\mathbf{A}^{(i)}. \tag{1.12}$$

The introduction of these directions leads to the use of other invariants, able to describe what happens in direction $\mathbf{A}^{(i)}$. Thus for the same direction i the invariants I_4 and I_5 can be defined as:

$${I_4}^{(i)} = \mathbf{A}^{(i)}.\mathbf{C}\mathbf{A}^{(i)} \tag{1.13}$$

$${I_5}^{(i)} = \mathbf{A}^{(i)}.\mathbf{C}^2\mathbf{A}^{(i)} \tag{1.14}$$

These invariants only depends on one direction but there exists also invariants to take into account the coupling influence between two different directions of fibers i and j, according to Spencer [1971], two other invariant can be defined:

$$I_8 = \frac{1}{2}\left(\mathbf{C} : (\mathbf{A}^{(i)} \otimes \mathbf{A}^{(j)}) + \mathbf{C} : (\mathbf{A}^{(j)} \otimes \mathbf{A}^{(i)})\right) \tag{1.15}$$

$$I_9 = \mathbf{A}^{(i)}.\mathbf{A}^{(j)} \tag{1.16}$$

1.5 Non linear effects: a short bibliography

This section presents a short bibliography of some preexisting models proposed in the literature to predict hyperelastic behavior with non linear phenomena exposed in paragraph 1.3. Models adapted either to rubber like materials either to soft tissues to take into account the non linear phenomena observed experimentally are presented.

1.5.1 Initial anisotropy

Most of the models that treat initial anisotropy have been developed for soft tissues, nevertheless a major part of these models have been inspired by rubber like materials.

In the last few years, the understanding of the mechanical behavior of soft tissues gets improved [Lanir, 1979, 1983; Fung, 1993; Holzapfel, 2000] and thus the multiplication of predictive models appear.
A review proposed by Chagnon *et al.* [2014] presents most of the models used to predict the mechanical behavior of many types of tissues as for instance: anterior malleolar ligament [Cheng and Gan, 2008], muscles [Gras *et al.*, 2012], human trachea [Trabelsi *et al.*, 2010], cornea [Shin *et al.*, 1997], skin [Groves *et al.*, 2013] or gallbladder walls [Li *et al.*, 2013]. Due to the composition of soft tissues most of them present an initial anisotropy, nevertheless many authors decide to use isotropic approach considered as efficient for small strain or when the anisotropy is weak as for liver [Lister *et al.*, 2011], kidney [Hostettler *et al.*, 2010], balder and rectum [Boubaker *et al.*, 2009], and many others [Parente *et al.*, 2009; Azar *et al.*, 2001; Li and Kleinstreuer, 2006; Abraham *et al.*, 2011; Kaster *et al.*, 2011].
For anisotropic models, there exists different type of models. First, many authors based their constitutive equation on *"Fung"* models. These functions are build by using the components of the Green-Lagrange strain tensor. It consists in proposing strain energy densities that are decomposed into the contributions of each component with different weights. The reader can refer to Tong and Fung [1976]; Fung *et al.* [1979]; Chuong and Fung [1983]; Costa *et al.* [1996]; Choi and Vito [1990]; Humphrey [2002] for instance.
A second class of anisotropic model for soft tissue is the one obtained by the use of strain invariants. For those models, the directions of the fibers are often taken into account and the use of the fourth or fifth invariant is current. In this way, the strain energy is often decomposed into an isotropic part and an anisotropic part, this decomposition is similar to the one proposed to rubber like materials as proposed by Govindjee and Simo [1992]. Some models of this type can be found in Triantafyllidis and Abeyaratne [1983]; Peng *et al.* [2006]; Peña *et al.* [2009]; Basciano and Kleinstreuer [2009]; Bonet and Burton [1998]; Merodio and Ogden [2005].
Finally, soft tissue often present an important strain hardening and they are also often described by means of exponential functions. Those models are very used since they permit to well describe the stress hardening of soft tissues [Humphrey and Yin, 1987; Weiss *et al.*, 1996; Pinsky *et al.*, 2005; Holzapfel *et al.*, 2002; Natali *et al.*, 2003; Gasser *et al.*, 2006; Peña *et al.*, 2010] and many others. Only few models are based on statistical approach, they are very inspired from the rubber like materials excepted that the micro structure of the soft tissues are not considered by chains [Bischoff *et al.*, 2002; Raghupathy and Barocas, 2009].

1.5.2 Stress softening

It is important to model the Mullins effect, as the mechanical behavior of the material can largely change after a first loading as it depends both on the maximal deformation and the loading direction. Nevertheless, Mullins effect could be ignored for particular studies, for instance Lion [1997a]; Rey *et al.* [2014] analyzed the hysteresis of elastomers during seconds loadings.
Several phenomena are described in the Mullins effect. First the stress softening is often considered as an irreversible effect, several studies show that even at room temperature no recovery was observed [Mullins, 1948; Rigbi, 1980; Hanson *et al.*, 2005]. Then, the

amount of stress softening depends mainly on the rubber like material studied and of the amount of fillers that they contain [Mullins and Tobin, 1957; Kluppel and Schramm, 2000; Dorfmann and Ogden, 2004]. It was experimentally observed that more the rubber like material contain fillers more it presents important stress softening. At the opposite, Meunier *et al.* [2008] shows that an unfilled silicone rubber did not present any stress softening but other authors observed some [Mullins and Tobin, 1957; Harwood and Payne, 1966]. Further details on Mullins effect characterization can be found in the review proposed by Diani *et al.* [2009].
The prediction of the Mullins effect is a large subject and many researchers proposed different models for many years. [Bueche, 1960] developed a micro mechanical based model considering consequent debonding of chains from fillers during the primary loading. He supposed that chains with different lengths are distributed within the rubber network and employed statistical mechanics in order to describe the Mullins effect. In the same way Dannenberg [1974]; Rigbi [1980] developed also models on micro mechanical assumptions of bonded chains. Govindjee and Simo [1991, 1992] proposed model where the network is decomposed into an elastic rubber part and a polymer-filler part. Several models of damage have also been proposed for rubber like material as Gurtin and Francis [1981]; DeSouza Neto *et al.* [1994]; Simo [1987]; Miehe [1995]; Ogden and Roxburgh [1999]. Nevertheless only a few constitutive equations are implemented into industrial finite element codes [Miehe, 1995; Miehe and Keck, 2000; Kaliske *et al.*, 2001; Zuñiga and Beatty, 2002a; Chagnon *et al.*, 2006; Guo *et al.*, 2006; Cantournet *et al.*, 2009; Gracia *et al.*, 2009]. The induced anisotropy by the Mullins effect has also been taken into account in several articles most of time by using damage functions or evolution functions that permit to take into account the history of the material. The only formulation implemented in a finite element code was proposed by Göktepe and Miehe [2005] who used the approach of Miehe *et al.* [2004] introducing a directional damage depending on the energy in the considered direction. According to this new problematic, recent research based on the use of a micro spherical approach have been proposed [Machado *et al.*, 2012b; Lion *et al.*, 2013; Diani *et al.*, 2006a; Merckel *et al.*, 2013].
Soft tissues present also a stress-softening. It was observed for example, for arteries [Vande Geest *et al.*, 2006; Maher *et al.*, 2012], venas [Alastrué *et al.*, 2008], vaginal tissues [Peña *et al.*, 2010], oesophageal [Natali *et al.*, 2009] and [Bose and Dorfmann, 2009; Kroon and Holzapfel, 2008]. Most of these constitutive equations are limited to materials presenting two reinforced directions. The damage functions are only applied on the fibers.

1.5.3 Permanent set

Experimental observations show that many materials present a permanent set in addition of the stress softening. This phenomenon is characterized by a residual strain that depends on the maximal strain reached and of the composition of the material, i.e. the amount of fillers [Menzel and Steinmann, 2001; Ogden, 2004; Diani *et al.*, 2006a]. The following section presents a quick review of the authors that take into account this phenomenon. Dorfmann and Ogden [2004] proposed a model by means of the pseudo-elasticity, which is an isotropic model able to take into account the stress softening and the permanent set. This model is one of the most employed and was implemented into a Finite Element code.

But few models are able to take into account stress softening, permanent set and induced anisotropy of a material. recently Dargazany and Itskov [2009]; Itskov *et al.* [2010] also proposed a model to take into account anisotropic softening and permanent set by means of a pseudo strain energy. Moreover, Diani *et al.* [2006a]; Merckel *et al.* [2013] developed a tridimensional model describing the permanent set and the stress softening and considered them as independent phenomena. Rececently, Ayoub *et al.* [2014] proposed a model that can also take into account the viscous effect of materials by using an alteration theory on rubber like materials.
Inspired by the rubber like materials, several authors proposed pseudo elastic models adapted to soft tissues [Franceschini *et al.*, 2006; Horgan and Saccomandi, 2005]. Micro structurally based models were proposed for 3D generalization for instance by Alastrué *et al.* [2009]. Several authors proposed also phenomenological models to take into account the stress softening and the permanent set [Maher *et al.*, 2012; Peña *et al.*, 2011; Passera *et al.*, 2013]. It is to note that for the soft tissues, it is generally considered that the stress softening and the permanent only occurs in the fibers and not in the matrix.

1.5.4 Viscoelasticity

For the most of rubber like materials, the mechanical behavior depends mainly on the strain rate, and the response varies from purely rubber like material to glassy polymer (Yi *et al.* [2006]; Sarva *et al.* [2007]).
The viscoelasticity in large deformations is classically described according to two different theories. The first theory is the one developed by Green and Rivlin [1957] and Coleman and Noll [1961] by using the principle of Boltzmann superposition. Indeed, Green and Rivlin [1957] introduced and supposed that relaxation functions depend only on the time and Coleman and Noll [1961] considered that these functions depend on time and on the actual state of deformation. These models are expressed in term of convolution integrals and were readapted by Berstein *et al.* [1963] and Zapas and Craft [1965] to finally be known as K-BKZ model for fluids. Later, Ogden [1972] and Christensen [1980] developed the extensions of Green and Rivlin [1957] at the first order for the solids.

$$\boldsymbol{\sigma} = g_0\mathbf{B}(t) + \mathbf{F}(t)\int_0^t g_1(t-\tau)\dot{\mathbf{E}}(\tau)d\tau\mathbf{F}^T(t) - p\mathbf{I} \tag{1.17}$$

Where $\mathbf{E} = (\mathbf{C}-\mathbf{I})/2$ is the Green Lagrange deformation tensor, and g_0 and $g_1$are material parameters. All these models are not numerically implemented except for fluid mechanics, i.e. the K-BKZ model.
The second theory was developed by Green and Tobolsky [1946] by means of differential models with internal variables. The viscoelasticity is classically build up for uniaxial formulations with springs and dashpots and generalized to tensorial formulation. The two standard models used are those of Zenner and Kelvin-Voigt as represented in Fig.1.9. The readaptation of the differential models, initially proposed by Green and Tobolsky [1946], was stimulated 40 years later by the work of Lubliner [1985]. This model is based on the decomposition of the deformation gradient into an elastic part $\mathbf{F_e}$ and an inelastic one $\mathbf{F_p}$.

$$\mathbf{F} = \mathbf{F_e}\mathbf{F_p} \tag{1.18}$$

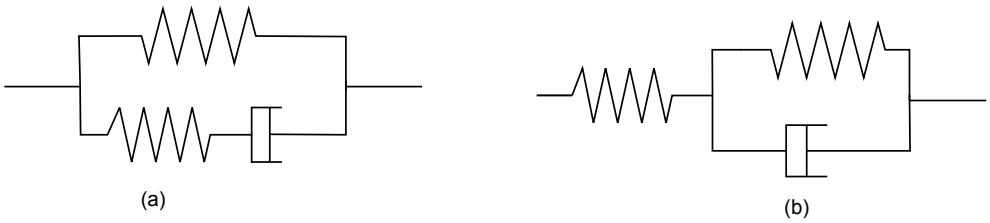

Figure 1.9: Rheological representation of the Maxwell model with a spring in parallel (a) and a Kelvin-Voight model with a spring in serie (b)

Later, several authors [Simo, 1987; Govindjee and Simo, 1992; Holzapfel and Simo, 1996; Lion, 1996; Kaliske and Rothert, 1998] proposed to separate the response of the material as the sum of an elastic and an inelastic stress, thus the internal variable is of "stress" type. Simo [1987] model is equivalent to the K-BKZ model as proved by Reese and Wriggers [1997], and was implemented in a finite element code. It is to note that the IVM theory is mainly used due to the facilities of numerical implementation Green and Tobolsky [1946]; Sidoroff [1974]; Lubliner [1985]. Many authors proposed models of this type as Huber and Tsakmakis [2000]; Reese and Govindjee [1998]; Lion [1997b]; Amin *et al.* [2006] for instance. For all the proposed models, the mechanical behavior is determined by an evolution equation that is consistent with the second law of thermodynamics. Yet non linear evolution equations are now often used to represent at the best the mechanical behavior of the material (Reese and Govindjee [1998]; Holzapfel and Simo [1996]; Miehe and Keck [2000]; Haupt and Sedlan [2001]; Lion [1996]), in these publications different internal variables can be used, anyway this choice depend on each author and is validated as long that the second law is too. Later Amin *et al.* [2006] proposed an improvement of Huber and Tsakmakis [2000] by using a non linear evolution equation for the inelastic strain rate. All these models are phenomenological. Non linear evolution equations were also proposed for micro mechanical models. The most recognized model is the one proposed by Bergstrom and Boyce [1998] which is an extension of the 8 Chain models of Arruda and Boyce [1993]. More recently Miehe and Göktepe [2005] proposed also an micro mechanical model based on the theory of chains constraints in tube. Furthermore this model is based on a micro sphere approach, that means that this model is spread out along a spatial repartition. In the same way Diani *et al.* [2006b] proposed also a model by using a sphere unit repartition and based on micro mechanic statistics Langevin function.
Soft tissues present also a strain rate dependency. Models were developed to take into account the viscoelasticity of soft tissues and the initial anisotropy due to their structure, see for example (Fung [1993]; Miller and Chinzei [1997]; Pioletti and Rakotomanana [2000]; Miller [2000]; Limbert *et al.* [2004]; Taylor *et al.* [2009]; Peña *et al.* [2008]).

1.6 Controlled anisotropy: Architectured materials

An emerging topic for a few years are architectured materials, they take an increasingly important place in many applications due to their specificities including mechanical properties [Bouaziz *et al.*, 2008]. It exists several types of architectured materials. For instance,

some materials are architectured due to their microstructure (grain size for metallic materials, polymer chain design or state of crystallization for example). This strategy operates at scales between 1 nm and 10 μm. The Fig.1.10 illustrates different architectured materials at different sizes, this figure is issue from Jang *et al.* [2013]. Architectured materials

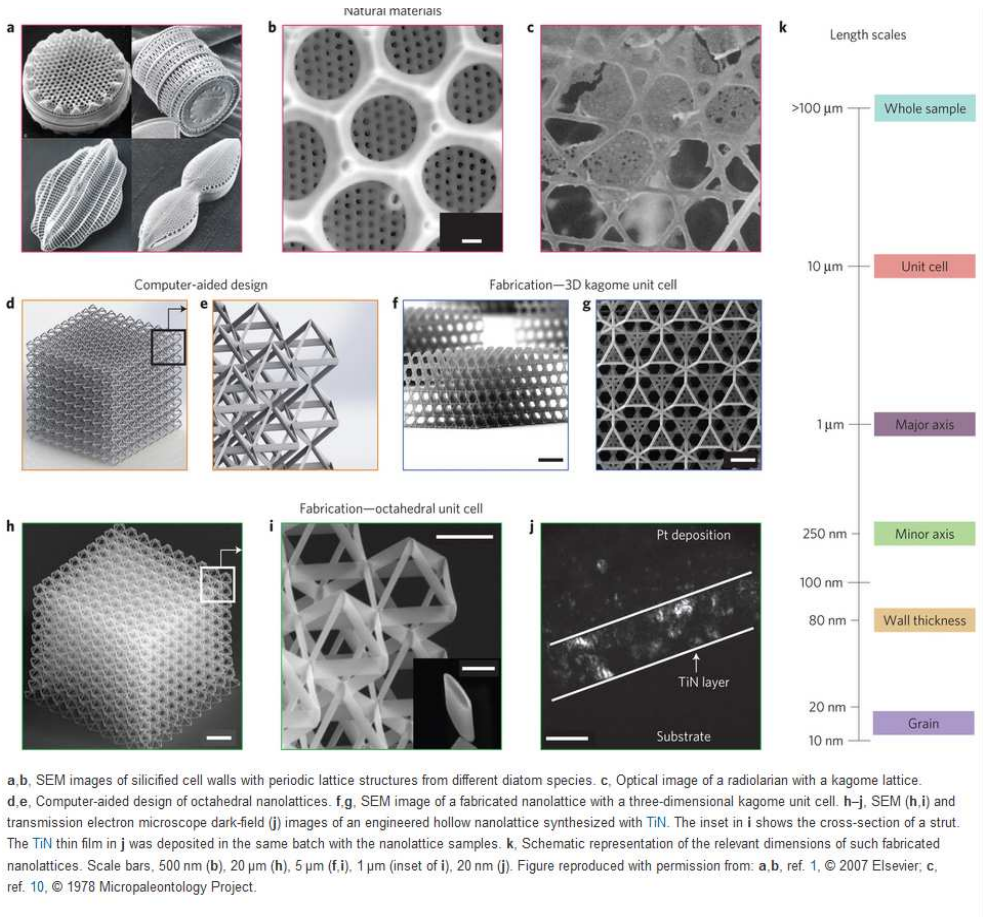

a,**b**, SEM images of silicified cell walls with periodic lattice structures from different diatom species. **c**, Optical image of a radiolarian with a kagome lattice. **d**,**e**, Computer-aided design of octahedral nanolattices. **f**,**g**, SEM image of a fabricated nanolattice with a three-dimensional kagome unit cell. **h**–**j**, SEM (**h**,**i**) and transmission electron microscope dark-field (**j**) images of an engineered hollow nanolattice synthesized with TiN. The inset in **i** shows the cross-section of a strut. The TiN thin film in **j** was deposited in the same batch with the nanolattice samples. **k**, Schematic representation of the relevant dimensions of such fabricated nanolattices. Scale bars, 500 nm (**b**), 20 µm (**h**), 5 µm (**f**,**i**), 1 µm (inset of **i**), 20 nm (**j**). Figure reproduced with permission from: **a**,**b**, ref. 1, © 2007 Elsevier; **c**, ref. 10, © 1978 Micropaleontology Project.

Figure 1.10: Different architectured materials [Jang *et al.*, 2013]

can also be composed with an association of several materials, and are called hybrid material. These architectured materials are usually used to build multifunctional materials [Brechet and Embury, 2013; Ashby, 2013; Bouaziz, 2013]. The Fig.1.11 represents for instance a composite material which is also considered as hybrid: a blade. The association of several materials is often used in industrial applications to improve mechanical properties. However, natural materials are also very often considered as architectured material, as presented by Dunlop and Fratzl [2013]. It can be considered that wood, bones, lobster shell and deep see sponge as illustrated in Fig.1.12 are architectured. Still for the natural architectured material, the human body is composed of many architectured materials, the fibrils collagen present in the bones for instance as represented by Lakes [1993] and in Fig.1.13.

Other materials can be considered as architectured because of their geometry. Meunier [2011] developed crenellated membranes with an unfilled silicone rubber. The main advantage of these membranes is that they present an anisotropic behavior without any

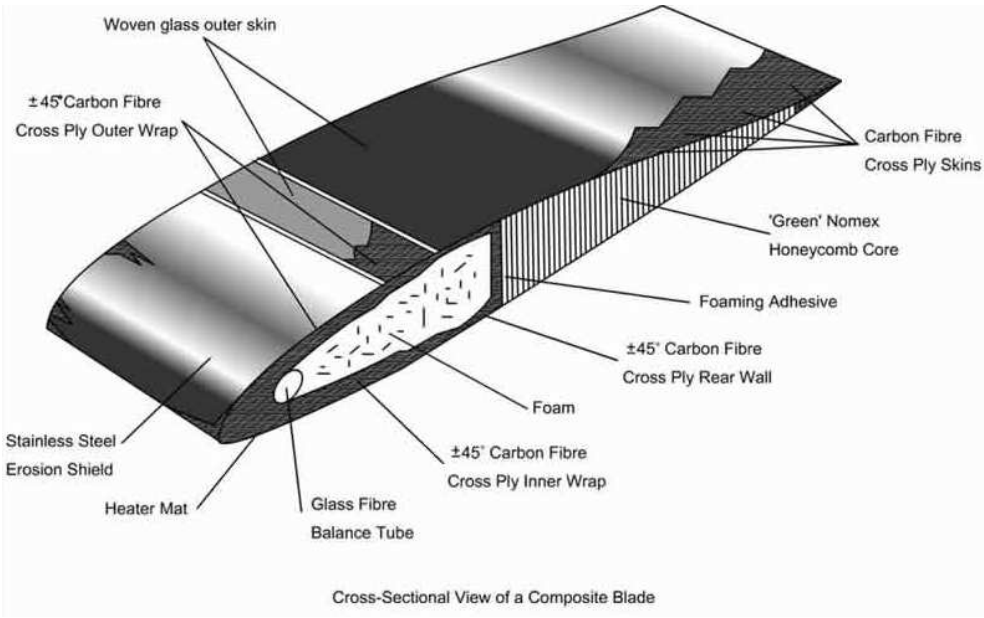

Figure 1.11: Hybrid materials: blade for instance (University of Liverpool)

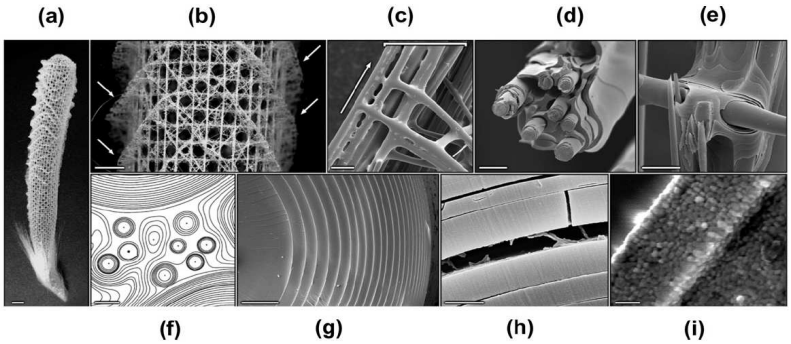

Figure 3. Multiple architectures found in the deep-sea sponge *Euplectella* sp. Skeleton. (a) Macroscopic architecture of the entire sponge skeleton (bar = 1 cm). (b) Reinforced square lattice making up the walls of the skeleton, showing diagonal bracing in every alternate square; arrows indicate orthogonal ridges (bar = 5 mm). (c) Detail of a single strut made up of a bundle of silica spicules; the arrow indicates the longitudinal direction of the strut (bar = 100 μm). (d) Acid-etched and fractured beam showing the ceramic fibre-composite structure (bar = 20 μm). (e) Image of an acid-etched joint, showing the fibre embedded in laminated silica layers (bar = 25 μm). (f) Contrast-enhanced image of a strut showing the multiple spicules embedded in a lamellar silica matrix (bar = 10 μm). (g) Details of the lamellar structure of a single spicule (bar = 5 μm). (h) Details of a fractured spicule showing evidence of a thin organic layer between the silica lamellae (bar = 1 μm). (i) A bleached surface of a cross-section showing the nanoparticles that make up each silica layer (bar = 500 nm). From Ref. [21], with permission from AAAS.

Figure 1.12: Natural architectured materials [Dunlop and Fratzl, 2013]

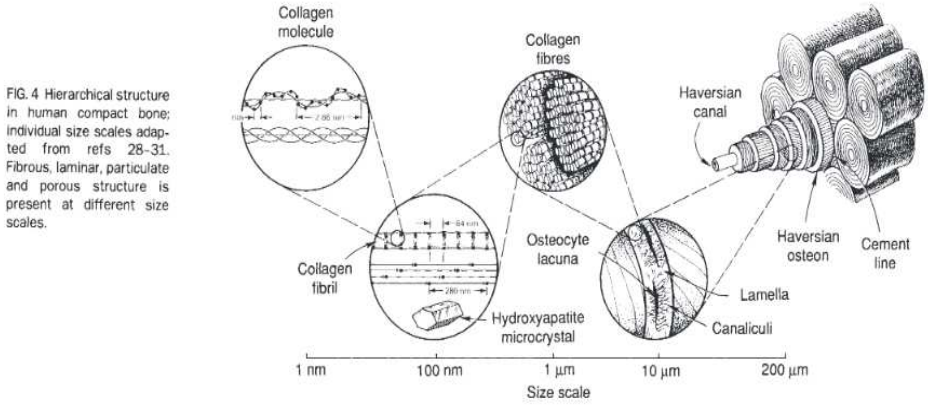

Figure 1.13: Collagen fibrils in bones Lakes [1993]

interface in the material. Indeed, the crenels and their orientations allow to induce and control the anisotropy. By means of these materials and the use of biocompatible materials (as silicone), it is now possible to create biomimetic materials.

1.7 Conclusions

This chapter highlights most of the non linear phenomena observed for the rubber like materials and the soft tissues. Several approach have also been presented to the modeling of them. A major point of this thesis is to develop new constitutive equations to take into account all the non linear phenomena observed. In this way, several experimental tests are performed on different materials. Each one of the material used permit to isolated at least one of the phenomenon to finally build a model able to take into account all the non linear phenomena observed in the same time.

In this way all the following chapter focuses on the study of one phenomenon:

- The first material used is a Room Temperature Vulcanizing (RTV) 3428 silicone. This type of silicone are made from a two component system (base plus curative) and are issue from industrial fabrication and contain fillers. This material is used to investigate the Mullins effect at slow strain rate for an initially isotropic material and does not present residual strain.

- The second material is used to investigate the residual strain of a rubber like material: a Hot Temperature Vulcanization (HTV). This material is still isotropic but present a very important stress softening. This behavior become thus closer from those of soft tissues.

- The viscoelasticity of materials is studied on Nitrile Butadien Rubber (NBR) in an isotropic framework.

- Finally, all the phenomena, including initial anisotropy are taken into account, experimental data are obtained by means of architectured materials, either made of RTV3428 or with a Thermoplastic Elastomer (TPE).

Many analogies between rubber like materials and soft tissues are done in this thesis work. Experimental data issues from literature on Ovine Vena Cava are exploited. By means of the experimental data obtained by means of the different materials, models able to take into account, Mullins effect, permanent set, initial anisotropy, induced anisotropy and viscous effect are developed.

Chapter

2 Anisotropic Mullins effect

Some part of this chapter have been published and can be found in the following reference

- ***M. Rebouah, G. Machado, G. Chagnon, D. Favier**, 2013, Anisotropic Mullins stress softening of a deformed silicone holey plate, Mech. Res. Commun., 49, 36 - 43*

Contents

2.1 General introduction

This chapter focuses on the modeling of the anisotropic Mullins effect. As explained in Chapter 1 the Mullins effect is one of the prevailing non linear phenomena observed for rubber like materials. To study this phenomenon, an isotropic filled silicone is used to isolate the stress softening and the induced anisotropy phenomena without permanent set. Several experimental tests were performed and a constitutive equation by means of a spherical approach is proposed to take into account the Mullins effect. Recently, Machado *et al.* [2010, 2012b] developed a large database for a filled silicone rubber including on one hand cyclic classical experimental tests and on the other hand uniaxial tests performed after different uniaxial and biaxial tension tests. This database is, used here to build a new constitutive equation easily implementable in finite element codes. In Section

2, the constitutive equation is detailed and the ability of the model to describe recent experimental data is discussed. In Section 3, the numerical implementation of the model is treated. In Section 4, the ability of the model to describe complex structures is tackled by means of a specific test on a rectangular plate containing five holes. The global and local estimations of the model are compared to experimental measures. Finally, Section 5 contains some concluding remarks of the modeling.

2.2 Anisotropic modeling of the Mullins effect

2.2.1 General formulation in strain invariants

Different anisotropic approaches to model Mullins effect were proposed in literature, but none of them was only expressed in term of strain invariants. Shariff [2006] and Itskov *et al.* [2010] took into account three principal damage directions to reproduce a special behavior in the direction orthogonal to loading. In a more general way, the spatial repartition of Bazant and Oh [1986] was used by many authors to create an anisotropic model. Diani *et al.* [2006b] and Dargazany and Itskov [2009] generalized the network evolution proposed by Marckmann *et al.* [2002] to an anisotropic approach by taking into account the maximum elongation in each spatial direction. Later Merckel *et al.* [2011, 2012] introduced a new framework and proposed a softening anisotropic criterion adapted to complex loading states.

The stress softening phenomenon has often been associated to the presence of fillers in the rubber, but Harwood *et al.* [1965] showed that stress softening can also occur in unfilled rubbers, even if it is reduced compared to filled rubbers. For silicone rubbers, Meunier *et al.* [2008] observed no Mullins effect for an unfilled one, whereas Machado *et al.* [2010] observed stress softening for a filled one. As a consequence, it can be considered that fillers in silicone rubbers are mainly responsible of the Mullins effect. Thus, as proposed by Govindjee and Simo [1992] the strain energy density $\mathcal{W}$ is additively decomposed into two parts: one that represents the energy density of the chains linked to other chains $\mathcal{W}_{cc}$ and an other part that represents the energy density of the chains linked to filler $\mathcal{W}_{cf}$. The total strain energy density is $\mathcal{W} = \mathcal{W}_{cc} + \mathcal{W}_{cf}$. It is considered that only $\mathcal{W}_{cf}$ can evolve with the Mullins effect as in Göktepe and Miehe [2005]. As a consequence $\mathcal{W}_{cc}$ is represented by a classical hyperelastic isotropic energy density and $\mathcal{W}_{cf}$ must be represented by an anisotropic strain energy that can evolve with the deformation history of the material. The ideal representation would be to propose a full integration of all spatial directions as proposed by Wu and Giessen [1993] in hyperleasticity, but it is not adapted to finite element implementation. A spatial discretization is needed. Forty-two initial spatial directions, noted $\mathbf{A}^{(i)}$, are introduced, these directions are those proposed by Bazant and Oh [1986]. Therefore, the strain energy density is written as:

$$\mathcal{W} = \mathcal{W}_{cc}(I_1, I_2) + \sum_{i=1}^{n} \omega^{(i)} \mathcal{F}^{(i)} \mathcal{W}_{cf}^{(i)}(I_4^{(i)}) \tag{2.1}$$

where I_1, I_2 are the first and second strain invariants of the right Cauchy-Green strain tensor $\mathbf{C}$. The strain in each direction (i) is defined by means of $I_4^{(i)} = \mathbf{A}^{(i)}.\mathbf{C}\mathbf{A}^{(i)}$. $\omega^{(i)}$ represents the weight of each direction and $\mathcal{F}^{(i)}$ is the Mullins effect evolution function. The

initial directions $\mathbf{A}^{(i)}$ are transformed in $\mathbf{a}^{(i)}$ by $\mathbf{a}^{(i)} = \mathbf{F}\mathbf{A}^{(i)}$, where $\mathbf{F}$ is the deformation gradient.

Classically, in an isotropic approach, the evolution function $\mathcal{F}^{(i)}$ would be written through the strain energy density, but Chagnon *et al.* [2004] showed that the first invariant can also be used. In an anisotropic approach, the elongation in each direction is used Diani *et al.* [2006b], knowing that the elongation is the square root of the invariant I_4. According to the conclusions of Machado *et al.* [2012b], it is chosen to describe the stress-softening function according to I_1 and ${I_4}^{(i)}$. For each direction (i), an evolution function which depends on three terms $\mathcal{F}_1$, $\mathcal{F}_2$, $\mathcal{F}_3$ is proposed:

$$\mathcal{F} = 1 - \mathcal{F}_1({I_1}^{\max} - I_1)\mathcal{F}_2\left({I_4}^{\max(i)} - {I_4}^{(i)}\right)\mathcal{F}_3\left(\frac{{I_4}^{\max(i)}}{{I_4}^{\max}}\right) \tag{2.2}$$

Where ${I_1}^{\max}$ and ${I_4}^{\max(i)}$ represent the maximum values taken during the material history by I_1 and ${I_4}^{(i)}$ respectively. ${I_4}^{\max} = \max_i({I_4}^{(i)})$ is the maximum dilatation in space and time. As proposed by Zuñiga and Beatty [2002b], a function that is constant during first loading and that evolves with the maximum and current deformations is imposed for the evolution function.

2.2.2 A particular form for evolution function

A Mooney [1940] constitutive equation is chosen for $\mathcal{W}_{cc}$, and a Kaliske [2000] quadratic equation $K(I_4^{(i)} - 1)^2$ is chosen for $\mathcal{W}_{cf}^{(i)}$, where $K^{(i)}$ is a material parameter. A first particular form is proposed for the stress-softening function, considering that a minimum of parameters should be introduced:

$$\mathcal{F}^{(i)} = 1 - \eta\sqrt{\frac{I_{1\max} - I_1}{I_{1\max} - 3}}\left(\frac{I_{4\max}^{(i)} - I_4^{(i)}}{I_{4\max}^{(i)} - 1}\right)\left(\frac{I_{4\max}^{(i)}}{I_{4\max}}\right)^4 \tag{2.3}$$

In this way, the evolution function depends only on one parameter: η which controls the stress softening for a given direction, this parameter is without unity. The large experimental database proposed by Machado *et al.* [2010, 2012b] on a filled silicone rubber is used to fit the model. These experimental results are decomposed into three parts: first the classical uniaxial tension, planar tension and biaxial tests realized by means of a bulge test [Machado *et al.*, 2012a], second the complex tensile tests with change of directions after the first loading; and third biaxial tensile tests followed by uniaxial tensile tests. The three hyperelastic parameters C_1, C_2 and $K^{(i)}$ are obtained by fitting the different first loading curves. All the $K^{(i)}$ parameters are chosen equal as the material is initially isotropic. The followings values are obtained: $C_1 = 0.05$MPa, $C_2 = 0.03$MPa and $\forall i \quad K^{(i)} = 0.10$MPa. The last parameter that characterizes the stress softening is obtained by minimizing the errors on the second loading curves for all the tests. The value $\eta = 4$ is obtain

The simulations of the cyclic uniaxial tensile, pure shear and equibiaxial tensile tests are presented in Fig. 2.1. It appears that the model describes well the stress softening for all these tests. The model predicts well uniaxial and pure shear tests whereas equibiaxial first loading curve is underestimated. This phenomenon is expected since first loading depends only on the hyperelastic equation. As explained by Marckmann and Verron [2006], it is difficult to fit all the different tests with the same energy density.

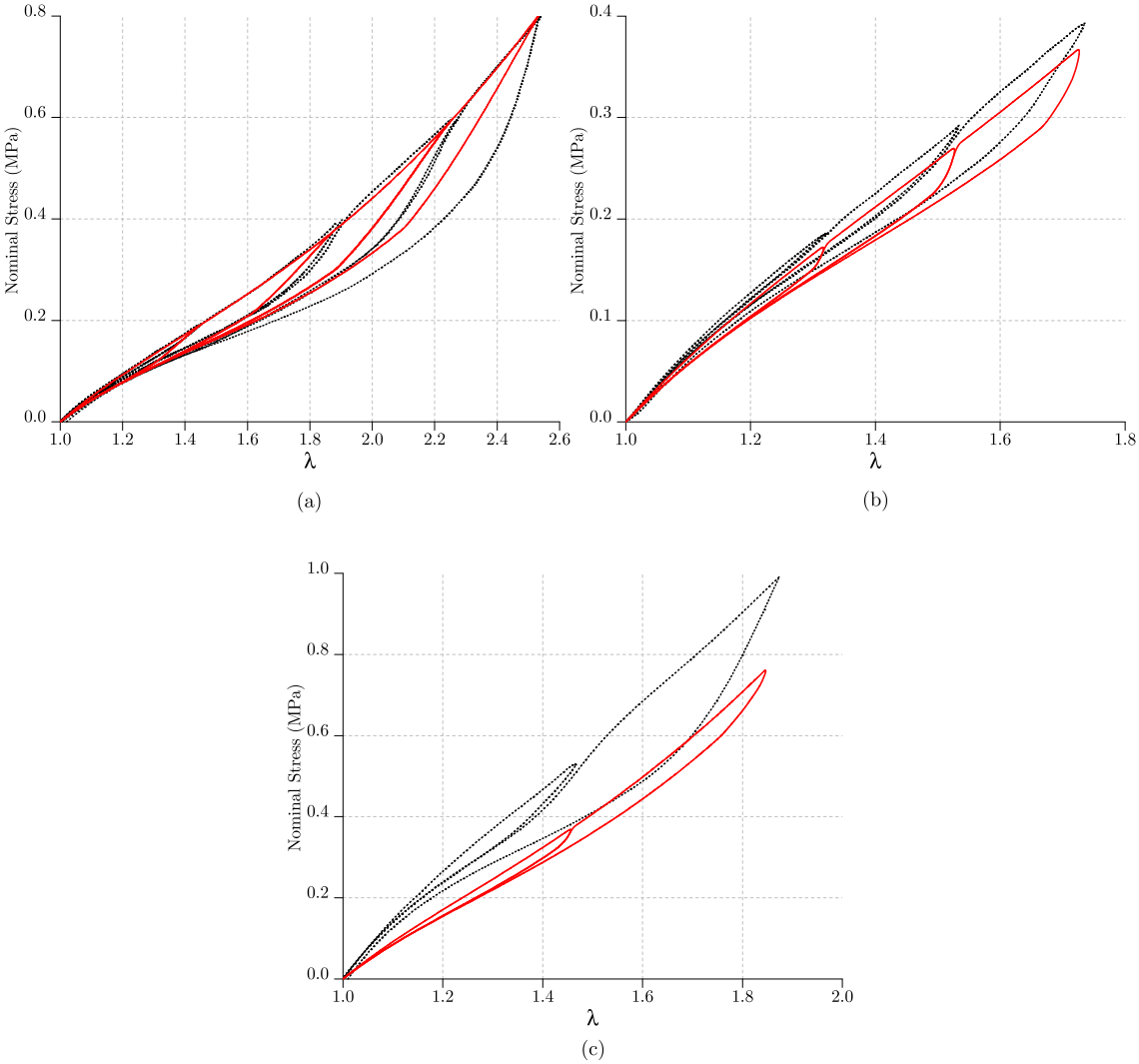

Figure 2.1: Comparison of the model (solid lines) with experimental data (dotted lines) from Machado *et al.* [2010] (a) cyclic uniaxial tensile test, (b) cyclic pure shear test (c) cyclic equibiaxial test.

The proposed model is now compared with the experimental data of the two complex pre-conditioning methods. First, Fig. 2.2, presents the results for tensile tests with a change of loading direction between the first and second loadings. The results from the model do not superimpose exactly experimental data, but all trends are quite well described for the different directions. Second, the model predictions are compared with biaxial pre-stretching tests results. The biaxial loading is characterized by the biaxiality ratio defined as $\mu = \ln(\lambda_{\min})/\ln(\lambda_{\max})$ (where $\lambda_{\min}$ and $\lambda_{\max}$ are the minimum and maximum in-plane principal elongation). Tests with different biaxiality ratios were used for the simulation. The comparison of the second loading curves is presented in Fig. 2.3. It appears that the stress softening is slightly overestimated but the return point on the first loading curve is very well described.

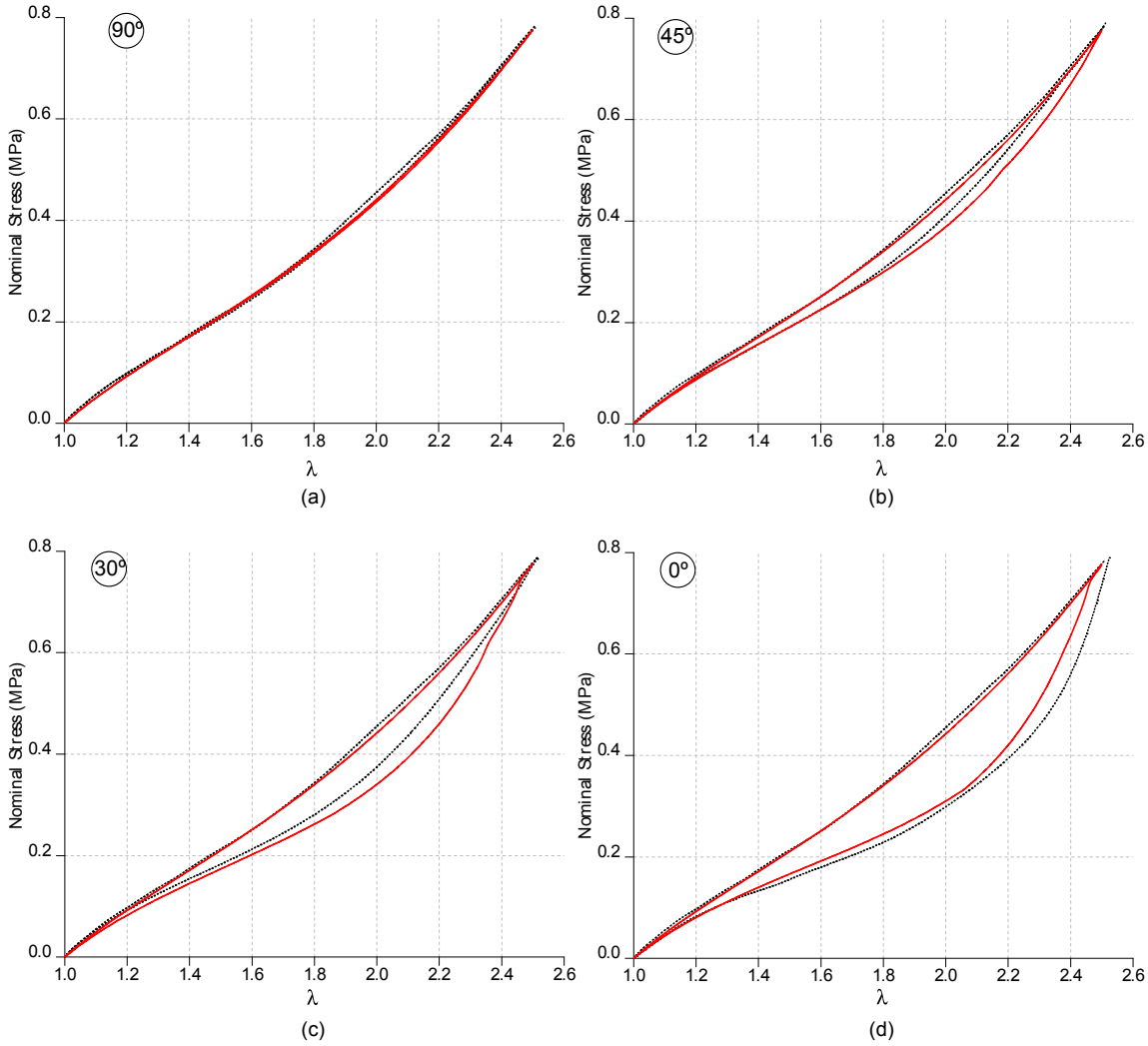

Figure 2.2: Comparison of the model (red line) with uniaxial pre-stretching experimental data (dotted lines) from Machado *et al.* [2012b]. Second tensile test oriented (a) at 90° (b) at 45° (c) at 30° and (d) at 0°

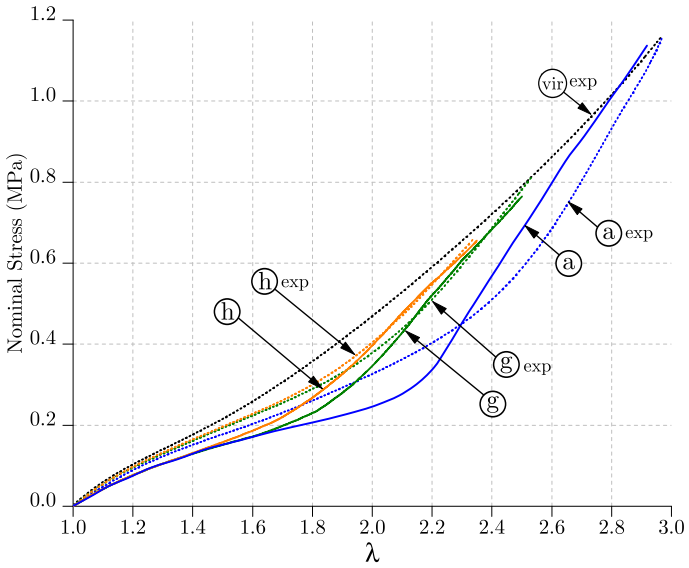

Figure 2.3: Comparison of the model (solid lines) with biaxial pre-stretching experimental data (dotted lines). Curve a presents simulation of the model for the second load after an equibiaxial test; curve g presents simulation of the model for the second load after a biaxial test of biaxiality rate $\mu = 0.7$; curve h presents simulation of the model for the second load after a biaxial test of biaxiality rate $\mu = 0.5$

2.3 Finite element implementation

Considering the model proposed in the last section, the strain energy density depends on the first, second and forty-two fourth invariants, i.e., $\mathcal{W} = \mathcal{W}(I_1, I_2, I_4^{(i)})$. As the numerical implementation needs a quasi-incompressible formulation [Federico *et al.*, 2008; Holzapfel *et al.*, 2000; Holzapfel and Gasser, 2001; Ogden, 2003, 1997; Sun W, 2005], the equation must be rewritten in terms of incompressible invariants as follows:

$$\mathcal{W} = \bar{\mathcal{W}}(\bar{I}_1, \bar{I}_2, \bar{I}_4{}^{(i)}) + \mathcal{U}(J) \tag{2.4}$$

where $J^2 = I_3 = \det(\mathbf{C})$ is the volume variation, and $\bar{I}_1 = I_3^{-1/3} I_1$, $\bar{I}_2 = I_3^{-2/3} I_2$, $\bar{I}_4{}^{(i)} = I_3^{-1/3} I_4^{(i)}$ are the incompressible invariants. The problem of the implementation of anisotropic hyperelastic energy densities has ever been tackled in literature, see for example [Peña *et al.*, 2009; Bose and Dorfmann, 2009; Kroon and Holzapfel, 2008]. After the decomposition given in Eq. 2.4, the second Piola-Kirchhoff stress tensor $\mathbf{S}$ is obtained by the strain energy derivation, as

$$\mathbf{S} = \bar{\mathbf{S}} + \mathbf{S}^{vol} = 2 \left\{ \frac{\partial \bar{\mathcal{W}}}{\partial \bar{I}_1} \frac{\partial \bar{I}_1}{\partial \mathbf{C}} + \frac{\partial \bar{\mathcal{W}}}{\partial \bar{I}_2} \frac{\partial \bar{I}_2}{\partial \mathbf{C}} + \sum_{i=1}^{n} \frac{\partial \bar{\mathcal{W}}}{\partial \bar{I}_4{}^{(i)}} \frac{\partial \bar{I}_4{}^{(i)}}{\partial \mathbf{C}} \right\} + J \frac{\partial \mathcal{U}}{\partial J} \mathbf{C}^{-1} \tag{2.5}$$

Where $\bar{\mathbf{S}}$ and $\mathbf{S}^{vol}$ are respectively the isochoric and volumetric parts of the second Piola-Kirchhoff stress tensor $\mathbf{S}$. The Lagrangian deviatoric tangent modulus, is finally given by

$$\bar{\mathbb{C}}^{\,L} = 4 \left\{ \frac{\partial}{\partial \mathbf{C}} \left(\bar{\mathcal{W}}_{,1} \frac{\partial \bar{I}_1}{\partial \mathbf{C}} \right) + \frac{\partial}{\partial \mathbf{C}} \left(\bar{\mathcal{W}}_{,2} \frac{\partial \bar{I}_2}{\partial \mathbf{C}} \right) + \sum_{i=1}^{n} \frac{\partial}{\partial \mathbf{C}} \left(\bar{\mathcal{W}}_{,4}^{(i)} \frac{\partial \bar{I}_4{}^{(i)}}{\partial \mathbf{C}} \right) \right\} \tag{2.6a}$$

$$\tag{2.6b}$$

Where $\bar{\mathcal{W}}_{,k}$ notes $\frac{\partial \bar{W}}{\partial \bar{I}_k}$. The Eulerian deviatoric modulus is deduced by means of the push–forward operation Φ_* as $\bar{\mathbb{C}}^{\,e} = \frac{1}{J} \Phi_*(\bar{\mathbb{C}}^{\,L})$.

Finally the stress and the tangent modulus are given by the first and second derivates of the strain energy function with respect to the first, second and fourth invariants. The general form of $\bar{\mathbb{C}}^{\,L}$ and $\mathbb{C}^{\,L}_{vol}$ are presented in Kaliske [2000]. For the present model, the particular forms of the derivatives of the energy are expressed as:

$$\bar{\mathcal{W}}_{,4}^{(i)} = 2K\, w^{(i)}\, \mathcal{F}^{(i)}\, (\bar{I}_4^{(i)} - 1) \tag{2.7}$$

$$\bar{\mathcal{W}}_{,44}^{(i)} = 2K\, w^{(i)} \left\{ \frac{\partial \mathcal{F}^{(i)}}{\partial \bar{I}_4^{(i)}} (\bar{I}_4^{(i)} - 1) + \mathcal{F}^{(i)} \right\} \tag{2.8}$$

$$\bar{\mathcal{W}}_{,14}^{(i)} = 2K\, w^{(i)} \frac{\partial \mathcal{F}^{(i)}}{\partial \bar{I}_1} (\bar{I}_4^{(i)} - 1) \tag{2.9}$$

with the following conditions

$$\begin{aligned} &\text{if} \quad \bar{I}_{1\max} = I_1 \quad \frac{\partial \mathcal{F}^{(i)}}{\partial \bar{I}_1} = 0 \\ &\text{elseif} \qquad \frac{\partial \mathcal{F}^{(i)}}{\partial \bar{I}_1} = \eta \tfrac{1}{2} \left(\frac{\bar{I}_{1\max} - \bar{I}_1}{\bar{I}_{1\max} - 3} \right)^{-\frac{1}{2}} \left(\frac{1}{\bar{I}_{1\max} - 3} \right) \left(\frac{\bar{I}_{4\max}^{(i)} - \bar{I}_4^{(i)}}{\bar{I}_{4\max}^{(i)} - 1} \right) \left(\frac{\bar{I}_{4\max}^{(i)}}{\bar{I}_{4\max}} \right)^4 \end{aligned} \tag{2.10}$$

$$\begin{aligned} &\text{if} \quad \bar{I}_{4\,\max}^{(i)} = \bar{I}_4^{(i)} \quad && \frac{\partial \mathcal{F}^{(i)}}{\partial \bar{I}_4^{(i)}} = 0 \\ &\text{elseif} && \frac{\partial \mathcal{F}^{(i)}}{\partial \bar{I}_4^{(i)}} = \eta \sqrt{\frac{\bar{I}_{1\,\max} - \bar{I}_1}{\bar{I}_{1\,\max} - 3}} \left(\frac{1}{\bar{I}_{4\,\max}^{(i)} - 1} \right) \left(\frac{\bar{I}_{4\,\max}^{(i)}}{\bar{I}_{4\,\max}} \right)^4 \end{aligned} \tag{2.11}$$

Finally, the model is implemented via a UMAT in the Finite Element code Abaqus and simulations can be realized [Abaqus, 2002].

2.4 Validation of the model on a structure calculus

2.4.1 Presentation of an experimental holey plate tension test

To test the ability of the model to simulate adequately a complex structure, an experimental test was designed. A RTV-3428 silicone rectangular plate sample with a thickness of 2mm was molded using the same protocol as in Machado *et al.* [2010]. After molding, five holes were generated. The final dimensions of the holey plate are described in Fig. 2.4(a). The plate was put into a tensile device which allows to record the force undergone by the plate. The force measure is synchronized with a Stereo Digital Image Correlation (SDIC) system. The SDIC technique allows the determination of three dimensional surface displacements and strain fields of the plate [Machado *et al.*, 2012a]. Thus, under the incompressibility assumption, in each point of the plate, the strain tensor is evaluated.
To observe the Mullins effect, a cyclic tensile test is performed on this plate. Its strain field is studied for a macroscopic engineering strains of 50% after different maximal engineering strain: 50 %, 100% and 150%. It is chosen to study in details three paths in the holey plate, they are represented in Fig. 2.4(a). These paths were chosen in order to obtain very different deformation states, i.e., different values of biaxiality ratio μ: that allows to highlight the reliability of the proposed model. As an illustration, Fig. 2.4(b) presents the evolution of the biaxiality ratio at the same level of macroscopic deformation i.e. 50% for the three paths.

2.4.2 Comparison with model predictions

Finite element simulations of the holey plate were performed in plane stress hypothesis with linear elements. The objective of this section is to compare the experimental and numerical results for an engineering strain of 50%. The following notations are used in this part, $1\mathcal{C}_{50}^{EF}$ and $1\mathcal{C}_{50}^{exp}$ represent the first load for the numerical model and experimental results, respectively. In the same way, $2\mathcal{C}_{100}^{EF}$, $2\mathcal{C}_{100}^{exp}$, and $2\mathcal{C}_{150}^{EF}$, $2\mathcal{C}_{150}^{exp}$ represent the deformation at 50% after a first load of 100% and 150%, respectively.

2.4.2.1 Global behavior of the plate

The global displacement and the force undergone by the plate for the experimental and numerical tests are compared in Fig 2.5. It appears that the first and second loadings are very close. A small difference appears for the first loading but, it is due to the

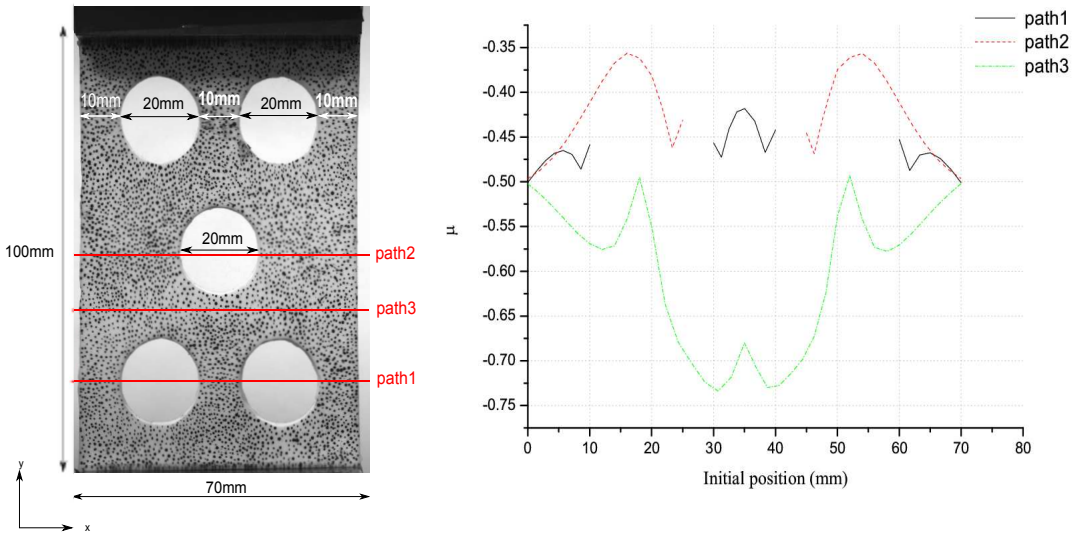

Figure 2.4: (a) Silicone holey plate sample containing five holes and the three paths of interest, (b) Biaxiality ratio along the three paths

underestimation of biaxial loading by the model. This small difference is only due to the hyperelastic constitutive equation and not to the stress softening function.

2.4.2.2 Contours of the plate and strain fields measurements

Fig 2.6 presents the maximal principal logarithmic strain field obtained for the holey plate by finite element simulation and experimental measurement for $2\mathcal{C}_{100}$ configurations. Considering the strain field distribution along the plate surface, it appears that the FE simulation represents quite well the experimental data. The results are the same for $1\mathcal{C}$ and $2\mathcal{C}_{150}$ configurations but these results are not presented in the paper. The contours of the plate are compared for $1\mathcal{C}_{50}$, $2\mathcal{C}_{100}$ and $2\mathcal{C}_{150}$ configurations and presented in Fig 2.7 for a deformation of 50%. The experimental tests are the gray picture and the FE simulations are the contour lines in red. It is possible to observe that experimental results and numerical simulations are almost superposed.

2.4.2.3 Observation of specific paths

To focus on the local behavior of the plate, the maximal principal logarithmic strain along the different paths (defined in Fig. 2.4) is presented in Fig. 2.8. A comparison between the experimental and numerical tests is presented. According to the Fig. 2.8(a) the maximal principal logarithmic strain is greater for the second loadings than for the first loadings along path1, but Fig. 2.8(b) and (c) show that the maximal principal logarithmic strain is more important for the first loadings that for the second loadings along path2 and 3. This difference is explained by the local state of deformation reached along each path.

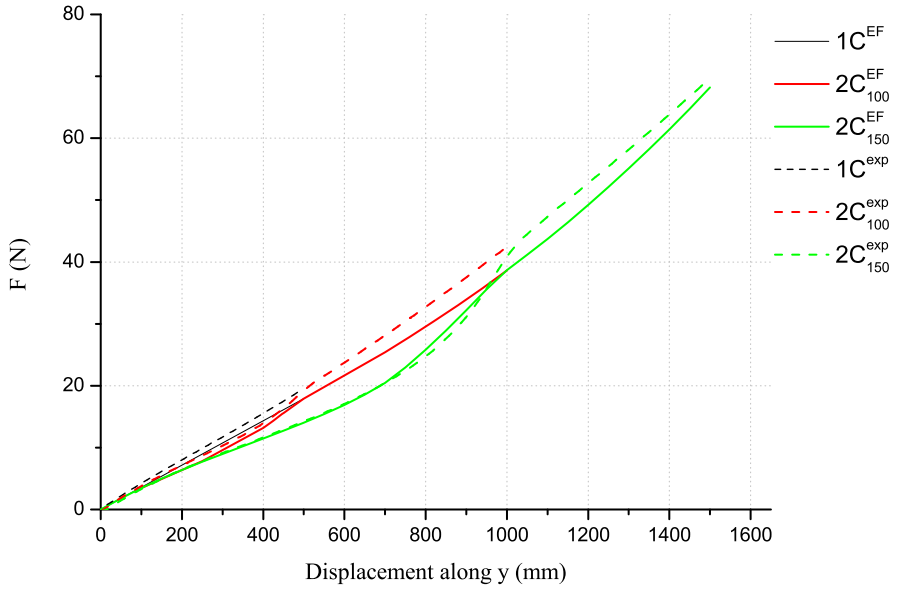

Figure 2.5: Comparison of global force response between the proposed model and the experimental holey plate.

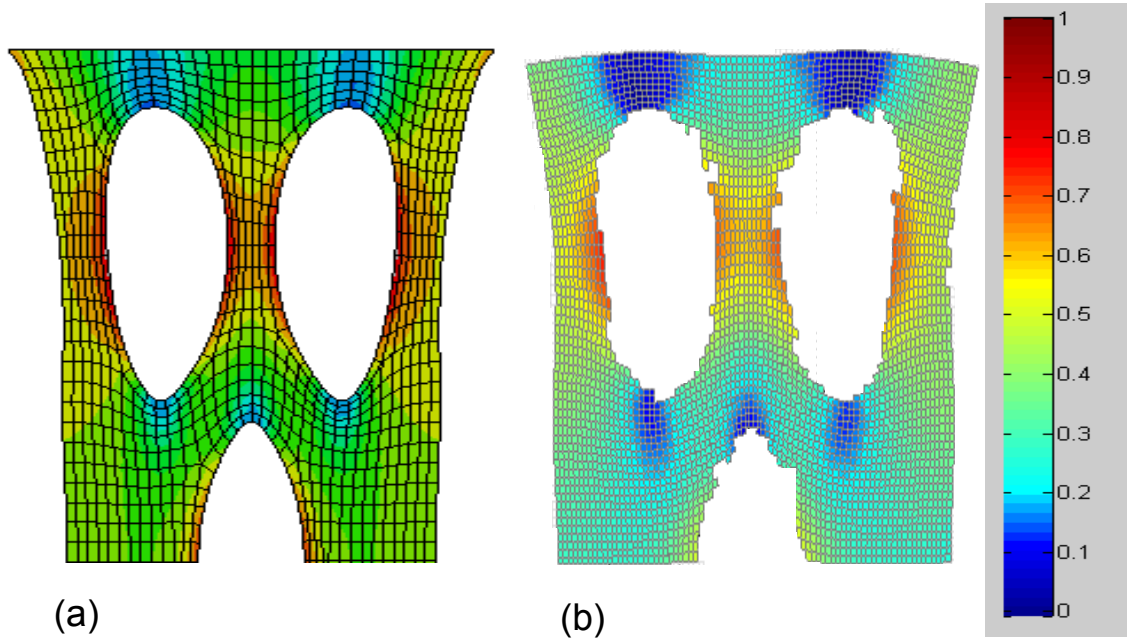

Figure 2.6: Maximal strain logarithmic fields of the silicone plate for the first loading : (a) numerical results and (b) experimental results.

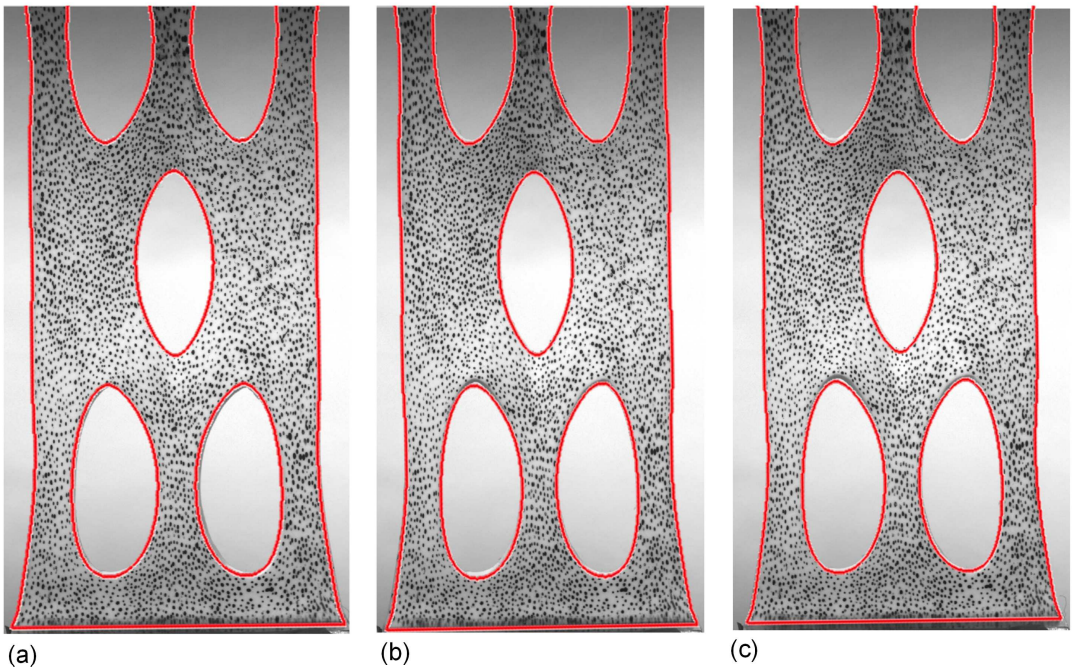

Figure 2.7: Comparison of the contours of the plate for $1\mathcal{C}_{50}$ (a), $2\mathcal{C}_{100}$ (b) and $2\mathcal{C}_{150}$ (c) at 50% of deformation. Gray pictures represent experimental data and red lines numerical data.

The maximal deformation is reached along the path1 so the stress-softening too. Since the stress-softening is maximal along the path1 it generates more important deformation along this path during seconds loadings. Along the paths2 and 3 the stress-softening is smaller that along the path1 so the deformations generated along these paths decrease for the second loadings since the global deformation of the holey is still the same as the first loading.

Fig. 2.8 also shows that the results are quite similar even if there is not a perfect spatial superposition between experimental and FE simulations. This difference can be also explained by the out-of-plane deformation, induced by the geometry of the holey plate, during the experimental test. Indeed for the experimental tests an out-of-plane displacement, close to the holes of the silicone plate, was observed. This out-of-plane displacement does not occur in numerical simulation since it is defined in plane stress. Thus, the superposition of the results is better along the path 2 (Fig. 2.8(b)) than along the paths 1 and 3 (cf. Fig. 2.8(a) and (c)) since the out-of-plane displacement observed is minimal near the hole of the path2 and maximal near the holes of paths1 and 3.

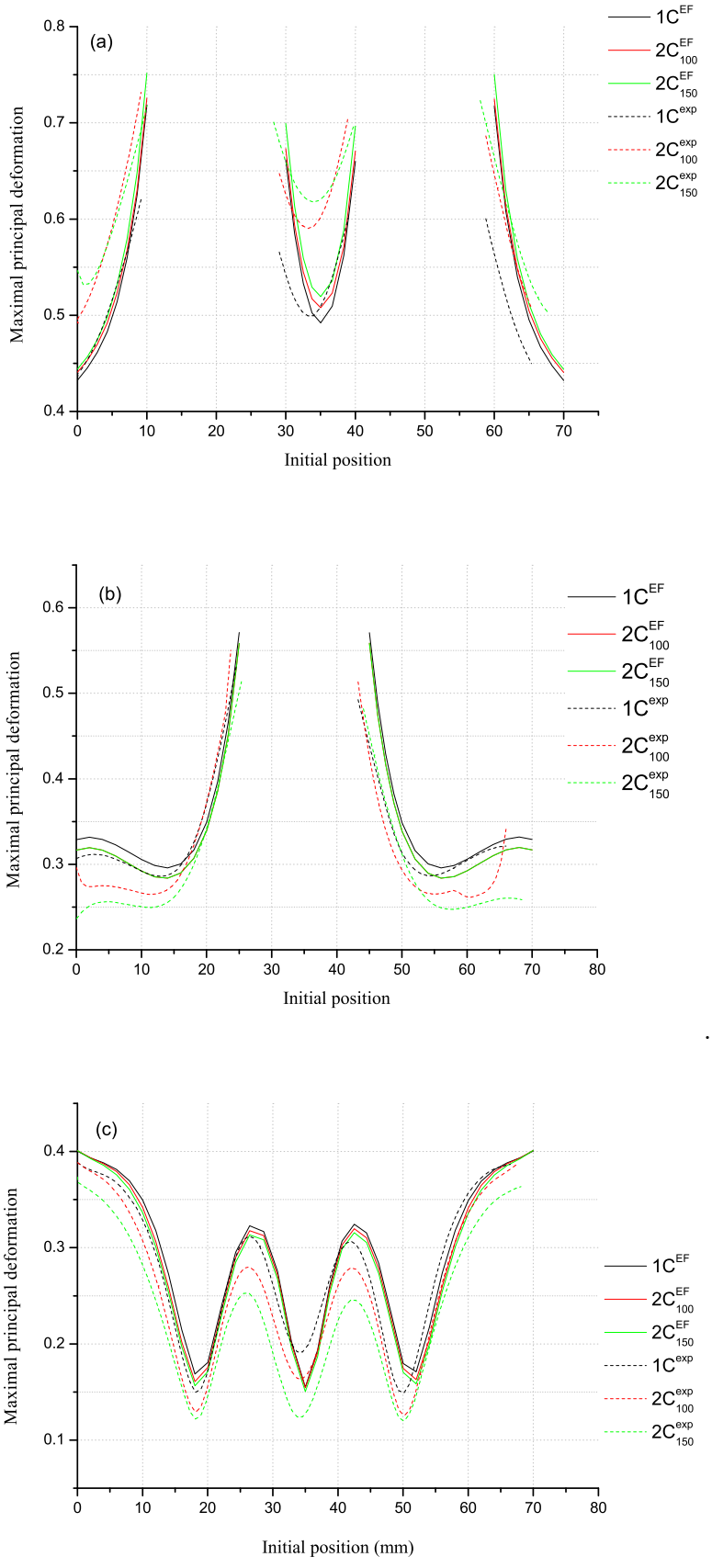

Figure 2.8: Maximal principal deformation for a global strain of 50% along the path1 (a), the path2(b) and the path3 (c).

2.5 General conclusion

The new constitutive equation presented here, permits to describe the stress softening phenomenon for very different loading states (uniaxial to biaxial). The comparison between FE simulation and experimental data highlighted that the return point on the first loading curve is very well described, and that the trends of the second loading curves are also well depicted. The form of the evolution function can be changed to improve the comparison between FE simulation and experimental data. The main difference between this new model and models from literature is that the stress softening function depends both on a global measure (i.e. the first invariant), and directional measure (i.e. the fourth invariants) although only a global measure is used in the isotropic approaches and only a directional measure is used in anisotropic approaches. The recording of this both measures allows the construction of a stress softening function that captures both the directional stress-softening and the return points on the first loading. To have a simple invariant form a quadratic energy density was chosen for the directional energies, but it can also be adapted to non-Gaussian chain theory as often used in literature. The choice of strain measures to describe stress softening was motivated by an easier implementation in finite element codes to obtain an explicit formulation. The general form of the constitutive equation can also be adapted to other stress softening measures. Thus, this chapter permits the development of a constitutive equation able to take into account two of the non linear effects classically observed for rubber like materials: stress softening and induced anisotropy.

Chapter

3 Permanent set

Some part of this chapter have been published and can be found in the following reference

- ***M. Rebouah, G. Chagnon**, 2013b, Permanent set and stress-softening constitutive equation applied to rubber-like materials and soft tissues, Acta Mechanica, 1-14*

Contents

3.1 General introduction

The previous chapter described a new constitutive equation to take into account the stress softening and the induced anisotropy endured by an isotropic material. Nevertheless as presented in Chapter 1, it appears that most of materials that present a stress softening

and an induced anisotropy present also a permanent set. This chapter aims to adapt the previous model to take into account this phenomenon. Furthermore this chapter present also an extension of the model to soft tissues. The model is in a first part developed and validated on HTV rubbers like materials and then the experimental data of Peña and Doblaré [2009] on ovine vena cava are used to validate his efficiency on an initially anisotropic soft tissue.

Thus, in Section 2 an experimental study lead on a filled HTV rubber is presented and highlights that the materials endured several phenomena such as: the stress softening, the induced anisotropy and the permanent set. In Section 3, constitutive equations are developed to take into account these effects for rubber like materials. Section 4 presents a successful comparison of the model with the experimental data. Finally, Section 5 presents the extension of the constitutive equation to soft tissues, the results are compared to experimental data.

3.2 Experimental data on silicone rubber

3.2.1 Materials

Two materials are used for this study, an initially isotropic one, a silicone rubber and an initially anisotropic one, an ovine vena cava [Peña and Doblaré, 2009]. The silicone rubber used is a Heat Cured Silicone (HCS) also called Hot Temperature Vulcanization (HTV) which contains 30% of fillers (silica). This filled silicone rubber is vulcanized with a peroxyde starter. A plate of 185 mm length, 170 mm width and 2.5 mm thick is molded and vulcanized under an increasing pressure (0.1MPa to 0.5 MPa) and a temperature 180°C. No experimental study is lead on the soft tissues. The experimental data are used from Peña and Doblaré [2009].

3.2.2 Classical tensile tests

Tensile tests were realized on samples of 15 mm length, 2.5 mm width and 2.5 mm thick cut from the molded rectangular plate. First, the influence of the strain rate is evaluated. Cyclic tensile tests up to $\lambda = 2.5$ (λ represents the actual length of a sample over its initial length) were performed at different strain rates: 0.025 s^{-1}, 0.167 s^{-1}, 1. s^{-1}, 1.667 s^{-1}. For these small variations of the strain rate, there is no significant influence on the mechanical behavior of rubber like material. For the study it is thus chosen to perform all the following tests at a strain rate of $1.s^{-1}$. Second, silicone specimens were submitted to cyclic loading up to a fixed stretch. Each of the specimens was subjected to two loading unloading cycles up to $\lambda = 2$. After completion of the second unloading cycle, each specimen was then loaded up to a stretch of $\lambda = 2.5$. No recovery time was allowed during the two loading unloading cycles. The results of one test can be observed in Fig.3.1. The stress softening and the permanent set can be observed as an hysteretic behavior, which is not taken into account in this study.

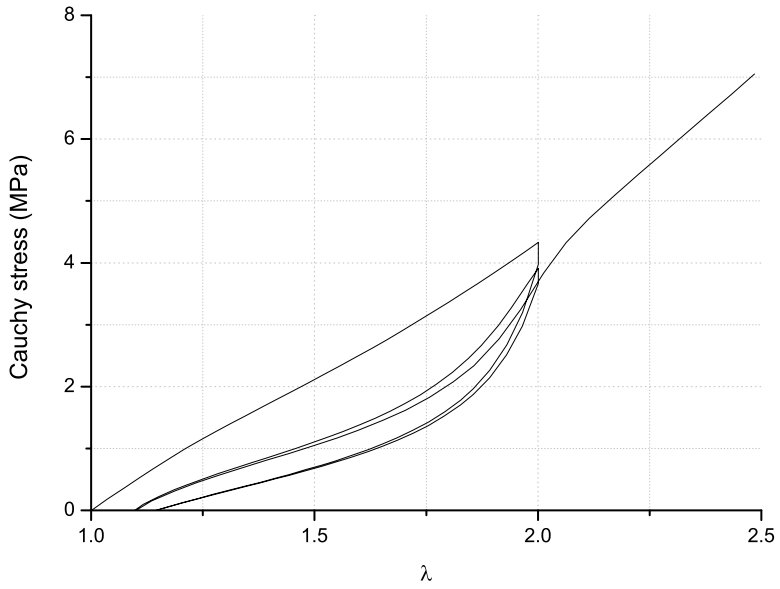

Figure 3.1: Cyclic tensile test on HTV silicone at a strain rate of $1s^{-1}$

3.2.3 Induced anisotropy by the Mullins effect

In this section, it is proposed to highlight the induced anisotropy by the Mullins effect in the HTV silicone rubber. First, a large sample of silicone is prepared for a pure shear test, it is presented in Fig.3.2(a). This sample of 40 mm length, 15 mm width and 2 mm thick is submitted to a cyclic tensile test up to $\lambda = 2$. This test is performed at a strain rate of 1 s^{-1}. Next, several samples are cut from this sample along different orientations ($\alpha = 0°$, $\alpha = 25°$, $\alpha = 45°$, $\alpha = 90°$) compared to the first tensile direction as illustrated in Fig.3.2(b). Four new samples of 15 mm length, 2.5 mm width and 2 mm thick are obtained. Each specimen is subjected to a loading unloading cycle up to $\lambda = 2.5$ at a strain rate of 1 s^{-1}.

The mechanical test realized and described in Fig.3.2 can be studied in different configurations (cf. Fig.3.2(c)). The first configuration C_0 is the initial configuration of the sample (before pure shear test). The C_1 configuration is the intermediary configuration (after pure shear test) and C_2 is the final configuration where the four samples cut according to different orientations from the pure shear test sample are submitted to a tensile test. By means of these tests, several observations can be done. First, the influence of the orientation of the samples is highlighted in Fig.3.3(a). For this representation, it is considered that the initial configuration is C_1 and not C_0 (cf. Fig.3.2(c)). The reference configuration is thus considered after the pure shear test, that means that the stress softening is studied without initial permanent set induced by the pure shear test. This allows to focus on the influence of the orientation. It is observed that for an orientation of $\alpha = 90°$ the material has the same behavior as a first loading (i.e. behavior similar to a virgin material). For an orientation of $\alpha = 0°$ the mechanical behavior is a classical second loading without

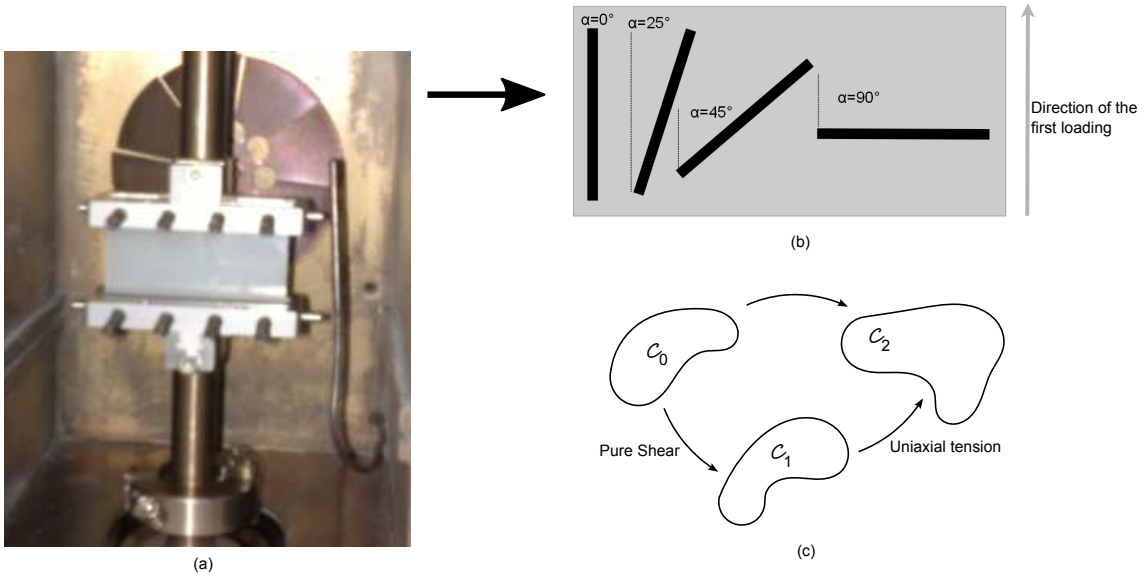

Figure 3.2: Experimental device used to highlight induced anisotropy by Mullins effect (a) pure shear test, (b) geometry of the cut specimens inside the pure shear specimen, (c) definition of the configurations, (C_0) initial configuration, (C_1) configuration after the pure shear test, (C_2) configuration after the pure shear and tensile tests.

change of direction. The intermediary orientations $\alpha = 25°$ and $\alpha = 45°$ present a behavior between a first and second loadings, the stress softening is more important for the orientation of $\alpha = 25°$ than for the orientation of $\alpha = 45°$ but the two curves come back on the same point on the first loading curve. These conclusions are the same as previously shown on a RTV silicone [Machado *et al.*, 2012b].

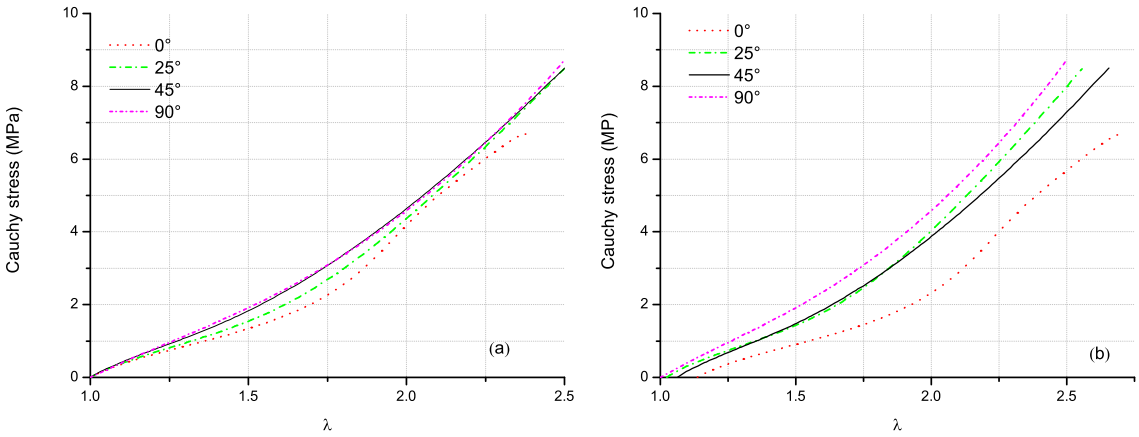

Figure 3.3: Influence of the angle between the first and second loadings on the stress softening compared to (a) configuration C_1, i.e. without taking into account the permanent set after the first loading and (b) compared to configuration C_0, i.e. by taking into account the permanent set after the first loading

It is also proposed to represent these four tensile tests by taking into account the complete history of the material i.e. compared to the initial configuration C_0 (cf. Fig.3.2(c)), i.e.

the permanent set generated by the pure shear test is now taken into account. The results are presented in Fig.3.3(b). The same stress softening as in Fig.3.3(a) is observed, and also the amount of permanent set endured lasting the pure shear test for the different samples. It is observed that more the orientation is close to the first loading direction more the permanent set is important. Indeed, for an orientation of $\alpha = 0°$ it can be observed an initial permanent set (due to the pure shear test) of $\lambda_{resid} = 1.136$ and at the opposite for the sample cut at $\alpha = 90°$ the initial permanent set is null. These results are similar to those obtained in literature [Machado *et al.*, 2012b].

3.3 Constitutive equation

3.3.1 General form

Recently, Rebouah *et al.* [2013] developed a constitutive equation written with strain invariants to predict the anisotropic stress softening in filled silicone rubbers but without permanent set. Based on the idea of Govindjee and Simo [1992], the strain energy density of the material $\mathcal{W}_{\text{silicone}}$ is additively decomposed into two parts: one that represents the strain energy of the chains linked to filler $\mathcal{W}_{cf}$ and an other part that represents the strain energy of the chains linked to other chains $\mathcal{W}_{cc}$. The total strain energy density is thus $\mathcal{W}_{\text{silicone}} = \mathcal{W}_{cc} + \mathcal{W}_{cf}$. Rebouah *et al.* [2013] considered that only $\mathcal{W}_{cf}$ can evolve with the Mullins effect. In our approach, it is also proposed to describe the permanent set by means of $\mathcal{W}_{cf}$. Thus $\mathcal{W}_{cf}$ is represented by an anisotropic strain energy function that can record the deformation history of the material. Any micro-sphere model defined by a spatial direction repartition $\mathbf{A}^{(i)}$ can be chosen. The dilatation in each direction is defined by means of ${I_4}^{(i)} = \mathbf{A}^{(i)}.\mathbf{C}\mathbf{A}^{(i)}$ where $\mathbf{C}$ is the right Cauchy-Green deformation tensor, defined by $\mathbf{C} = \mathbf{F}^T\mathbf{F}$, and $\mathbf{F}$ is the deformation gradient. The general form of the model is:

$$\mathcal{W}_{\text{silicone}} = \mathcal{W}_{cc}(I_1, I_2) + \sum_{i=1}^{n} \omega^{(i)} \mathcal{F}^{(i)} \mathcal{W}_{cf}^{(i)}(I_4^{(i)}). \tag{3.1}$$

$\mathcal{W}_{cc}$ is an hyperelastic energy density, I_1, I_2 are the first and second strain invariants of $\mathbf{C}$. $\mathcal{W}_{cf}^{(i)}$ is the hyperelastic strain energy associated with each direction and $\omega^{(i)}$ represents the weight of each direction. They are given by Bazant and Oh [1986], $\mathcal{F}^{(i)}$ is the Mullins effect evolution function. The HTV silicone does not present strain hardening, thus it is decided to use a strain energy that is not presenting a large increase of slope with deformation. The Mooney [1940] strain energy function is chosen for $\mathcal{W}_{cc}$ and a particular form is proposed for $\mathcal{W}_{cf}$. Previously (Rebouah *et al.* [2013]) the quadratic equation proposed by Kaliske [2000] was used. Nevertheless for this material this equation presents a stress hardening too important to represent the considered material, thus a function with a few hardening is used:

$$\text{if} \quad {I_4}^{(i)} \geq 1 \quad \mathcal{W}_{cf}^{(i)}(I_4^{(i)}) = \tfrac{K}{2} \int \sqrt{\frac{I_4^{(i)} - 1}{I_4^{(i)}}} dI_4^{(i)} \quad \text{else} \quad 0 \tag{3.2}$$

where K is the only material parameter. It is to note that it is considered here that the strain energy in each direction is considered only in tension.

Rebouah *et al.* [2013] proposed an evolution function which depends on the first and fourth invariants with only one material parameter η. The evolution function is the product of three terms. The first is an isotropic term which depends only on the first invariant and represents the global deformation of the material (similar to isotropic approaches), the second represents the maximal deformation of each direction of the material and the third the triaxiality of the loading state. In this paper, it is proposed to adapt the constitutive equation to represent both stress softening and permanent set. For the HTV silicone rubber, the isotropic part is useless, then it is omitted here. The evolution of the stress softening is then different for this material the powers of the two terms of the evolution function are changed and can be considered as parameters. The proposed function is :

$$\mathcal{F}^{(i)} = 1 - \eta \left(\frac{I_{4\,\max}^{(i)} - I_4^{(i)}}{I_{4\,\max}^{(i)} - 1} \right)^{\beta} \left(\frac{I_{4\,\max}^{(i)}}{I_{4\,\max}} \right)^{\gamma} \tag{3.3}$$

As proposed in literature by Zuñiga and Beatty [2002b], the stress-softening is described by the difference between the current strain and the maximum strain. The first term of the equation is the ratio of this difference between the current and undeformed states. The second term represents the triaxiality of the strain by the ratio of the strain in one direction compared to the maximum one. The powers assigned to each term must be chosen to represent at the best the mechanical behavior of the material and to avoid numerical problems. It is to note that these functions are phenomenological and their form is not motivated by micro mechanical observations.

The parameters η, β and γ influence simultaneously the stress softening and the permanent set of the material. $I_{4\max}^{(i)}$ represents the maximal value of $I_4^{(i)}$ for the whole material history for each direction and $I_{4\,\max}$ represents the maximal value of $I_4^{(i)}$ for the whole material history and all directions. To control the permanent set a strong restriction proposed by Rebouah *et al.* [2013] is suppressed here, the evolution function $\mathcal{F}^{(i)}$ is allowed to become negative. That means that the zero stress of a direction is no longer reach for zero deformation but for a deformation depending on the parameter η. It is to note that the evolution function $\mathcal{F}^{(i)}$ depends on two different maximal values of the fourth invariant, i.e in the considered direction, and for the whole material. Finally the Cauchy stress is obtained by:

$$\sigma_{\text{silicone}} = \boldsymbol{\sigma}_{cc} + \boldsymbol{\sigma}_{cf} - p\mathbf{I} \tag{3.4}$$

Where $\boldsymbol{\sigma}_{cc}$ is the part of the Cauchy stress that represents the chains linked to other chains and $\boldsymbol{\sigma}_{cf}$ the part of the Cauchy stress that represents the chains linked to fillers, expressed as:

$$\boldsymbol{\sigma}_{cc} = 2\mathbf{B}\frac{\partial W_{cc}}{\partial I_1} + 2\left(I_1\mathbf{B} - \mathbf{B}^2\right)\frac{\partial W_{cc}}{\partial I_2} \tag{3.5}$$

$$\boldsymbol{\sigma}_{cf} = 2\sum_{i=1}^{42} \omega^{(i)} \mathcal{F}^{(i)} \frac{\partial W_{cf}}{\partial I_4^{(i)}}^{(i)} \mathbf{F}\mathbf{A}^{(i)} \otimes \mathbf{A}^{(i)}\mathbf{F}^T \tag{3.6}$$

where the 42 directions repartition proposed by Bazant and Oh [1986] were chosen, in this study.

3.3.2 Validity of the model

It remains to verify that the presented model is in agreement with the requirements of thermodynamics (see e.g. Coleman and Gurtin [1967]). If only isothermal processes is considered, the Clausius-Duhem inequality must be satisfied

$$-\frac{\partial \mathcal{W}_{\text{silicone}}}{\partial I_{4\,\max}^{(i)}} \dot{I}_{4\,\max}^{(i)} \geq 0 \tag{3.7}$$

$$-\frac{\partial \mathcal{W}_{\text{silicone}}}{\partial I_{4\,\max}} \dot{I}_{4\,\max} \geq 0 \tag{3.8}$$

where $\dot{I}_{4\,\max}^{(i)} \geq 0$ and $\dot{I}_{4\,\max} \geq 0$ are the maximum deformation increase rates. By means of manipulations of Eqs. (3.7), (3.8) and (3.1), it can be easily established the next sufficient relations with the functions $\mathcal{F}^{(i)}$:

$$\frac{\partial \mathcal{F}^{(i)}}{\partial I_{4\,\max}^{(i)}} \leq 0 \quad \forall i \tag{3.9}$$

$$\frac{\partial \mathcal{F}^{(i)}}{\partial I_{4\,\max}} \leq 0 \quad \forall i \tag{3.10}$$

Considering, the generic form of the evolution constitutive equation (5.5), it can be explicitely written that:

$$\begin{aligned} \frac{\partial \mathcal{F}^{(i)}}{\partial I_{4\,\max}^{(i)}} &= -\eta\alpha \frac{\left(I_{4\,\max}^{(i)}-1\right)-\left(I_{4\,\max}^{(i)}-I_4^{(i)}\right)}{\left(I_{4\,\max}^{(i)}-1\right)^2} \left(\frac{I_{4\,\max}^{(i)}-I_4^{(i)}}{I_{4\,\max}^{(i)}-1}\right)^{\beta-1} \left(\frac{I_{4\,\max}^{(i)}}{I_{4\,\max}}\right)^{\gamma} \\ &\quad -\eta\beta \frac{1}{I_{4\,\max}} \left(\frac{I_{4\,\max}^{(i)}-I_4^{(i)}}{I_{4\,\max}^{(i)}-1}\right)^{\beta} \left(\frac{I_{4\,\max}^{(i)}}{I_{4\,\max}}\right)^{\gamma-1} \end{aligned} \tag{3.11}$$

$$\frac{\partial \mathcal{F}^{(i)}}{\partial I_{4\,\max}} = -\eta\beta I_{4\,\max}^{(i)} \left(\frac{I_{4\,\max}^{(i)} - I_4^{(i)}}{I_{4\,\max}^{(i)} - 1}\right)^{\beta} \left(\frac{I_{4\,\max}^{(i)}}{I_{4\,\max}}\right)^{\gamma-1} \tag{3.12}$$

To verify Eqs (3.9) and (3.10), the conditions to verify are $\alpha > 0$, $\beta > 0$ and $\left(I_{4\,\max}^{(i)} - 1\right) - \left(I_{4\,\max}^{(i)} - I_4^{(i)}\right) > 0$. This last condition is automatically verified if $I_4^{(i)} \geq 1$. It is verified for $I_4^{(i)} \leq 1$ by means of Eq (3.1) as no energy is considered in compression, that means that this term becomes 0.

3.4 Simulations of the model

To validate the model, it is proposed to compare its simulations to the different mechanical tests. The values of the material parameters were fitted on the different mechanical tests. The obtained values are: $C_1 = 0.3$ MPa, $C_2 = 0.15$ MPa, $K = 1.6$ MPa, $\eta = 5$, $\beta = 0.5$ and $\gamma = 2.5$.

3.4.1 HTV on a tensile test

First the cyclic tensile test presented in Fig.3.1 is compared to the prediction of the model. The results obtained are illustrated in Fig.3.4. These results are satisfactory since it can be observed that the Mullins effect and the permanent set are quite well described by the model.

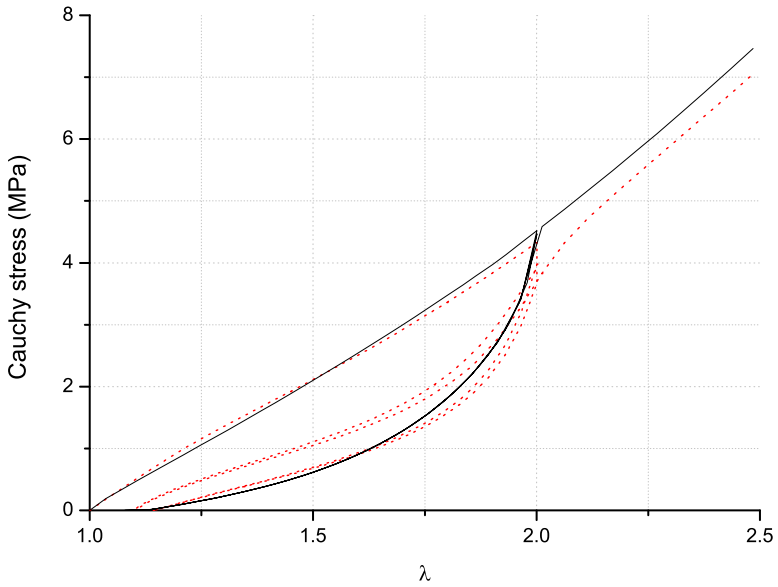

Figure 3.4: Comparison of the prediction of the model (full lines) to experimental data (dotted lines)

3.4.2 HTV on a tensile test after a pure shear test

In this section, it is proposed to compare the model to the experimental results of the pure shear test followed by tensile tests according to different orientations. A comparison between the model and the tests is proposed in Fig.3.5. It is to note that the first and second loadings (and thus the elongation) do not correspond to the same test. For each test the definition of λ corresponds to the elongation in the tensile test direction whatever the experiment. Every simulated orientations present a similar behavior to the experimental results, thus the same observation as the one made in paragraph 2.3 can be done. Furthermore it is shown that the model is able to take well into account the induced anisotropy. Finally for the curve at $\alpha = 25°$ it is observed that the second loading curve of the model present a rupture of slope about $\lambda = 1.8$. This phenomenon is due to the discretization along the 42 directions of Bazant and Oh [1986]. The problem is that the discretization in 42 directions creates a numerical anisotropy, as explained in literature [Gillibert *et al.*, 2010]. This phenomenon can be avoided with a full integration in space, nevertheless the computational formulation become more complicated and it becomes very time consuming. Despite discretization problems, these results proved the ability of the model to take into account the induced anisotropy and the permanent set.

3.4.3 Analysis of the model simulations

In this part, it is proposed to analyze the evolution of the stress softening along the 42 spatial directions. The principal request directions during a cycling tensile test are observed along the direction of tension $\vec{x}$, where the maximal deformations are reached

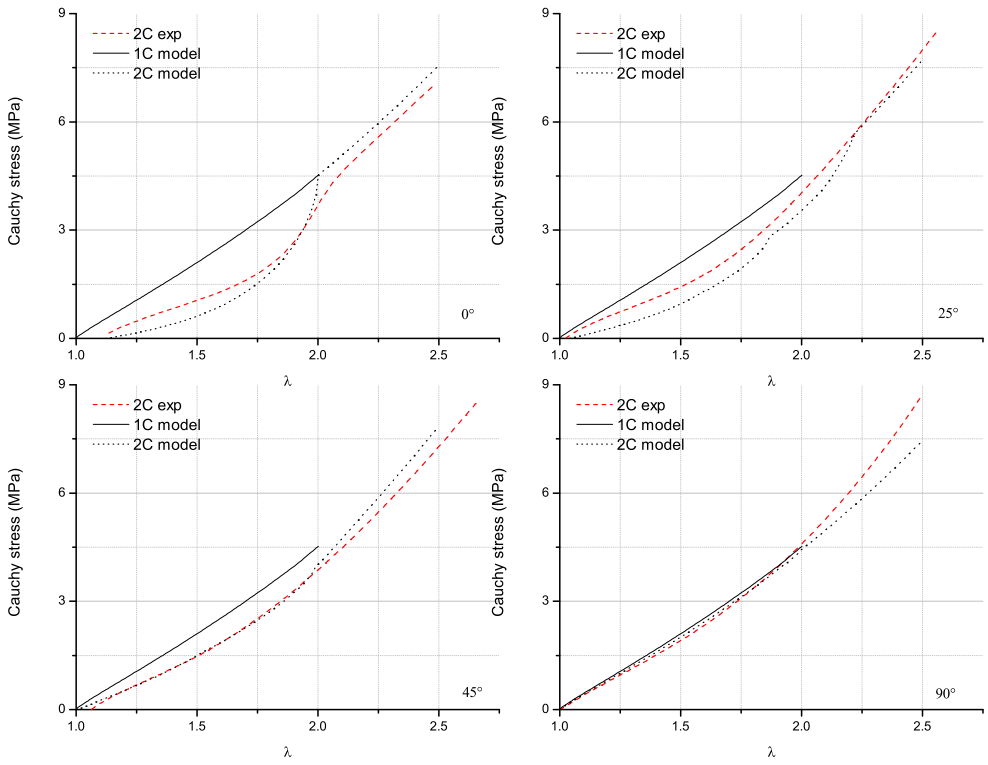

Figure 3.5: Comparison with experimental oriented data and the model. The black full lines represent the theoretical first loading in uniaxial tension (1Cmodel), the black dotted lines represent the second loadings (i.e. the tensile test) for the different orientations (2Cmodel). The red dashed lines represent the experimental results for the different oriented samples of tensile tests after the pure shear test (2Cexp)

for different cycles until a maximal elongation of $\lambda = 1.5$, then $\lambda = 2.$ and $\lambda = 2.5$. The 42 directions are represented in projection in the plan $(\vec{z}, \vec{y})$ in Fig.3.6 as Miehe *et al.* [2004]. It is to note that many directions have the same angle with the $\vec{x}$ direction. They are summarized by the definition of 4 circles.

The stress σ_{xx} which corresponds to the stress in the tensile direction. It is by construction the tensorial sum of stresses along the 42 directions [Bazant and Oh, 1986]. More a direction is closer from direction $\vec{x}$, more its contribution to σ_{xx} is important. All the directions that belong to a same circle provide the same contribution in the case of uniaxial tension in direction $\vec{x}$. Thus, for clarity of the figure only one direction per circle is presented. The stress strain behavior of each direction is presented in Fig.3.7. It appears that the most loaded direction is direction 1, which is consistent since it corresponds to the tensile direction $\vec{x}$. Nevertheless it is observed that the directions which belong to the circle 3 (4-5-6-7) and to the circle 4 (18-19-20-21) endure also an important deformation and generate important stresses. It can also be observed that the directions which belong

to the circle 2 (10-11-12-13-14-15-16-17) have very few influence, and the directions which belong to the circle 1 (2-3-8-9) are equal to zero as they are loaded only in compression. Besides direction 1, circles 3 and 4 present a negative part of the Cauchy stress during second loadings, that means that these directions present a permanent set. The directions that belong to circle 1 and 2 are still superior or equal to zero thus they do not present permanent set.

The evolution function generates a new equilibrium position, meaning that the zero stress state is no longer reached for zero deformation. This new equilibrium depends on the maximum deformation and is thus more important for directions close to direction $\vec{x}$. This is illustrated by Fig.3.8. It is observed that along the direction 1, the circle 3 and 4 the evolution function becomes negative, thas means that the material presents a zero stress, and thus a permanent set. It is to note that the directions where the evolution function become negative are the same direction for which the stress become negative and thus directions which generate permanent set. For this study the 42 directions proposed by Bazant and Oh (1986) were used, nevertheless the other directions repartition proposed by the same author can also be used. It was proved that the results observed are identical but they are not presented in the paper.

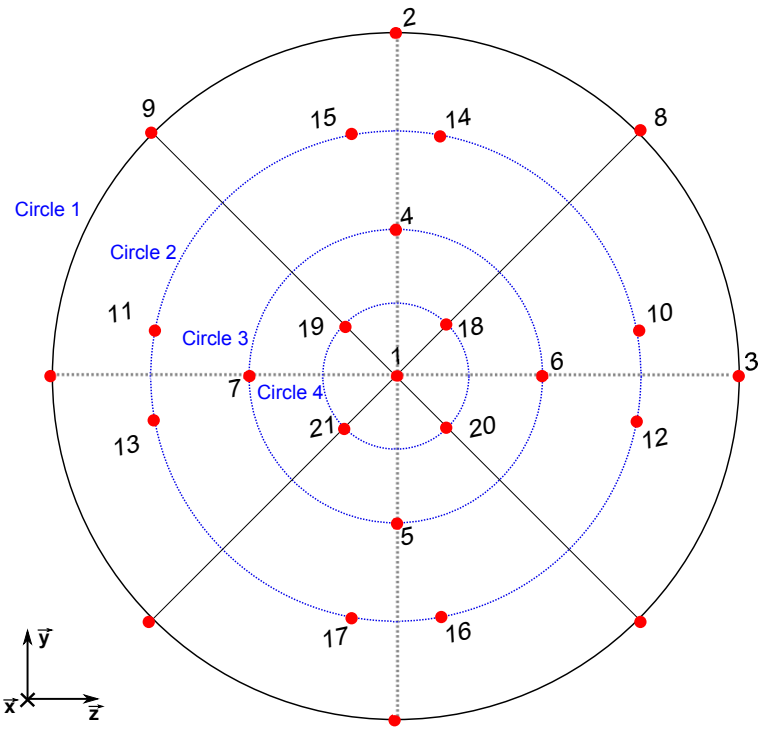

Figure 3.6: Representation of the 42 Bazant and Oh directions in the plan $(\vec{z}, \vec{y})$

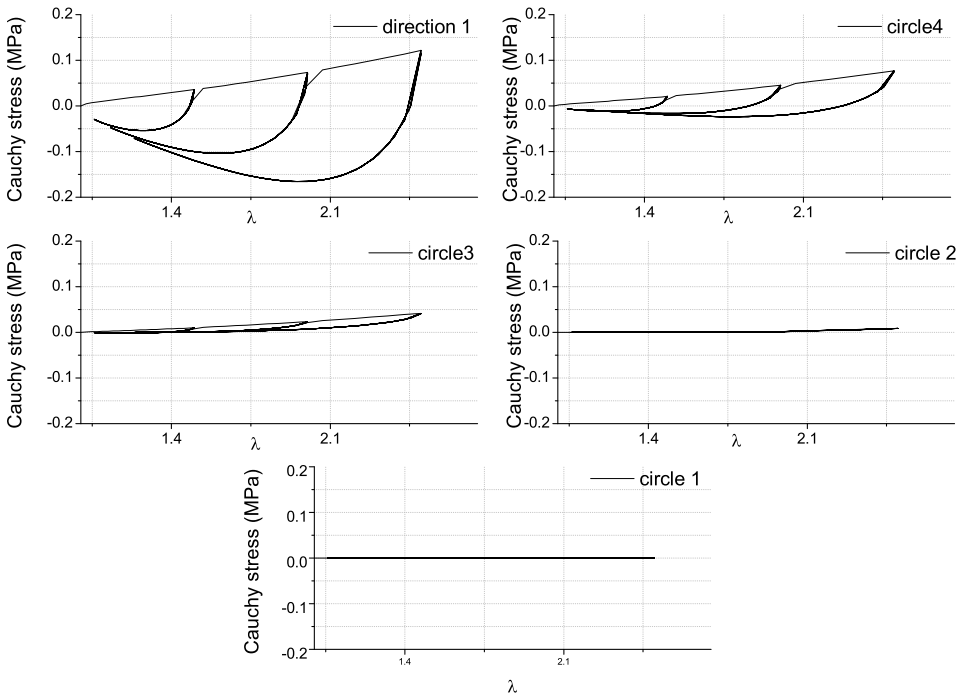

Figure 3.7: Representation of the first component of the stress tensor (σ_{xx}) for cyclic tensile test up to $\lambda = 2.5$

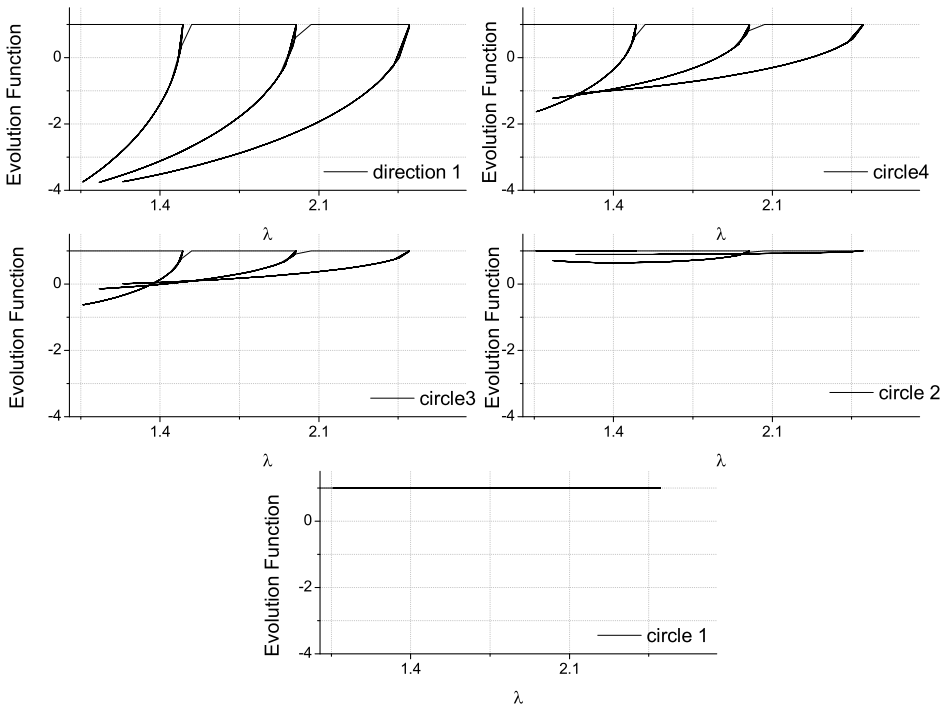

Figure 3.8: Representation of the evolution function for cyclic tensile test up to $\lambda = 2.5$

3.5 Adaptation of the constitutive equation to soft tissues

3.5.1 Adaptation of the model

It is proposed here to adapt the general form of the model previously described to non initially isotropic materials, i.e. soft tissues. This anisotropy is imputed to the presence of fibers, often collagen [Holzapfel, 2000], into the matrix of the tissue. In many soft tissues, there exist two main fibers orientations (the model will be developed for 2 directions, but the proposed principle would be the same for more directions). The orientation of these fibers depends on the studied soft tissues [Natali *et al.*, 2009; Schröder *et al.*, 2005; Li and Robertson, 2009; Ehret and Itskov, 2009; Peña, 2011]. As classically done in literature, it is proposed to model the soft tissues mechanical behavior as the sum of three terms. The first part represents the behavior of the matrix, the second and third parts represent respectively the mechanical behavior of the fibers oriented in the two directions.

$$\mathcal{W}_{\text{soft-tissue}} = \mathcal{W}_{\text{matrix}} + \mathcal{W}_{\text{fiber1}} + \mathcal{W}_{\text{fiber2}} \tag{3.13}$$

It is also often assumed that the fibers can only endured tension, i.e. that no stress is generated in compression. The principle is to propose a strain energy that can simulate the stress softening both in the matrix and in the fibers. In the matrix, an initially isotropic strain energy is considered, which is similar to the one proposed for silicone rubbers in part 3. The same form is thus proposed

$$\mathcal{W}_{\text{matrix}} = \mathcal{W}_{cc}(I_1) + \sum_{i=1}^{n} \omega^{(i)} \mathcal{F}^{(i)} \mathcal{W}_{cf}^{(i)}(I_4^{(i)}). \tag{3.14}$$

Different hyperelastic strain energies are used, as soft tissues present more strain hardening than silicone rubber. Classical strain energies are chosen for $\mathcal{W}_{cc}(I_1)$ [Demiray, 1972; Delfino *et al.*, 1997] and for $\mathcal{W}_{cf}^{(i)}$ [Kaliske, 2000], they are defined as:

$$\mathcal{W}_{cc}(I_1) = C_1 exp\left(C_2(I_1 - 3)^2 - 1\right) \tag{3.15}$$

$$\mathcal{W}_{cf}^{(i)} = K(I_4^{(i)} - 1)^2 \tag{3.16}$$

where C_1, C_2 and K are material parameters. The evolution function $\mathcal{F}^{(i)}$ of the matrix is the same as the one used for silicone rubber model, described in Eq.(5.5).
The strain energy for fiber j is the product of an hyperelastic strain energy $\mathcal{W}_{\text{cf-fiber}_j}$ and an evolution function $\mathcal{F}_{\text{fiber}^{(j)}}$ to describe the Mullins effect:

$$\mathcal{W}_{\text{fiber1}} = \mathcal{F}_{\text{fiber}^{(j)}} . \mathcal{W}_{\text{cf-fiber}_j} \tag{3.17}$$

The hyperelastic strain energy of each fiber is noted $\mathcal{W}_{\text{cf-fiber}_j}$ [Holzapfel *et al.*, 2000] is expressed as:

$$\mathcal{W}_{\text{cf-fiber}_j} = \frac{K_f}{2} \exp(I_4^{(j)} - I_{4_0}^{(j)})^2 \tag{3.18}$$

K_f is a material parameter and $I_{4_0}^{(j)}$ matches to the value of $I_4^{(j)}$ for which the stress hardening of the material appears. Finally, due to the hypothesis of tension in the fiber, the evolution function is also adapted for the fibers, where only $I_4^{(j)}$ is necessary. A

simplified form of the evolution function is used compared to the one used in Eq.(3).Indeed for the fiber only one direction is considered, that means that the third term that took into account the triaxiality is not necessary. Only the second term is consistent

$$\mathcal{F}_{\text{fiber}}^{(j)} = 1 - \eta_f \left(\frac{I_{4\,\max}^{(j)} - I_4^{(j)}}{I_{4\,\max}^{(j)} - 1} \right)^{\beta} \tag{3.19}$$

Where η_f and β are the material parameters which allows to take into account the stress softening and the permanent set of the fibers. It is to note that in this part, it is considered that the material cannot endured compression, thus the stress cannot become negative in any direction. Nevertheless it generates the begining of the permanent set for the material. This difference compared to the last model (for rubber like materials) is due to the stress hardening of soft tissues which is very important, and thus the evolution function must be adapted to correctly describe the phenomena.

3.5.2 Comparison with experimental data

To highlight the ability of the model to mimic soft tissues, it is proposed to compare it by means of the experimental data of Peña and Doblaré [2009] considering first and second loadings at different maximum deformation in ovine vena cava during uniaxial tension. The orientation of the fibers was chosen at $\alpha = 45°$. These results were obtained for the following values of the different material parameters $C_1 = 0.28\text{MPa}; C_2 = 0.16\text{MPa}; K = 0.13\text{MPa}; K_f = 0.5\text{MPa}; \eta = 2., \eta_f = 5$ and $\beta = 2$. As observed in Fig.3.9 the experimental

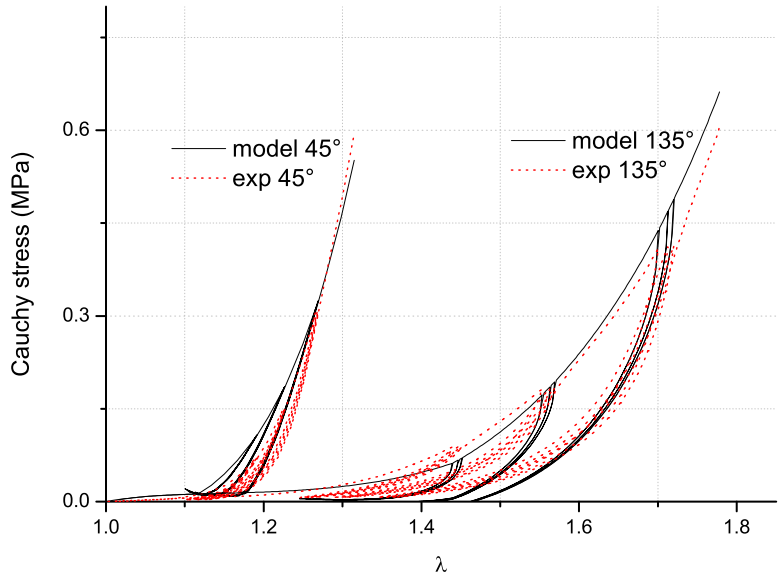

Figure 3.9: Experimental data and comparison with the model for oriented sample of 45° and 135° in the tissue

data obtained for loading reloading cycles at different stretches are well described by the

model. Fig.3.9(a) represents the theoretical tensile test for a tensile test along the axial direction for a value of $\alpha = 45°$ and Fig.3.9(b) along the circumferential direction. For both tests it is observed that the hyperelastic behavior, the stress softening, the permanent set and the initial anisotropy are well taken into account. In this case the induced anisotropy is not visible on the experimental data, nevertheless the model can also take it into account.

3.6 General conclusion

As explained and shown in this chapter a simple model is proposed here to take into account several effects of the Mullins effect. This model is adapted for both rubber like materials and soft tissues. Compared to literature Diani *et al.* [2006a]; Merckel *et al.* [2012] the major difference is that the permanent set and the stress softening are considered as correlated phenomena and thus the material parameters allow to represent simultaneously the stress softening and the permanent set. Due to the use of two different materials (HTV and soft tissues) different expressions were used for the strain energies and the evolution functions. Nevertheless the discretization by a micro sphere model represents well the both material. Finally, by means of the extension of the model to soft tissues, the initially anisotropy of the materials can be taken into account independently of the induced anisotropy due to the stress softening. For both of these materials the constitutive equations were successfully compared to experimental data to take into account simultaneously the stress softening of the material, the permanent set, the induced anisotropy or the initial anisotropy of the material. Furthermore, due to the formulation in strain invariant of the constitutive equations, can easily be implemented into a Finite Element code.

The authors thank Professor Estefania Peña for helpful information on the experimental data of Peña and Doblaré [2009].

Chapter

4 Viscoelasticity of initially isotropic materials

Some part of this chapter have been published and can be found in the following reference

- **M. Rebouah, G. Chagnon**, 2014, Extension of classical viscoelastic models in large deformation to anisotropy and stress softening, International Journal of Non-Linear Mechanics, 61, 54-64

Contents

4.1 General introduction

As presented in the previous chapters the stress softening, the induced anisotropy and the permanent set can be taken into account in the modeling of rubber like materials and extended to soft tissues. Nevertheless, as presented in Chapter 1, most of materials present also a viscoelastic behavior. This chapter proposed a way to take into account these viscous effects. For this purpose, the chapter can be divided in three main parts.
First an experimental part to characterize the material used in this section: a filled NBR. This study begin by the determination of the glass transition temperature by means of Differential Scanning Calorimetry (DSC) and Dynamic Mechanical Analysis (DMA) tests. Then mechanical tests are performed to highlight the viscoelasticity of the material. In this way, the influence of the strain rate is highlighted, cyclic tensile tests with imposed relaxation times and intern subloop are carried out to emphasize the influence of each non linear phenomena.
The second part is mainly issued from Rebouah and Chagnon [2014] and presents the extension of two classical viscoelastic models by means of a 3D micro spherical homogenization. The two classical models recently studied by Petiteau *et al.* [2012] are studied a Convolution Integral Model (CIM) and an Internal Variable Model (IVM). This section is exclusively theoretical, simulations are proposed. The differences induced by the two formulations are evaluated by means of simulated classical mechanical tests: uniaxial, planar and equibiaxial tension are compared. Then an initial anisotropy is induced by means of the spatial repartition used in the 3D homogenization. Finally, a stress softening term is added in the constitutive equation. All the simulations highlight the capacity of the formulation.
Finally, the last section of this chapter presents an adaptation of the theoretical method presented in the second part to preexisting models. Based on a 3D micro spherical homogenization, it is proposed to extend four classical models of IVM type. First the model developed by Huber and Tsakmakis [2000] which is defined by a linear evolution equation and then the micro mechanical model proposed by Bergstrom and Boyce [1998, 2001]. The elastic part of the Bergstrom and Boyce [1998, 2001] model is either represented by a Neo Hookean, a Mooney Rivlin or (as initially proposed) by the eight chain model. The robustness of the models is evaluated by means of comparisons with the experimental data obtained in first section.

4.2 Experimental Part

The experimental study was lead on an industrial filled NBR, due to confidentiality the composition cannot be revealed. Several tests were performed to highlight its behavior. First DMA and DSC tests are presented to determine the glass transition temperature of

the material used. Then, the strain rate influence is studied and cyclic tensile tests with imposed relaxation times and intern subloop are performed. These tests were performed to study the hysteresis loop associated to the material. It is to note that the NBR used, present an initial isotropic behavior.

4.2.1 Glass transition temperature

A DSC is performed by using a Q200 TA instruments at a heating rate of $10°C.min^{-1}$ on a NBR sample. The test was carried out for a temperature cycle from 50°C to -80°C and back to 50°C. The material glass transition temperature was obtained as the inflection temperature measured and the results are presented in Fig.4.1. It appears that the glass transition temperature of the material is different for the cooling and the heating range. For the cooling range the glass transition temperature is obtained at approximately -13.8°C and for the heating at -7.2°C.

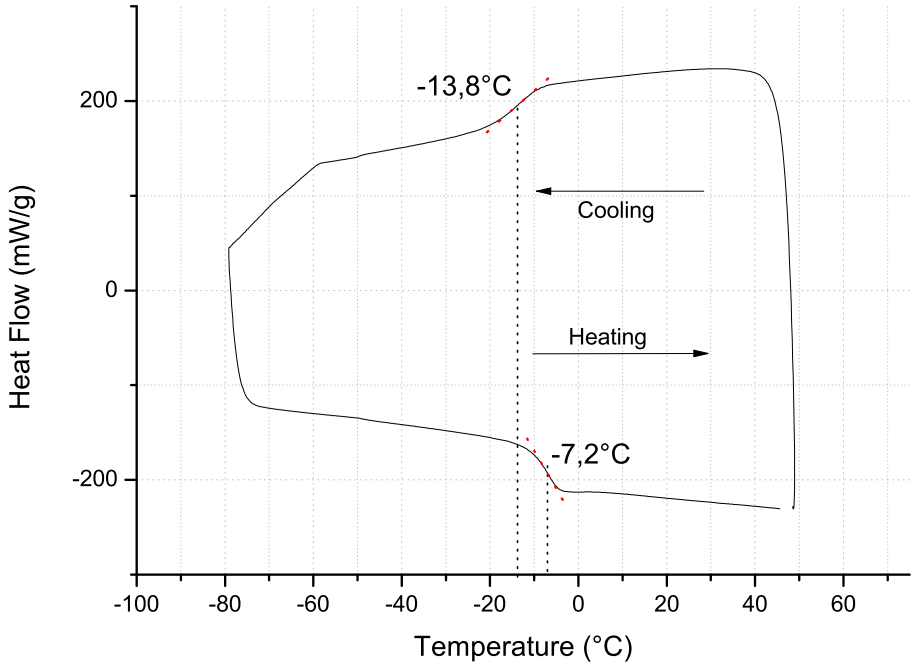

Figure 4.1: DSC performed on NBR at a heating rate of $10°C.min^{-1}$

The material was also tested in DMA at a frequency of 1Hz, for strain amplitude of 0.5% and at a heating rate of $2°C.min^{-1}$ with a pre-stretch of 15%. The results obtained are presented in Fig.4.2. As for the DSC the glass transition temperatures are different for the cooling and the heating range. For the cooling, a glass transition temperature of approximately -16.0°C is obtained and -6.5°C in heating.
The results obtained with both techniques are similar. Indeed, with these two tests it can be concluded that a glass transition temperature of approximately -7.0°C is obtained in

heating, and -15.0°C in cooling. For the study of elastomers the glass transition considered is often the one obtain in cooling [Yi *et al.*, 2006; Diani *et al.*, 2013; Rey *et al.*, 2013]. All the following tests are performed at an ambient room temperature ($\theta > 23$°C), nearly up to the glass transition temperature.

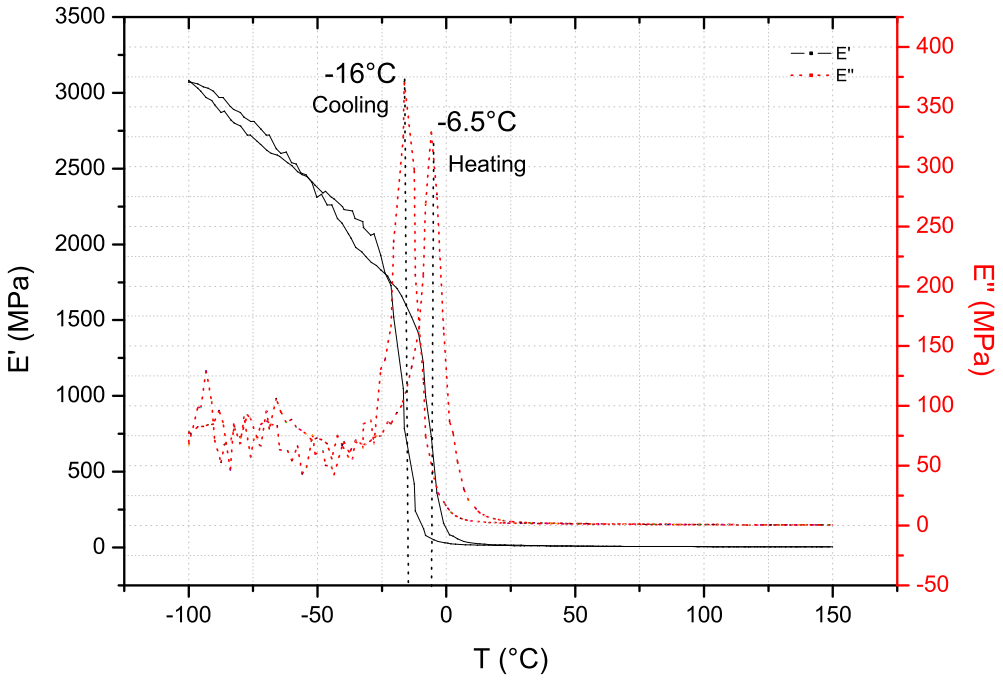

Figure 4.2: DMA on NBR at a frequency f=1Hz and a strain amplitude=0.5% at a heating rate of 2°C.min^{-1}

4.2.2 Influence of the strain rate

The second test carried out is a cyclic tensile test up to $\lambda = 1.5$, $\lambda = 2$ and $\lambda = 2.5$. This test was performed at the following values of strain rate $\alpha = 0.00025\text{s}^{-1}$, $\alpha = 0.0016\text{s}^{-1}$, $\alpha = 0.01\text{s}^{-1}$ and $\alpha = 0.0166\text{s}^{-1}$. The obtained results are presented in Fig.4.3, it is observed that the strain rate influences the mechanical behavior of the material. More the strain rate is important more the stress hardening of the material is important too. This simple test highlights that the material presents an important stress softening between the first and the second loadings (Mullins effect) and a viscoelastic behavior. Moreover, the material presents also a residual strain that depends on the strain rate applied. Indeed more the strain rate is important more the amount of residual strain is important too. If the mechanical permanent set (supposed as damaged) is considered as constant for any strain rate, it is clearly highlighted that the viscous permanent set is dependent of the strain applied. No proportionality is observed between the curves at the different strain rates, this observation supposed that the influence of the strain rate is different on the hyperelastic behavior, the stress softening and the viscoelasticity of the material.

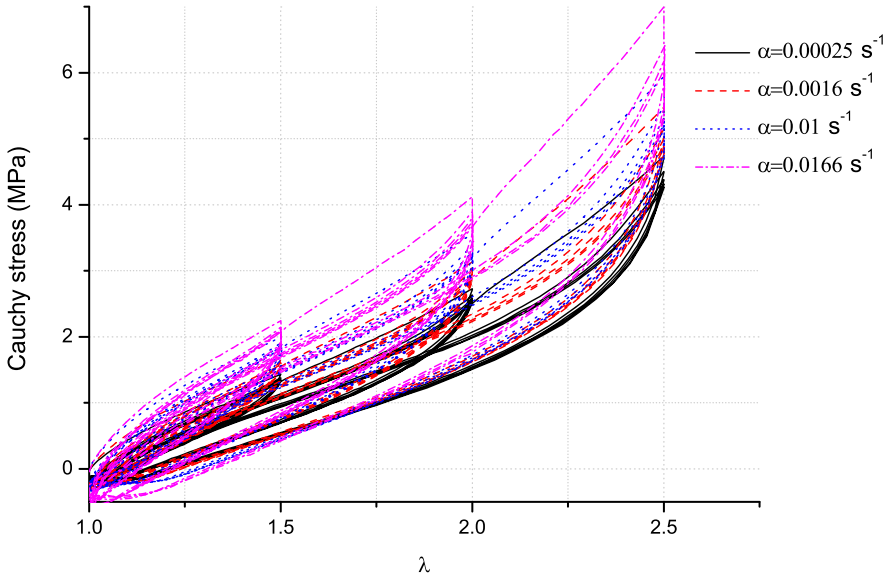

Figure 4.3: Influence of the strain rate on the mechanical behavior of NBR

4.2.3 Cyclic tests with imposed relaxation times

The third test performed on the material is a cyclic test containing several relaxation times as proposed by Lion [1997b] for instance. This test is carried out at two different strain rates: $\alpha = 0.00025\text{s}^{-1}$ and a $\alpha = 0.0166\text{s}^{-1}$. The different strain states reached and the relaxation times are defined by a cycle repeated five times. This cycle is designed as follow: a load up to $\lambda = 1.5$, 30 min of relaxation, a load up to $\lambda = 2$, 30 min of relaxation, and a load up to $\lambda = 2.5$, an unload up to $\lambda = 2$, 30 min of relaxation, an unload up to $\lambda = 1.5$, 30 min of relaxation and an unload up to $\lambda = 1$. This cycle is described at the top of the Fig.4.4. Even if this cycle is repeated five times for the two strain rates, only the two first cycles are presented for more clarity, it appears that after the second cycle the material presents the same behavior in the following cycle for the two strain rates, only the experimental errors are observed between these cycles, curves are overlapping. The results of the tests are presented in Fig.4.4, where the black full lines represent the relaxation test and the red dotted line represents the same test without relaxation times during loadings and unloadings (five cycles up to $\lambda = 2.5$).
Fig.4.4 highlights also that the material presents a stress softening between the first and the second cycles (Mullins effect), and it does not evolve for superior cycles. It is also observed that the residual strain is more important for high strain rates. The weak compression observed lasting the residual strain is due to the buckling of the sample. At each relaxation time, the stress endured by the material decreases until the curve gets on an equilibrium curve and the amount of overstress is highlighted. It is to note that the curves come back on those of the cyclic tests carried out without relaxation, thus it is assumed that the mechanical behavior is not modified by the relaxation times.

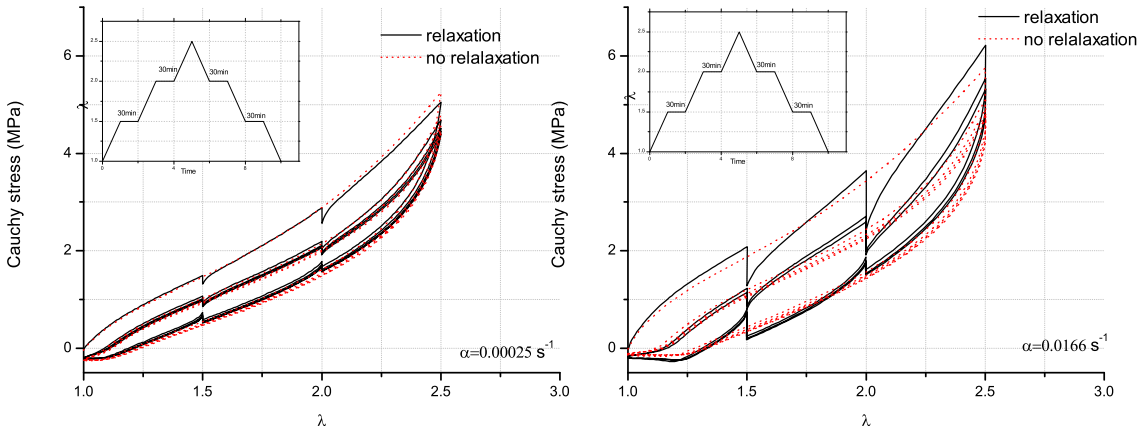

Figure 4.4: Comparison of relaxation tests at two strain rates (black full lines) and tests without relaxation (red dotted lines).

At the end of the relaxation time the curve reached a specific stress state for each strain state. That means that the material is on its equilibrium state, only a few viscous effects are represented at these points. Several equilibrium curves can be defined. The first equilibrium curve is defined for the first loading, the second equilibrium curve for the second loading (and other loading after) and an equilibrium curve for the unloading (which is overlapping for the first and second cycles). These three equilibrium curves are depicted in Fig.4.5(a) for a strain rate of $\alpha = 0.00025s^{-1}$ and in Fig.4.6(a) for a strain rate of $\alpha = 0.016s^{-1}$. The difference of stress between the load and the unload for the first and the second cycles can be deduced from these equilibrium curves as represented in Fig.4.5(b) and in Fig.4.6(b). It appears that the difference of stress between load and unload is much more important for the first cycle than for the second cycle for both strain rates. This difference is due to the stress softening of the material, indeed for the first cycle the difference observed is due to the stress softening and the viscous effects, for the second cycle this difference is only due to the viscous effects. Those observations are identical for both strain rates studied, nevertheless it appears that for a strain rate of $\alpha = 0.016s^{-1}$ the hysteresis of the equilibrium curves is weaker than the one at a strain rate of $\alpha = 0.00025s^{-1}$.

Finally, the Fig.4.7 represents all the equilibrium curves deduced from the cyclic test with imposed relaxation times for both strain rates. It appears that, as long that the global deformation endured by the material is "*small*" (inferior to 100%), the equilibrium curves are similar for the both strain rates. At a deformation of $\lambda = 2.5$ the difference between equilibrium curve is maximal and due to the lack of relaxation time imposed to the material. It explains the difference of stress reached for the both strain rates at the same strain state. However, it appears that the second loading curves and the unloading curves are very close for both strain rates, it can be supposed that most of the hysteresis is due to the viscous effects and that a permanent hysteresis could be neglected.

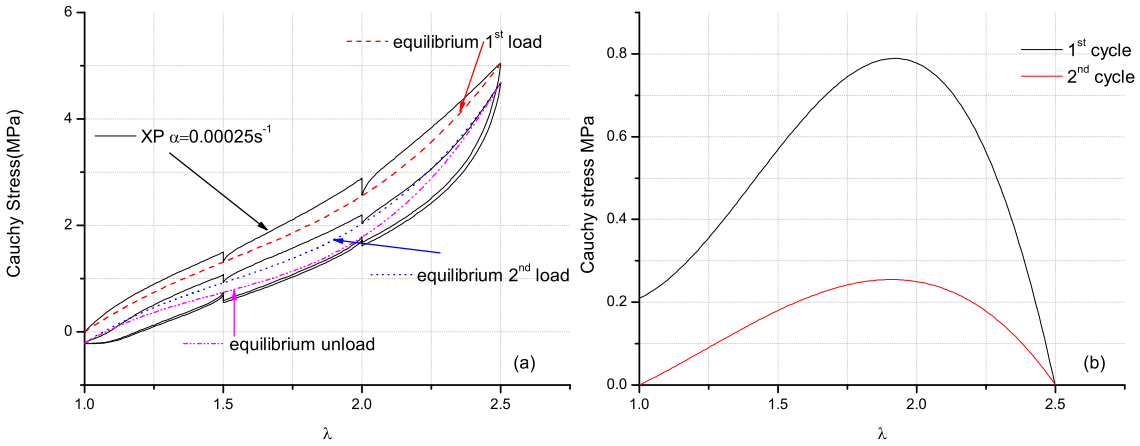

Figure 4.5: Equilibrium curve associated to the material for the cyclic tensile test (a) and the difference of the equilibrium curve between the loading and the unloading for the first and the second loading (b), at a strain rate $\alpha = 0.00025s^{-1}$

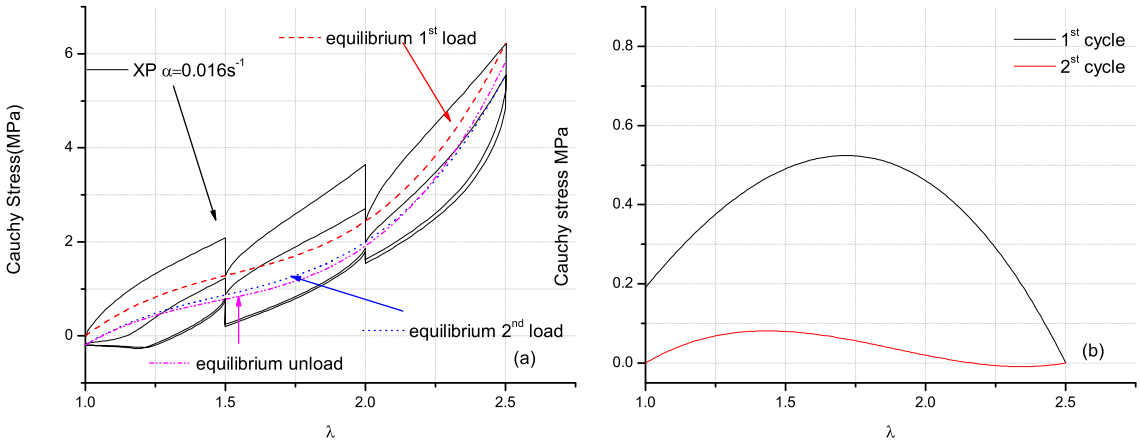

Figure 4.6: Equilibrium curve associated to the material for the cyclic tensile test (a) and the difference of the equilibrium curve between the loading and the unloading for the first and the second loading (b), at a strain rate $\alpha = 0.016s^{-1}$

4.2.4 Subloop tests

Finally, cyclic tests including interne loops (called subloop tests) are performed at two different strain rates: $\alpha = 0.00025\text{s}^{-1}$ and $\alpha = 0.0166\text{s}^{-1}$. A representation of the test is presented at the top of Fig.4.8 (a) and 4.9(a). The cycle is designed as follow: a loading up to $\lambda = 1.5$, an unloading up to $\lambda = 1.25$, a loading up to $\lambda = 2$, an unloading up to $\lambda = 1.75$, loading up to $\lambda = 2.5$, an unloading up to $\lambda = 2$, a loading up to $\lambda = 2.25$, an unloading up to $\lambda = 1.5$, loading up to $\lambda = 1.75$ and an unloading up to $\lambda =$, this represented is repeated five times for both strain rates. The results are presented in Fig.4.8 (a) and Fig.4.9(a). It appears that the first and the second loadings are very different due to the stress softening, but the unloading are overlapping. The third, fourth and fifth cycle are overlapping the second cycle, thus only the first and second cycle cyle are represented

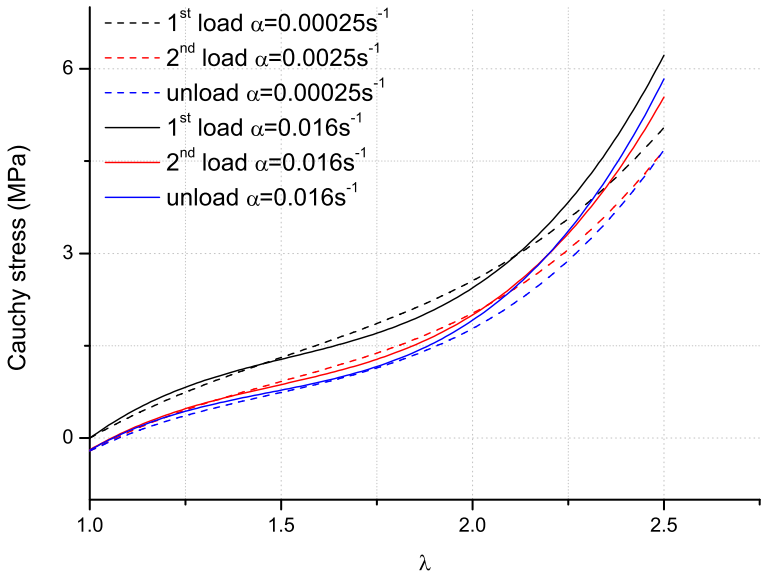

Figure 4.7: Equilibrium curve associated to the NBR material for the both strain rates

in the following figures and discussions for more clarity.

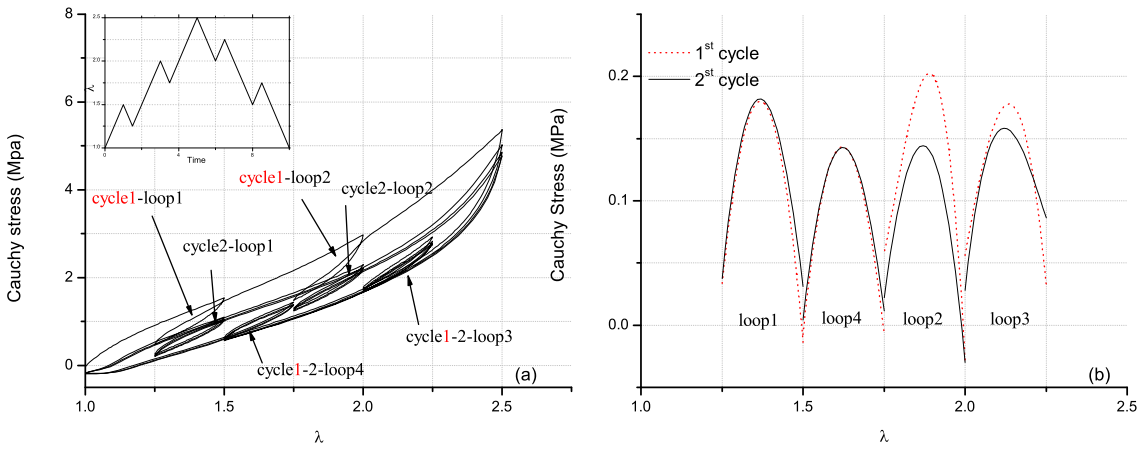

Figure 4.8: Subloop test for NBR sample at a strain rate of $\alpha = 0.00025\text{s}^{-1}$ (a) and the size of the hysteresis subloop (b).

It is proposed to study the size of the hysteresis subloops during the first and the second cycles at the both strain rates in Fig.4.8 (b) and Fig.4.9(b). It appears that the size of the hysteresis subloops are more important for a strain rate of $\alpha = 0.0166\text{s}^{-1}$ compared to $\alpha = 0.00025\text{s}^{-1}$. This difference is due to the viscous effects of the material that increase with the strain rate as highlighted in the previous experimental tests. Furthermore, it also appears that the hysteresis is more important for the the first cycle than for the second cycle, it supposed that a part of the hysteretic behavior is due to the stress softening.

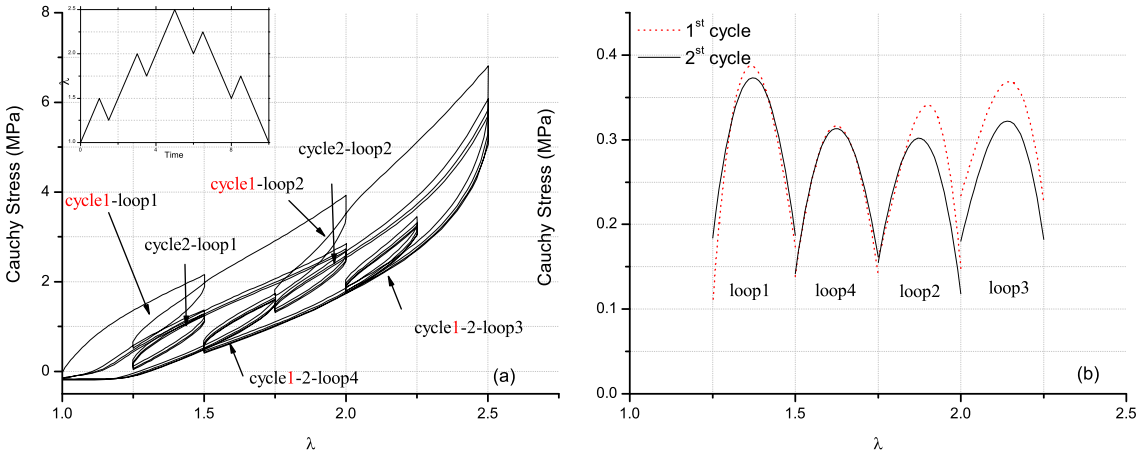

Figure 4.9: Subloop test for NBR sample at a strain rate of $\alpha = 0.0166\text{s}^{-1}$ (a) and the size of the hysteresis subloop (b).

Finally, it appears that the size of the hysteresis subloops are similar for the loading and unloading for both strain rates, except for the hysteresis of the first subloop which is greater than the others.

4.2.5 Discussion

The experimental tests performed on the filled NBR highlight that the material presents most of the non linear phenomena that can be observed for rubbers like materials. Indeed, stress softening, permanent set and viscous effects are emphasized. Cyclic tests with imposed relaxation time highlight the part of the mechanical behavior that corresponds to the equilibrium part and the overstress part. The cyclic tensile tests highlight too that the material present an hysteresis due to the viscous effects and stress softening for the first loading. The equilibrium curves are almost overlapping fro the second loading and unloading, thus it is conclude that permanent hysteresis is not a phenomena observed for this material. The subloop tests highlight that the size of the hysteresis is similar for all state of deformations, except for the first one in loading.

4.3 Micro sphere formulation of simple viscoelastic models

This section is purely theoretical and no comparisons with experimental data are proposed here. The point is to present a 3D homogenization of two classical models, an IVM and a CIM, by means of a micro spherical approach. The constitutive equations of the 3D homogenization are depicted and comparisons between both formulations are proposed. A way to describe an initial anisotropic behavior is presented and the proposed equations to take into account the Mullins effect of the last chapter are added to the viscoelastic model.

4.3.1 Presentation of the models

The two viscoelastic isotropic models used in this paper are those used by Petiteau *et al.* [2012]. The first one is an IVM deduced from the theory of Green and Rivlin [1957] and the second is a CIM deduced from the theory of Green and Tobolsky [1946]. These two models are quickly recalled in this section, in the incompressible framework.

4.3.1.1 Internal Variable Model

The simplest IVM for viscoelasticity was derived by Huber and Tsakmakis [2000] and is represented by a Zenner model. This model is based on the decomposition of the deformation gradient $\mathbf{F}$ between an elastic part $\mathbf{F_e}$, which represents the deformation gradient of a spring and an inelastic part $\mathbf{F_p}$, which represents the deformation gradient of a dashpot as illustrated in Fig.4.10. Thus, the deformation gradient $\mathbf{F}$ can be expressed as

$$\mathbf{F} = \mathbf{F_e}\mathbf{F_p} \tag{4.1}$$

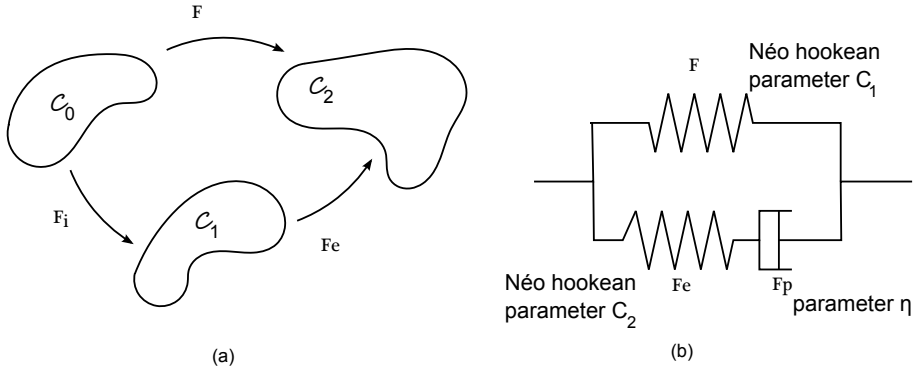

Figure 4.10: Representation of the different configurations by using a strain type internal variable (a) and the rheological representation of the components (b)

Classically it is considered, that there is no rotation in $\mathbf{F_p}$ and thus the rotation is only in the elastic part $\mathbf{F_e}$. This permits to keep unique the elastic-inelastic decomposition. Furthermore it is assumed that the material is incompressible, thus each deformation is defined as $\det \mathbf{F_e} = 1$ and $\det \mathbf{F_p} = 1$. The strain enery density associated to the rheological representation is defined by:

$$\mathcal{W}(\mathbf{F_e}, \mathbf{F_p}) = \mathcal{W}_1(\mathbf{F_e}) + \mathcal{W}_2(\mathbf{F_p}) \tag{4.2}$$

where $\mathcal{W}_1$ represents the strain energy density between the initial C_0 and the intermediary C_1 configuration and $\mathcal{W}_2$ the strain energy density between the intermediary C_1 and final C_2 configuration. According to the Second Principle of Thermodynamics

$$\mathcal{D}_{int} = \boldsymbol{\sigma} : \mathbf{D} - \dot{\mathcal{W}} \geq 0 \tag{4.3}$$

where $\mathcal{D}_{int}$ is the internal dissipation and $\mathbf{D}$ is the rate of deformation tensor. After some algebric manipulations described in Huber and Tsakmakis [2000] and Petiteau *et al.* [2012],

the second principle can be rewritten as

$$\left(\boldsymbol{\sigma} - 2\frac{\partial \mathcal{W}_1}{\partial \mathbf{B}}\mathbf{B} - 2\frac{\partial \mathcal{W}_2}{\partial \mathbf{B_e}}\mathbf{B_e}\right) : \mathbf{D} + 2\mathbf{F}^T\frac{\partial \mathcal{W}_2}{\partial \mathbf{B_e}}\mathbf{F_e} : \mathbf{D}_p \geq 0 \tag{4.4}$$

where $\mathbf{D}_p$ is the inelastic strain rate tensor defined as $\mathbf{D}_p = 1/2(\mathbf{L}_p + \mathbf{L}_p^T)$ and $\mathbf{L}_p = \dot{\mathbf{F}}_p\mathbf{F}_p^{-1}$ the velocity gradient. $\mathbf{B}$ is the left Cauchy Green tensor (defined as $\mathbf{B} = \mathbf{F}\mathbf{F}^T$) associated to the global deformation and $\mathbf{B_e}$ is the left Cauchy Green tensor (defined as $\mathbf{B_e} = \mathbf{F_e}\mathbf{F_e}^T$) associated to the elastic deformation. According to the procedure described by Coleman and Noll [1963] for deformation processes, the incompressibility constraint and to Petiteau *et al.* [2012] who defined a Neo Hookean strain energy [Treloar, 1943] for each spring of the rheological model, it is deduced from Eq.(4.4) that the Cauchy stress can be described as:

$$\boldsymbol{\sigma} = -p\mathbf{I} + 2C_1\mathbf{B} + 2C_2\mathbf{B_e} \tag{4.5}$$

and the dissipation

$$2\mathbf{F}^T\frac{\partial \mathcal{W}_\mathbf{2}}{\partial \mathbf{B_e}}\mathbf{F_e} : \mathbf{D}_p \geq 0 \tag{4.6}$$

where C_1 the material parameter of the Neo Hookean model associated to the global deformation and C_2 is the material parameter of the Neo Hookean model of the elastic part. It is quickly recalled that a Neo Hookean model is defined as $W = C_1(I_1 - 3)$, where I_1 is the first strain invariant. It is deduced as in Petiteau *et al.* [2012] that for uniaxial extension in the direction $\vec{x}$ the first component of the stress tensor is:

$$\sigma = 2C_1\left(\lambda^2 - \frac{1}{\lambda}\right) + 2C_2\left({\lambda_e}^2 - \frac{1}{\lambda_e}\right) \tag{4.7}$$

where σ is the stress for a tensile test along the direction $\vec{x}$ and λ and λ_e the global and elastic stretches along the same direction. To determine the deformation of elastic and inelastic parts, i.e. the left Cauchy Green tensor of the elastic part, it is necessary to establish an evolution equation of $\mathbf{B_e}$, which is deduced as the simplest sufficient condition to satisfy Eq.(4.6). As described by Huber and Tsakmakis [2000] and Petiteau *et al.* [2012], the evolution equation is

$$\dot{\mathbf{B}}_\mathbf{e} = \mathbf{L}\mathbf{B_e} + \mathbf{B_e}\mathbf{L}^T - 4\frac{C_2}{\eta}\left({\mathbf{B_e}}^2 - \frac{1}{3}I_{1Be}\mathbf{B_e}\right) \tag{4.8}$$

where η is a material parameter. Particularly, in uniaxial extension the expression can be written by means of the stretch of the elastic part:

$$\dot{\lambda_e} = \lambda_e\frac{\dot{\lambda}}{\lambda} - 4\frac{C_2}{3\eta}(\lambda_e^3 - 1) \tag{4.9}$$

4.3.1.2 Convolution Integral Model

The CIM model is an adaptation of a K-BKZ formulation [Berstein *et al.*, 1963]. By using the same model as Petiteau *et al.* [2012] the stress endured by an incompressible material can be expressed as follow:

$$\sigma = -p(t)\mathbf{I} + 2g_0\mathbf{B}(t) - 2\mathbf{F}(t)\int_{-\infty}^{t} g_1 \exp\left(-\frac{t-\tau}{\tau_r}\right)\frac{\partial \mathbf{C}^{-1}(\tau)}{\partial \tau}d\tau\mathbf{F}^T(t) \tag{4.10}$$

where g_0, g_1 are material parameters that represent the stiffness of the material and are expressed in MPa and τ_r is a material parameter that represents a relaxation time in seconds. Adapted to uniaxial extension in direction $\vec{x}$, the model can be defined as:

$$\sigma = 2g_0\left(\lambda^2(t) - \frac{1}{\lambda(t)}\right) + \int_{-\infty}^{t} 2g_1 \exp\left(-\frac{t-\tau}{\tau_r}\right)\left[\frac{1}{\lambda(\tau)}\frac{\partial\lambda(t)}{\partial\tau}\left(2\frac{\lambda(t)^2}{\lambda(\tau)^2} + \frac{\lambda(t)}{\lambda(\tau)}\right)\right] d\tau \tag{4.11}$$

4.3.2 Homogenization by means of a micro spherical approach

4.3.2.1 General definition

The formulations previously presented (Eq.(4.22) and Eq.(4.10)) are isotropic. To turn it into a possible anisotropic formulation it is proposed to adapt the model with a sphere unit formulation, i.e. a spatial repartition of n directions, where each direction is defined by an initial vector $\mathbf{A}^{(i)}$ transformed in a vector $\mathbf{a}^{(i)}$ after deformation by $\mathbf{a}^{(i)} = \mathbf{F}\mathbf{A}^{(i)}$, where i is the number of the direction. It is often considered that each direction corresponds to a macromolecular chain and thus each chain can endure only tension-compression. To take into account the behavior of a material according to different directions, the fourth invariant $I_4^{(i)}$ is used. It is to note that the elongation and the fourth invariant are equivalent according to the definition:

$${I_4}^{(i)} = \mathbf{A}^{(i)}.\mathbf{C}\mathbf{A}^{(i)} = {\lambda^{(i)}}^2 \tag{4.12}$$

Where $\mathbf{C} = \mathbf{F}^T\mathbf{F}$ is the right Cauchy Green strain tensor. The following sections describe how to turn the models described previously into spherical models.

4.3.2.2 Application to the IVM

For IVM formulations, the location of the rotation in the decomposition between the elastic and the inelastic parts (cf. Eq.(4.22)) is still an open issue. Indeed it is often estimated that the rotation endured by the material occurs into the elastic part and not into the inelastic one. By means of this spherical formulation, the problem does not occur since each direction is only submitted to tension, that means that there is no hypothesis to formulate about the rotation in this approach. It is proposed to turn the IVM into a sphere unit formulation, thus each expression described previously has to be adapted. First, the evolution equation of the IVM is just adapted from Eq.(4.8) to be defined along n directions, it writes for each direction i:

$$\dot{\mathbf{B}}_\mathbf{e}^{(i)} = \mathbf{L}^{(i)}{\mathbf{B}_\mathbf{e}}^{(i)} + {\mathbf{B}_\mathbf{e}}^{(i)}{\mathbf{L}^T}^{(i)} - 4\frac{C_2}{\eta}\left({\mathbf{B}_\mathbf{e}}^{(i)^2} - \frac{1}{3}I_{1Be}{\mathbf{B}_\mathbf{e}}^{(i)}\right) \tag{4.13}$$

thus for uniaxial extension:

$$\dot{\lambda}_e^{(i)} = {\lambda_e}^{(i)}\frac{\dot{\lambda}^{(i)}}{\lambda^{(i)}} - 4\frac{C_2}{3\eta}\left({\lambda_e^{(i)}}^3 - 1\right) \tag{4.14}$$

by means of this expression one can obtain the value of the stress in each direction:

$$\sigma^{(i)} = 2C_1\left({\lambda^{(i)}}^2 - \frac{1}{\lambda^{(i)}}\right) + 2C_2\left({\lambda_e^{(i)}}^2 - \frac{1}{\lambda_e^{(i)}}\right) \tag{4.15}$$

4.3.2.3 Application to the CIM

To adapt the formulation of the CIM, the previous equation Eq.(4.11) must also be defined in n directions. Thus for the CIM, and due to the hypothesis of uniaxial extension the n directions can be described only by $\lambda^{(i)}(t)$. The stress for each direction can be deduced from the Eq.(4.11):

$$\begin{aligned}\sigma^{(i)} &= 2g_0\left({\lambda^{(i)}}^2(t) - \frac{1}{\lambda^{(i)}(t)}\right)\\ &+ \int_{-\infty}^{t} 2g_1 \exp\left(-\frac{t-\tau}{\tau_r}\right)\left[\frac{1}{\lambda^{(i)}(\tau)}\frac{\partial\lambda^{(i)}(t)}{\partial\tau}\left(2\frac{{\lambda^{(i)}}^2(t)}{{\lambda^{(i)}}^2(\tau)} + \frac{\lambda^{(i)}(t)}{\lambda^{(i)}(\tau)}\right)\right]d\tau\end{aligned}$$

4.3.2.4 Definition of the global stress

In this paper, it is proposed to use the spatial repartition of 42 directions proposed by Bazant and Oh [1986]. This discretization is homogeneously spread in space and allow to describe an isotropic behavior. The choice of 42 directions is made because they well represent the space and limit also the anisotropy due to the discretization as explained by Gillibert *et al.* [2010]. To obtain the total stress endured by the material, it is necessary to sum the influence of each direction by applying a weight $\omega^{(i)}$. Thus, the stress induced by the material for both models is defined as:

$$\boldsymbol{\sigma} = \sum_{i}^{42} \omega^{(i)}\sigma^{(i)}(\mathbf{a}_n^{(i)} \otimes \mathbf{a}_n^{(i)}) \tag{4.16}$$

where $\mathbf{a}_n^{(i)}$ is the normalized vector for each direction, i.e. $\mathbf{a}_n^{(i)} = \frac{\mathbf{a}^{(i)}}{\|\mathbf{a}^{(i)}\|}$ and $\sigma^{(i)}$ is given by Eq.(4.23) or Eq.(4.16) according to the chosen model. The spatial repartition of 42 directions used and proposed by Bazant and Oh [1986] is represented according to different plans in Fig.4.11. The Fig.4.11(a) represents the directions in the plan $(\vec{y}, \vec{z})$. It appears that each direction belong to a circle. A representation of the different circles is illustrated in the plan $(\vec{x}, \vec{z})$ in Fig.4.11(b).

4.3.2.5 Simulation of the homogenized models

It is proposed in this section to compare the results for a same loading for classical and spherical formulations and for both models at several strain rates. The Fig.4.12(a) highlights the results obtained for two cycles tensile tests up to $\lambda = 4$ along the direction $\vec{x}$ for the IVM classical formulation (as presented in Petiteau *et al.* [2012]) and Fig.4.12(b) the results with the spherical formulation for the IVM. For both simulations the parameters used are identical as those used by Petiteau *et al.* [2012]: $C_1 = 1$ MPa ; $C_2 = 9$ MPa and $\eta = 1$MPa.s. It is observed that the obtained behaviors are different for the two formulations, the results of the spherical formulation provide a lower response than the classical formulation for all the different strain rates studied. But the influence of the strain rate is similar for the two formulations. In the same way it is proposed to highlight the most requests directions for the spherical formulation. A weight stress tensor can be associated to each direction, i.e. $w^{(i)}\sigma^{(i)}(\mathbf{a}_n^{(i)} \otimes \mathbf{a}_n^{(i)})$, the contribution of the weight stress tensor along the tensile direction is illustrated in Fig.4.13 for a strain rate of $\alpha = 100$ s^{-1}. It is to note that each direction that belongs to a same circle (cf. Fig.4.11) presents the

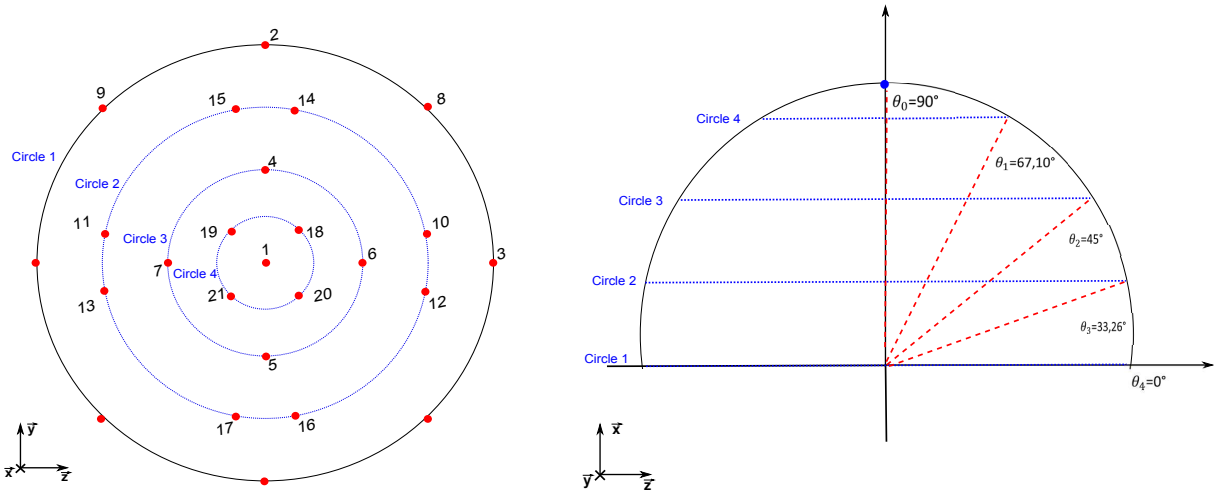

Figure 4.11: Representation of the 42 directions of Bazant and Oh [1986] (a) in the plan $(\vec{y},\vec{z})$, (b) and in the plan $(\vec{x},\vec{z})$.

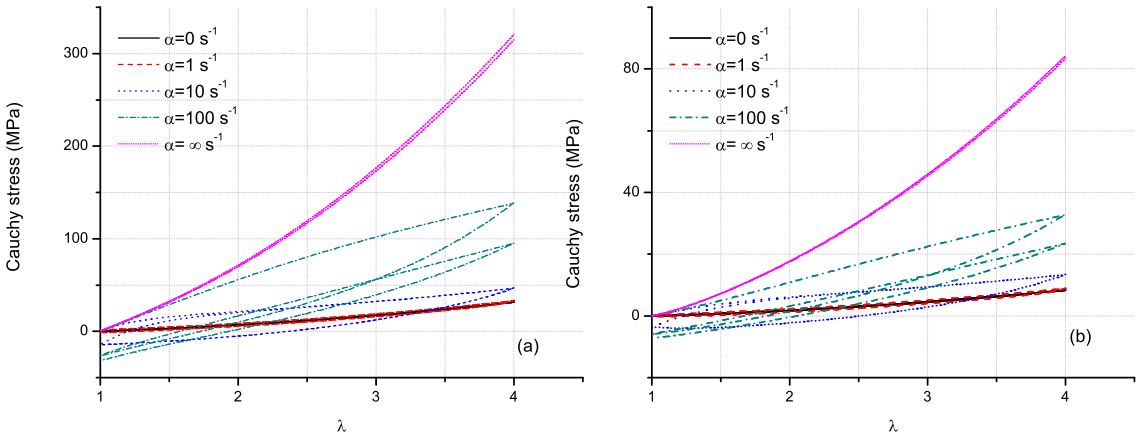

Figure 4.12: Stress strain curve IVM for an isotropic formulation (a) and a sphere unit formulation with 42 directions (b)

same mechanical behavior. Moreover, it is observed that some directions do not have any influence: directions 2-3-8-9 which belong to the circle 1 as illustrated in Fig.4.11. Indeed it is consistent that these directions do not present any influence since the directions of the circle 1 projected in the direction $\overrightarrow{x}$ (which matches to the tensile direction) is equal to zero. The other directions present an increasing contribution for the circles 2, 3, 4 and for the direction 1 which corresponds to the tensile direction.

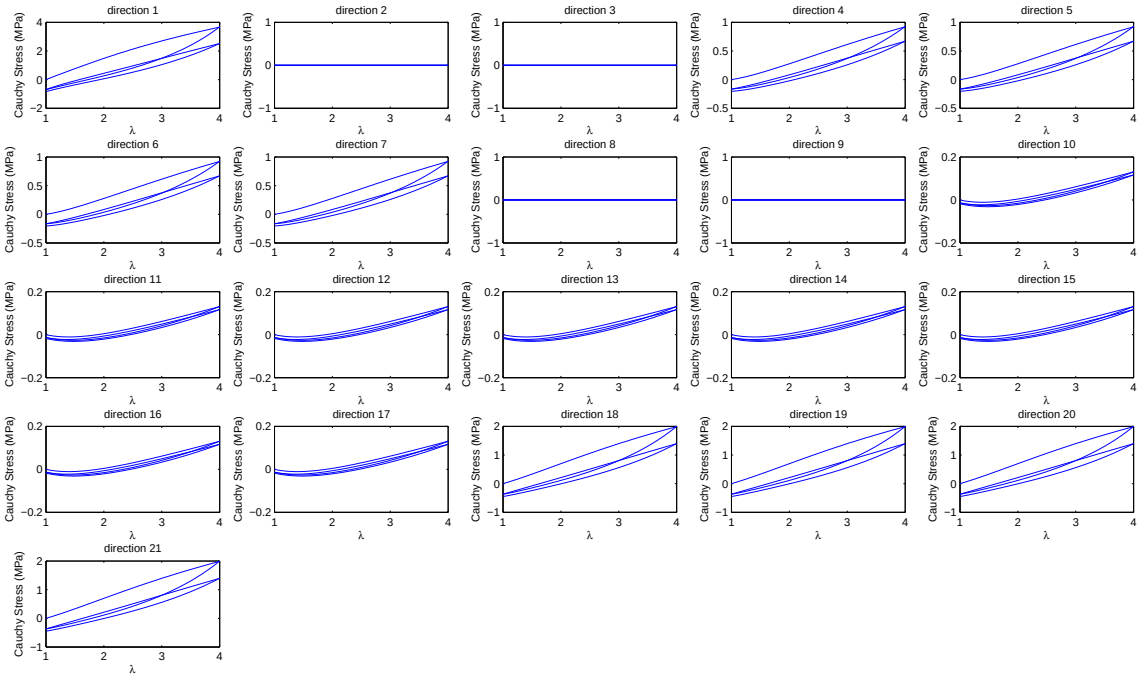

Figure 4.13: Stress strain curves for IVM for the 42 directions of the sphere unit model

It is proposed to realize the same two cycles tensile test up to $\lambda = 4$ with the classical and spherical formulations of the CIM. The obtained results are presented in Fig.4.14. The parameters used are identical as those used by Petiteau *et al.* [2012]: $g_0 = 1$ MPa, $g_1 = 9$ MPa and $\tau_r = \frac{1}{36}$ s. As previously, both formulations do not predict the same behavior, but the influence of the strain rate is similar. Indeed the spherical formulation induced a lower stress state than the classical formulation for the same strain state at different strain rates. The stress state for each direction can be observed in Fig.4.15 for a strain rate of $\alpha = 100$ s^{-1} and for the same mechanical parameter. As previously, the most request direction is the direction 1 since it is the direction that corresponds to the tensile direction $\overrightarrow{x}$.

4.3.2.6 Comparison of the two theories with a sphere unit formulation

As proved for the classical formulation by Petiteau *et al.* [2012], it appears that the two models exhibit the same response, even if the strengthening is larger for CIM than for IVM. Furthermore, the hysteresis loop is larger for IVM than for CIM. These differences are more important at high strain rates. With the sphere unit formulation it is observed that both models exhibit also similar responses, still with some differences, as illustrated in

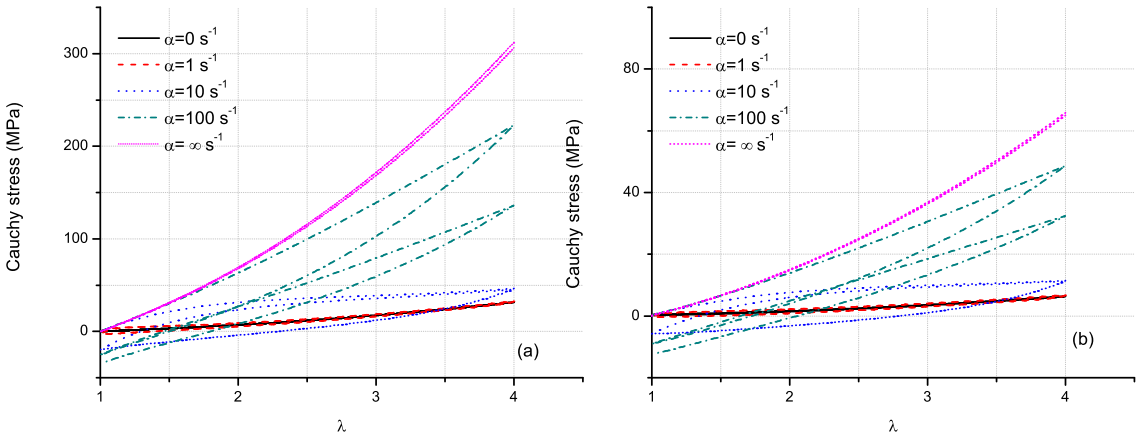

Figure 4.14: Stress strain curve of the CIM model for an isotropic formulation (a) and a sphere unit formulation with 42 directions (b)

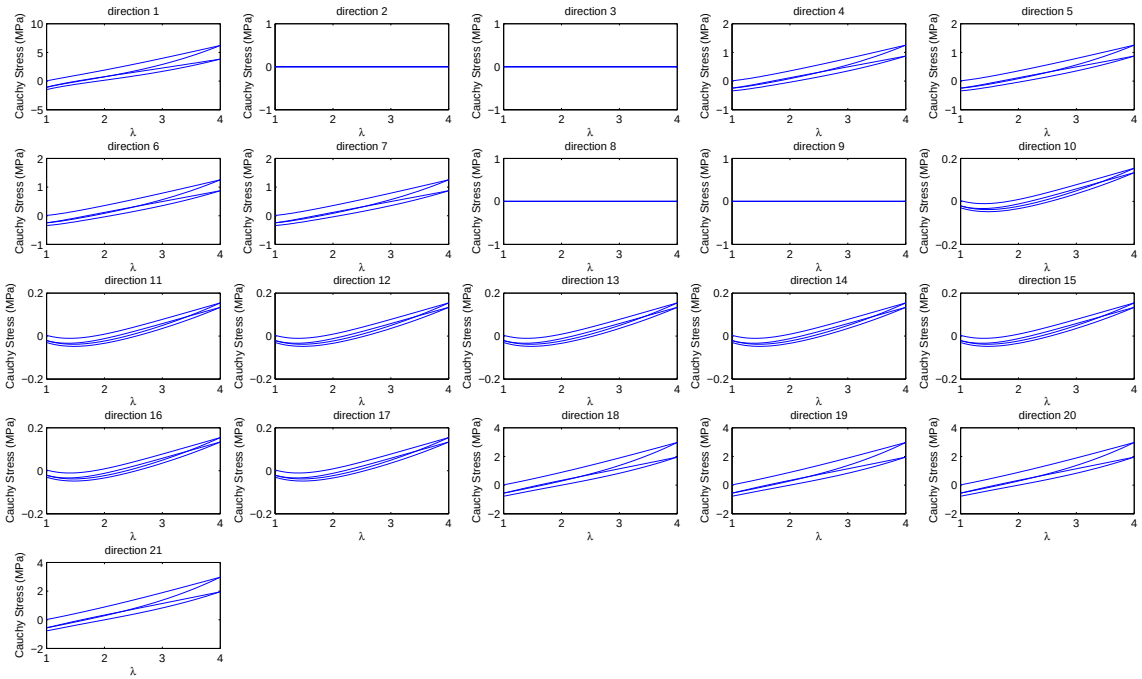

Figure 4.15: Stress strain curves for CIM for the 42 directions of the sphere unit model

Fig.4.12(b) and Fig.4.14(b). Indeed for all strain rates the two models present a different strengthening (larger for CIM than IVM) and hysteresis (larger for IVM than CIM). The differences are still more important for high strain rates. It is to note that the results of the sphere unit formulation are similar to the classical formulation for both models with a scale factor at each strain rates. This sphere unit formulation provides similar results as those of Miehe and Göktepe [2005]; Diani *et al.* [2006b] for isotropic materials. It is to note that the sphere unit formulation is based on a Neo Hookean constitutive equation but could be represented by any phenomenological constitutive equation instead of micro mechanics model based on Langevin function as proposed by Miehe and Göktepe [2005]; Diani *et al.* [2006b]. Anyway, the spherical formulation can be adapted to any strain energy density.

4.3.3 Comparison of the classical formulations and the sphere unit formulations for different mechanical loadings

In this part, it is proposed to compare the results obtained with a classical formulation and a spherical formulation for the IVM and the CIM according to different loadings states. For each formulation and model, it is proposed to simulate a two cycles test up to $\lambda = 4$ for uniaxial (UT), planar (PT) and equibiaxial (ET) tests. The stress equations for planar and equibiaxial tests are easily deduced from Eq.(4.22) and Eq.(4.8) for the IVM and from the Eq.(4.10) for the CIM. The Fig.4.16 illustrates the results obtained for the IVM and the CIM with the classical formulation. It is observed that the three mechanical tests provide approximately the same response, the first load and the beginning of the first unload. For the ET it is observed that the models cannot truly take into account the viscoelasticity since the tests present highly compressive stress during the unloading, these results are not consistent with the experimental observations. It is also expected to obtain a stress state more important for an equibiaxial test compare to uniaxial or planar state [Treloar, 1943; Marckmann and Verron, 2006; Boyce and Arruda, 2000]. This phenomenon can be explained by the unidirectional modeling used for the classical models.
The same cyclic tensile tests were performed with the sphere unit formulation for the IVM and CIM as illustrated in Fig.4.17. It appears that the equibiaxial tests provide a stress state more important than the uniaxial or planar tensile tests for a same strain state with the same elementary hyperelastic models. Furthermore with the sphere unit formulation, it is observed that there is only a few compressive stress during the unloading. These results are more consistent than those obtained with the classical formulation for the both models. These results highlight that the sphere unit formulation is more adapted to describe an equibiaxial test than the classical formulation for this type of viscoelastic models for classical formulations. The uniaxial and planar tensile tests are also well described by the sphere unit formulation.
In conclusion, these simulations prove that simple tensorial form models cannot be easily used to represent biaxial loading, and leads to inconsistent results. At the opposite the use of spherical approach to represent three dimensional loadings is efficient even if the three dimensional homogenization is based on simple tensorial form issue from uniaxial development.

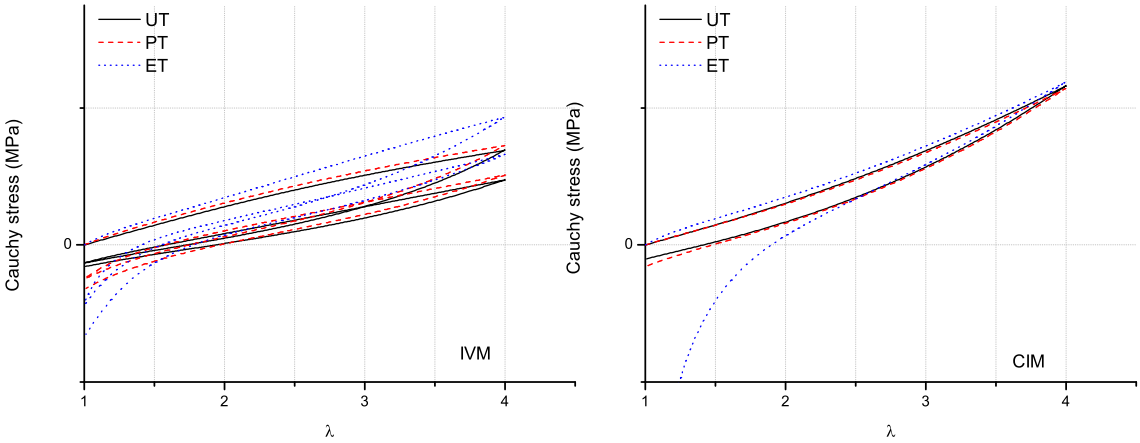

Figure 4.16: Stress-strain curves for uniaxial (UT), planar (PT) and equibiaxial (ET) tension for isotropic formulation with the IVM and the CIM

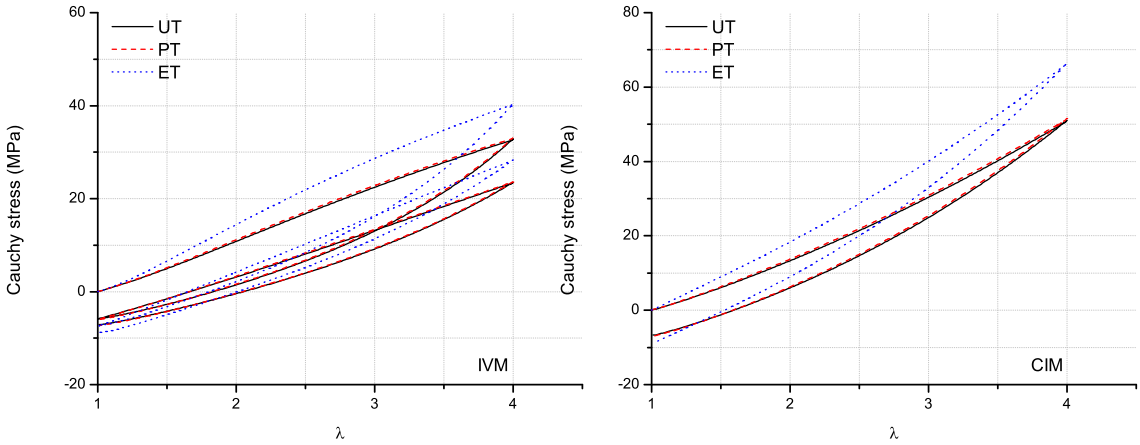

Figure 4.17: Stress-strain curves for uniaxial (UT), planar (PT) and equibiaxial (ET) tension for sphere unit formulation with the IVM and the CIM

4.3.4 Extension to anisotropic viscoelasticity

By means of the spatial repartition of the directions used previously, an isotropic viscoelastic formulation was written. It is proposed now to use the sphere unit formulation to obtain an anisotropic response by a parametric study of the different directions. That means that each direction is no longer represented by the same mechanical parameter. With the sphere unit formulation, the directions are homogeneously distributed in space, a projection of this distribution was presented in Fig.4.11. This homogenous repartition of the directions induces a quasi isotropic behavior [Gillibert *et al.*, 2010]. Thus, the results obtained for a tensile test along the direction $\vec{x}$ or $\vec{y}$ are identical.

4.3.4.1 Variation of the viscoelastic parameter (η and τ_r)

4.3.4.2 Presentation

It is proposed to induce a variation of the viscoelastic parameters η for the IVM and τ_r for the CIM. The variation of the viscoelastic terms do not change the expressions of the stress described previously. Except that, it is considered that this parameter depends on the considered directions as illustrated in Fig.4.18. To highlight the influence of an

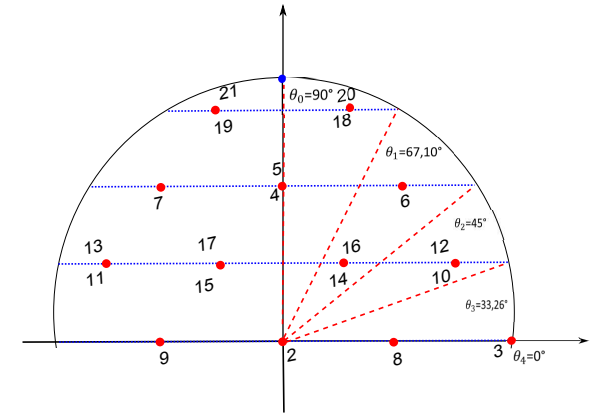

$$\eta = \eta_0 \cos(\theta_0) \qquad \tau_r = \tau_{r0} \cos(\theta_0)$$
$$\eta = \eta_0 \cos(\theta_1) \qquad \tau_r = \tau_{r0} \cos(\theta_1)$$
$$\eta = \eta_0 \cos(\theta_2) \qquad \tau_r = \tau_{r0} \cos(\theta_2)$$
$$\eta = \eta_0 \cos(\theta_3) \qquad \tau_r = \tau_{r0} \cos(\theta_3)$$
$$\eta = \eta_0 \cos(\theta_4) \qquad \tau_r = \tau_{r0} \cos(\theta_4)$$

Figure 4.18: Representation of the spatial distribution of Bazant and Oh directions in the plan $(\vec{y}, \vec{z})$

anisotropic formulation compared to an isotropic formulation, several numerical simulations are performed:

- First, a cyclic tensile test along the direction $\vec{x}$ until a stretch of $\lambda = 4$ is performed for a sphere unit formulation where the viscoelastic term is constant in each direction: $\eta(i) = 1$ MPa.s and $\tau_r(i) = \frac{1}{36}$ s $\forall i$, these tests are denoted (**dir1 – isotropic**).

- Then the same cyclic test along $\vec{x}$ is performed for a variation of the viscoelastic term for each direction as described previously and illustrated in Fig.4.18: $\eta(i) = \eta_0 \cos(\theta_i)$ and $\tau_r(i) = \tau_{r0} \cos(\theta_i)$ where $\eta_0 = 1$ MPa.s and $\tau_{r0} = \frac{1}{36}$ s, these tests are denoted (**dir1 – anisotropic**).

- Finally the same cyclic tensile test, with the variation of the viscoelastic parameters ($\eta(i) = \eta_0 \cos(\theta_i)$ and $\tau_r(i) = \tau_{r0} \cos(\theta_i)$), is performed along the direction $\vec{y}$, these tests are denoted (**dir2 – anisotropic**).

These simulations are performed for both models (IVM and CIM) and the same sets of mechanical parameters defined previously are used (cf. paragraph 4.3.2.5). All the results are simulated for a strain rate $\alpha = 100$ s^{-1}.

4.3.4.3 Analysis

The results of the tests described previously for the IVM and the CIM are presented in Fig.4.19. It is observed that the results are similar for the CIM (variation of τ_r), and for

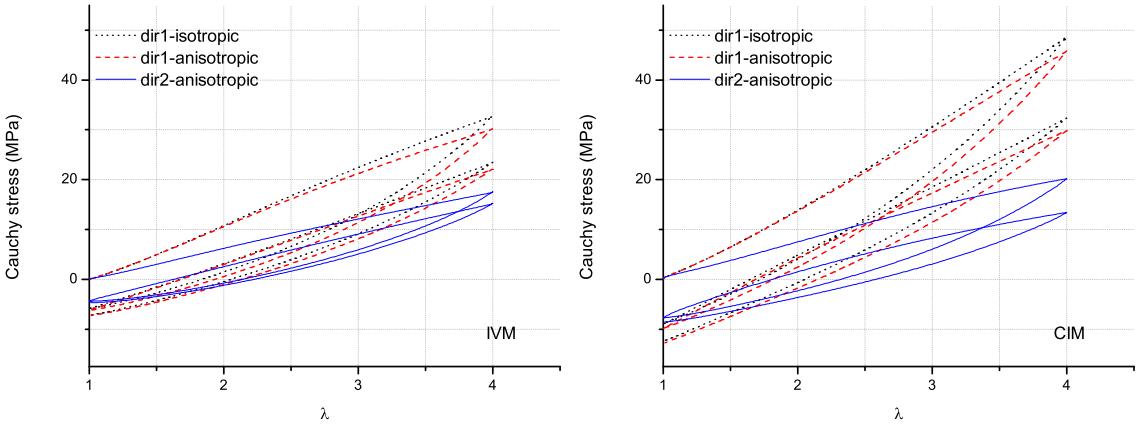

Figure 4.19: Variation of the viscoelastic parameter τ_r and η for the both model IVM and CIM, the other parameters are identical for a cyclic uniaxial tensile test.

the IVM (variation of η). Indeed the stress strain curves obtained for (**dir1 − isotropic**) and (**dir1 − anisotropic**) are very similar, the predominant direction in the spherical approach is the closest one from the loading direction. As the viscoelastic parameters were not changed in direction 1 the mechanical behavior is not so modified. At the opposite, the stress strain curve (**dir2 − anisotropic**) is very lower than the stress strain curves corresponding to a tensile test along the direction $\vec{x}$. Thus, it proves that with the spherical formulation the two models can easily represent a multidirectional anisotropic viscoelastic behavior.

4.3.4.4 Variation of the hyperelastic parameter of the inelastic part (g_1 and C_2)

4.3.4.5 Presentation

It is proposed for this second study to vary a second material parameter. The C_2 (IVM) or g_1 (CIM) parameters, are not the same in all directions. Thus, the variation of the parameters is expressed in the same way as previously, that means that C_2 and g_1 are now depending on the orientation of the directions in space as illustrated in Fig.4.20. As previously several tests are performed:

- First a tensile test along $\vec{x}$ until a stretch of $\lambda = 4$ for a constant value of the parameters in each direction: $C_2(i) = 9$ MPa and $g_1(i) = 9$ MPa $\forall i$, these tests are denoted (**dir1 − isotropic**).

- Then the same tensile test in the direction $\vec{x}$ with varying values of the parameters: $C_2 = C_{2-0}\cos(\theta_i)$ and $g_1 = g_{1-0}\cos(\theta_i)$ where $C_{2-0} = 9$ MPa and $g_{1-0} = 9$ MPa, these tests are denoted (**dir1 − anisotropic**).

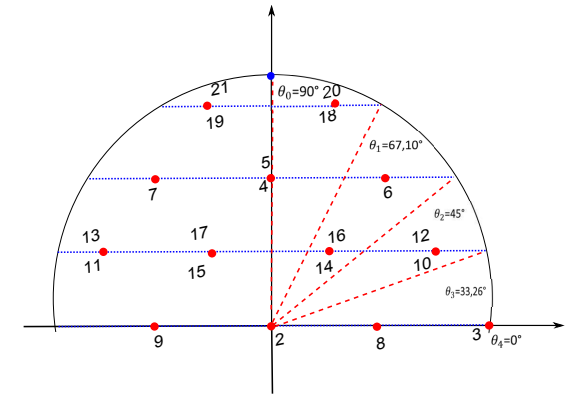

$$C_2 = C_{2-0}\cos(\theta_0) \qquad g_1 = g_{1-0}\cos(\theta_0)$$
$$C_2 = C_{2-0}\cos(\theta_1) \qquad g_1 = g_{1-0}\cos(\theta_1)$$
$$C_2 = C_{2-0}\cos(\theta_2) \qquad g_1 = g_{1-0}\cos(\theta_2)$$
$$C_2 = C_{2-0}\cos(\theta_3) \qquad g_1 = g_{1-0}\cos(\theta_3)$$
$$C_2 = C_{2-0}\cos(\theta_4) \qquad g_1 = g_{1-0}\cos(\theta_4)$$

IVM CIM

Figure 4.20: Representation of the spatial distribution of Bazant and Oh directions in the plan $(\vec{y}, \vec{z})$

- Finally, still the same tensile test along the direction $\vec{y}$ with also varying values (**dir2 – anisotropic**) is performed.

4.3.4.6 Analysis

The results can be observed in Fig.4.21, where g_1 and C_2 are varying and the other mechanical parameters are constant, the simulations are presented for a strain rate $\alpha = 100$ s^{-1}. As previously it is observed that for a tensile test along the direction $\vec{x}$ the results are quite similar for the both models, even if the anisotropic spherical formulation (**dir1 – anisotropic**) provides lower results as the isotropic spherical formulation (**dir1 – isotropic**). The tensile tests along the direction $\vec{y}$ for the anisotropic spherical

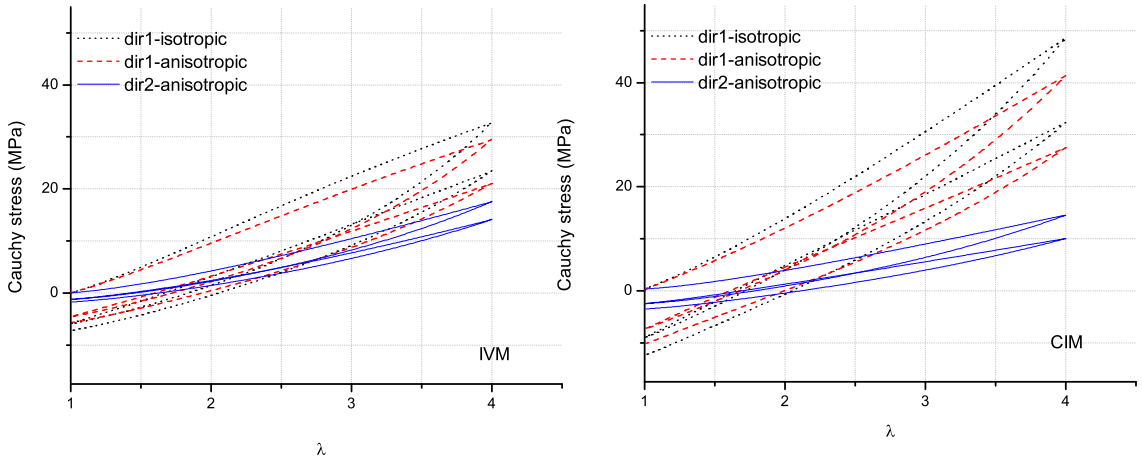

Figure 4.21: Variation of g_1 and C_2 for the both models IVM and CIM, the other parameters are still the same (where η and τ are constant) for a cyclic uniaxial tensile test.

formulation ($\mathbf{dir2-anisotropic}$) present results lower than the two other stress strain curves for both models. Thus, by varying these other mechanical parameters it is also possible to obtain an anisotropic behavior for both models, and the behavior of the chain oriented in the loading direction is still predominant.

4.3.4.7 Conclusions

According to this study, it was observed that, by means of a sphere unit formulation, it is easy to obtain an anisotropic behavior. The anisotropy of a material was induced by means of the mechanical parameters. All the parameters do not induce the same anisotropic response. Thus, it is possible to turn a material anisotropic as wished. The results presented in this paragraph where performed at $\alpha = 100\text{s}^{-1}$, but the conclusions are identical for other strain rates. Compared to others pre-existent models about viscoelasticity, it is to note that there is only a few proposed models in literature [Miehe and Göktepe, 2005; Diani *et al.*, 2006b] to take into account a multidirectional anisotropic viscoelastic behavior. Miehe and Göktepe [2005] proposed an adaptation of its initial model to take into account anisotropic behavior and Diani *et al.* [2006b] proposed a model to take into account the induced anisotropy due to the stress softening. Most of the anisotropic models are developed for soft tissues but they only present two different directions, due mainly to the fiber reinforcement in the material Peña *et al.* [2007]; Taylor *et al.* [2009]. The model presented here allows to take into account the initial anisotropy of a material by the simple way of a sphere unit formulation and can thus represented a multidirectional anisotropy by means of a simple phenomenological model.

4.3.5 Viscoelasticity and Mullins effect

As explained previously the viscoelasticity is one of the non linear phenomenon associated to rubberlike materials and soft tissues. Nevertheless other phenomena as Mullins effect or permanent set are also current for this materials. It is proposed in this part to add the phenomenological stress softening model developed by Rebouah *et al.* [2013] at the CIM and IVM to take into account the Mullins effect in the previous sphere unit viscoelastic models. It is to note that any other constitutive equation for describing the Mullins effect can also be used, especially the micromechanics-based model as De Tommasi *et al.* [2006]; Diani *et al.* [2006b]; Miehe and Göktepe [2005]. The main equations are recalled here where a repartition of n initial spatial directions $\mathbf{A}^{(i)}$ is also used. The general form of the strain energy is:

$$\mathcal{W} = \mathcal{W}_{cc}(I_1) + \sum_{i=1}^{n} \omega^{(i)} \mathcal{F}^{(i)} \mathcal{W}_{cf}^{(i)}(I_4^{(i)}). \tag{4.17}$$

where $\mathcal{W}_{cc}$ represents the hyperelastic Neo Hookean model already used in the viscoelastic model, and $\mathcal{F}^{(i)}$ is the Mullins effect evolution function similar as the one proposed by Zuñiga and Beatty [2002b] and $W_{cf}^{(i)}$ is the strain energy associated with each direction. The energy proposed by Kaliske [2000] is chosen:

$$\mathcal{W}_{cf}^{(i)} = \frac{K}{4}(I_4^{(i)} - 1)^2 \tag{4.18}$$

and the evolution function is:

$$\mathcal{F}^{(i)} = 1 - \eta_m \sqrt{\frac{I_{1\max} - I_1}{I_{1\max} - 3}} \left(\frac{I_{4\,\max}^{(i)} - I_4^{(i)}}{I_{4\,\max}^{(i)} - 1} \right) \left(\frac{I_{4\,\max}^{(i)}}{I_{4\,\max}} \right)^4 \tag{4.19}$$

where η_m is a mechanical parameter that represents the intensity of the stress softening between the first and the second loadings, and $I_{1\max}$, $I_{4\max}^{(i)}$ and $I_{4\max}$ are respectively the maximum values of I_1, ${I_4}^{(i)}$ for the direction i and ${I_4}^{(i)}$ for all directions.

4.3.5.1 IVM

The Mullins effect model was added to the viscoelastic part and thus the rheological scheme is modified as illustrated in Fig.4.22. The final expression of the IVM and Mullins

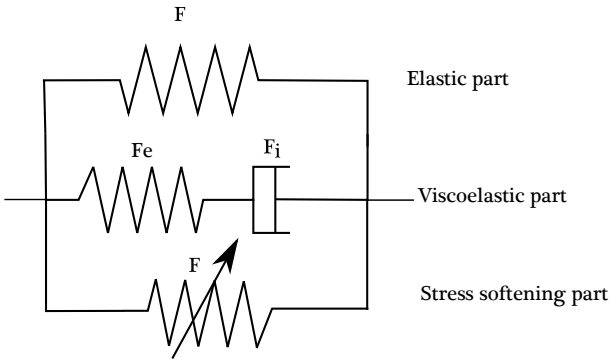

Figure 4.22: Representation of the viscoelastic and Mullins effect modeling

effect model is expressed as:

$$\sigma = \sum_{i}^{42} \omega^{(i)} \left(2C_1 \left({\lambda^{(i)}}^2 - \frac{1}{\lambda^{(i)}} \right) + 2C_2 \left({\lambda_e^{(i)}}^2 - \frac{1}{\lambda_e^{(i)}} \right) + 2{\lambda^{(i)}}^2 \mathcal{F}^{(i)} \frac{\partial W_{cf}}{\partial I_4^{(i)}}^{(i)} \right) \mathbf{a}_n^{(i)} \otimes \mathbf{a}_n^{(i)} \tag{4.20}$$

It is proposed to simulate a tensile test defined by 5 cycles until $\lambda = 2$, then 5 cycles until $\lambda = 3$ and finally 5 cycles until $\lambda = 4$. A strain rate of $\alpha = 15\ \mathrm{s}^{-1}$ is imposed and the chosen parameter are: $g_0 = 1$ MPa, $g_1 = 9$ MPa, η=1 MPa.s, K=0.5 MPa and η_m=4.5. The results are illustrated in Fig.4.23. The behavior of the viscoelastic part (**visco**) and stress softening (**Mullins**) are represented independently and finally the sum of these two behaviors is represented (**total**). It is observed that for each cycle the Mullins effect is well taken into account and can be very well treated independently of the viscous effects. The global behavior is finally composed of hyperelasticity, viscoelasticity and stress softening.

4.3.5.2 CIM

The Mullins effect part is added to the viscoelastic part of the CIM in the same way as described for the IVM. The evolution function, and the strain energy are the same. Thus, the following expression of the stress is obtained:

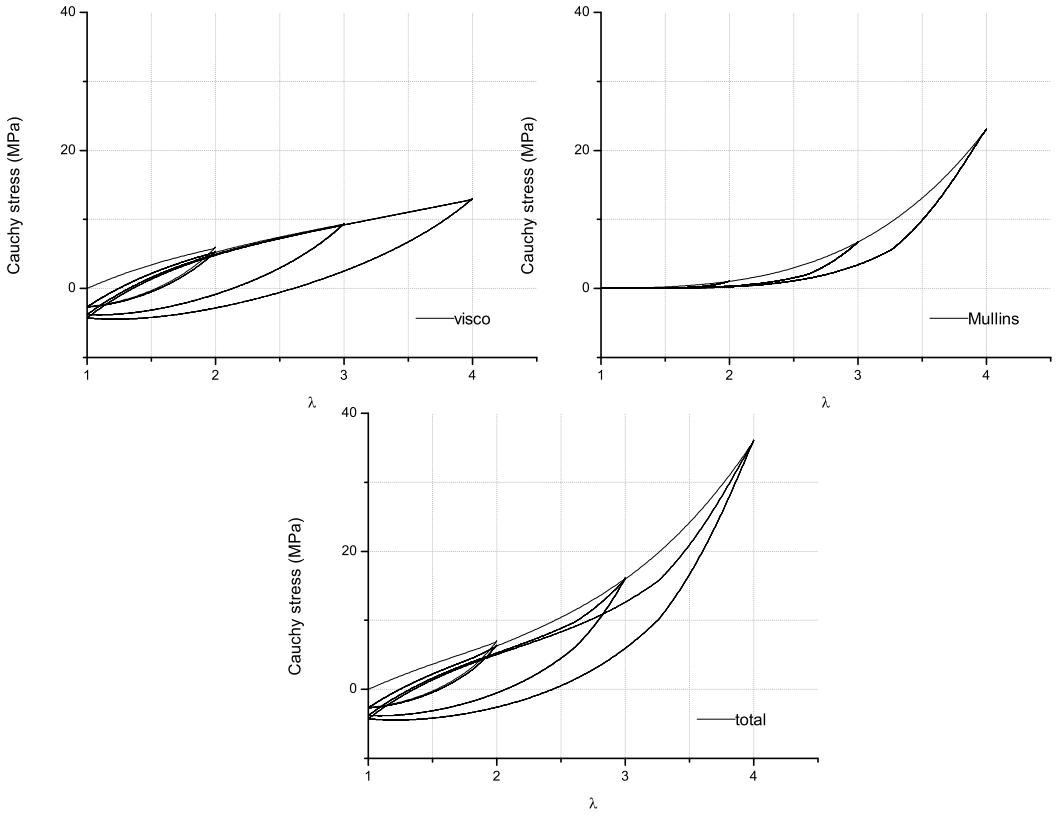

Figure 4.23: Simulation of 15 cycles with the IVM sphere unit model coupled with the Rebouah *et al.* [2013] stress softening model

$$\sigma = \sum_{i}^{42} \omega^{(i)} \left(\left[2g_0 \left({\lambda^{(i)}}^2(t) - \frac{1}{\lambda^{(i)}(t)} \right) \right] + \int_{-\infty}^{t} 2g_1 \exp\left(-\frac{t-\tau}{\tau_r} \right) \right.$$
$$\left. \left[\frac{1}{\lambda^{(i)}(\tau)} \frac{\partial \lambda^{(i)}(t)}{\partial \tau} \left(2\frac{{\lambda^{(i)}}^2(t)}{{\lambda^{(i)}}^2(\tau)} + \frac{\lambda^{(i)}(t)}{\lambda^{(i)}(\tau)} \right) \right] d\tau + 2{\lambda^{(i)}}^2 \mathcal{F}^{(i)} \frac{\partial W_{cf}}{\partial I_4^{(i)}}^{(i)} \right) \mathbf{a}_n^{(i)} \otimes \mathbf{a}_n^{(i)} \qquad (4.21)$$

It is also proposed to simulate the same test as the one described in paragraph 4.3.5.1. The results are obtained for a strain rate of $\alpha = 15$ s^{-1} and the material parameters are: $g_0 = 1$ MPa, $g_1 = 9$ MPa, $\tau_r = \frac{1}{36}$ s, K=0.5 MPa and η_m=4.5. The results are illustrated in Fig.4.24. As for the IVM it is observed that for cycles until a same strain state that the Mullins effect is well described and can be also very well treated independently as the viscous effects.

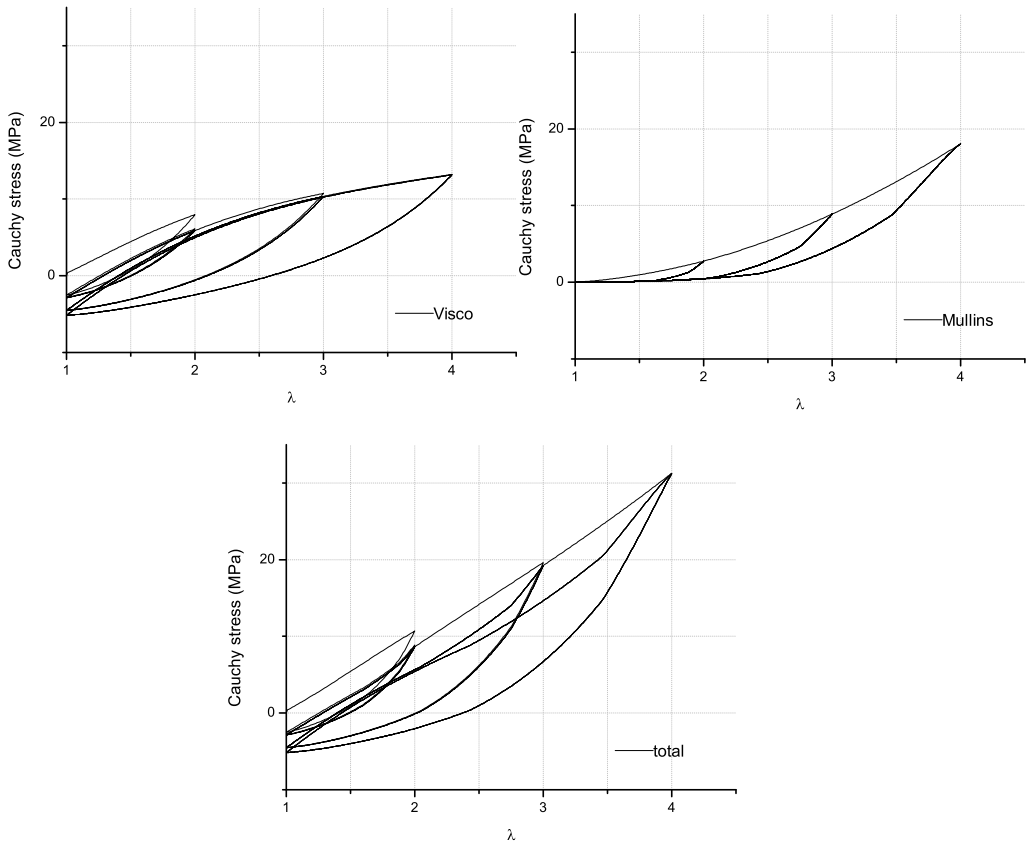

Figure 4.24: Simulation of 15 cycles with the CIM sphere unit model coupled with the Rebouah *et al.* [2013] stress softening model

4.3.6 Conclusion

This section presented an extension of Petiteau *et al.* [2012] study by proposing an adaptation of classical viscoelastic model to spherical approaches to realize a three directional homogenization in an incompressible framework. This formulation can be adapted to rubber like materials and soft tissues. Two classical models of viscoelasticity (IVM and CIM) were written by means of a spherical formulation and compared to a classical formulation. It appears that, if a homogeneous repartition of directions in space is used (isotropic behavior), the sphere unit model allows to describe better different loadings state (uniaxial, planar and equibiaxial tension) than a classical formulation by correctly describing the equibiaxial extension. This permits to use these simple constitutive equations in a tridimensional framework and to be able to simulate any loading state even with simple constitutive equations.

Then, the sphere unit formulation was used to induce an initial anisotropy by imposing different mechanical parameters in each direction. It was observed that an anisotropic behavior could be easily created in this way, simply by a parameter variation along the

directions. Finally, a stress softening model was added to the spherical formulation to also take into account the Mullins effect.

4.4 Extension to preexisting models

The point of this section is to propose models able to take into account the mechanical behavior of the studied NBR in first section. For this, and based on the previous part, several models are extended to a 3D homogenization by means of a micro spherical approach as described in the previous section. The first model studied is the model developed by Huber and Tsakmakis [2000] which is defined by a linear evolution equation, then three adaptations of the micro mechanical model proposed by Bergstrom and Boyce [1998, 2001] are used. The elastic part of the Bergstrom and Boyce [1998] model is either represented by a Neo Hookean [Treloar, 1943], a Mooney Rivlin [Mooney, 1940] or (as initially proposed) by the eight chain model [Arruda and Boyce, 1993]. Each model is built by considering that each direction endured tension compression loading. The following sections give the expression of the stress in one direction for each model.

4.4.1 The model of Huber and Tsakmakis [2000]-$Huber$

The first model used is the one proposed by Huber and Tsakmakis [2000] which was already described in the previous part of this chapter. The stress endured by each direction is described by the equations Eq.(4.22) and Eq.(4.23), that are recalled here:

$$\dot{\lambda}_e^{(i)} = {\lambda_e}^{(i)} \frac{\dot{\lambda}^{(i)}}{\lambda^{(i)}} - 4\frac{C_2}{3\eta}\left({\lambda_e^{(i)}}^3 - 1\right) \tag{4.22}$$

$$\sigma^{(i)} = 2C_1\left({\lambda^{(i)}}^2 - \frac{1}{\lambda^{(i)}}\right) + 2C_2\left({\lambda_e^{(i)}}^2 - \frac{1}{\lambda_e^{(i)}}\right) \tag{4.23}$$

This model is denoted as $Huber$ in the following.

4.4.2 The model of Bergstrom and Boyce [1998]-BB

In this paragraph, the classical equations of the Bergstrom and Boyce [1998, 2001] model are quickly recalled. The Bergstrom and Boyce [1998, 2001] model can be represented by an equilibrium part, denoted network A, and an overstress, denoted network B as represented in Fig.4.25. The network A represents the spring in parallel with the network B which is a represented by a spring and a dashpot in series. The Cauchy stress associated to the elastic part is a 8 chains model [Arruda and Boyce, 1993]. This model is one of the most used (see Dal and Kaliske [2009]; Rickaby and Scott [2013]; Kuhl *et al.* [2005] for instance).

$$\boldsymbol{\sigma}_A = \frac{\mu_A}{J\overline{\lambda}}\frac{\mathcal{L}^{-1}(\overline{\lambda}/\lambda_A^{lock})}{\mathcal{L}^{-1}(1/\lambda_A^{lock})}\mathrm{dev}\left[\overline{\mathbf{B}}\right] + \kappa\left[J-1\right]\mathbf{I} \tag{4.24}$$

Where μ_A and κ are material parameters, $J = det(\mathbf{F})$, $\overline{\mathbf{B}} = J^{-2/3}\mathbf{F}\mathbf{F}^T$, $\overline{\lambda} = \sqrt{tr[\overline{\mathbf{B}}]/3}$ and $\mathcal{L}^{-1}(x)$ is the inverse Langevin function, dev represents the deviatoric operator, λ_A^{lock}

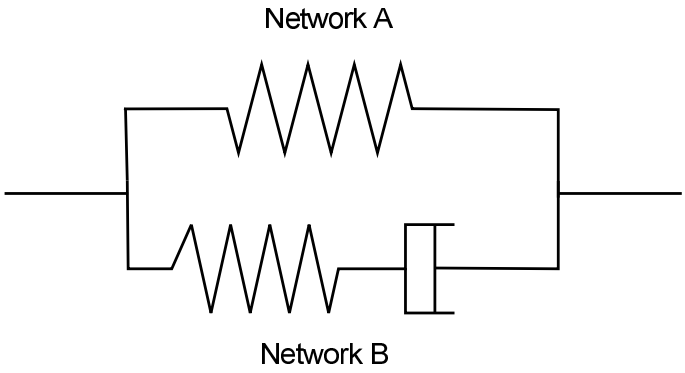

Figure 4.25: Representation of the two network for Bergstrom and Boyce [1998, 2001] model.

is a material parameter that represents the maximal elongation of the network A. In the same way the Cauchy stress of the network B can be expressed as:

$$\boldsymbol{\sigma}_B = \frac{\mu_B}{J_B^e \overline{\lambda_B^e}} \frac{\mathcal{L}^{-1}(\overline{\lambda_B^e}/\lambda_B^{lock})}{\mathcal{L}^{-1}(1/\lambda_B^{lock})} \text{dev}\left[\overline{\mathbf{B}_B^e}\right] + \kappa\left[J_B^e - 1\right]\mathbf{I} \tag{4.25}$$

Where μ_B and κ are material parameters, $J_B^e = det({\mathbf{F}_B}^e)$, $\overline{\mathbf{B}_B^e} = {J_B^e}^{-2/3}\mathbf{F}_B^e\mathbf{F}_B^{eT}$, $\overline{\lambda_B^e} = \sqrt{tr[\overline{\mathbf{B}_B^e}]/3}$ and λ_B^{lock} is a material parameter that represents the maximal elongation of the network B. The total Cauchy stress is defined by $\boldsymbol{\sigma} = \boldsymbol{\sigma}_A + \boldsymbol{\sigma}_B$. To determine the stress of the total network the total velocity is used $\mathbf{L}_B = \dot{\mathbf{F}}\mathbf{F}^{-1}$. The velocity can be decomposed into an elastic and an inelastic part, thus $\mathbf{L}_B = \mathbf{L}_B^e + \mathbf{F}_B^e\mathbf{L}_B^e\mathbf{F}_B^{e-1} = \mathbf{L}_B^e + \tilde{\mathbf{L}}_B^e$, furthermore we can defined $\mathbf{L}_B^p = \dot{\mathbf{F}_B^p}\mathbf{F}_B^{p-1} = \mathbf{D}_B^p + \mathbf{W}_B^p$ and $\tilde{\mathbf{L}_B^p} = \tilde{\mathbf{D}_B^p} + \tilde{\mathbf{W}_B^p}$. The unload configuration can be made unique by one particularly approach that takes the inelastic tensor equal to zero $\tilde{\mathbf{W}_B^p} = 0$. The viscous rate of change of the network B is defined by $\tilde{\mathbf{D}_B^p} = \dot{\gamma}_B\mathbf{N}_B$, where $\dot{\gamma}_B$ is an effective deformation rate and $\mathbf{N}_B$ gives the direction of the stress state. The effective strain rate is defined by

$$\dot{\gamma}_B = \dot{\gamma}_0(\overline{\lambda_B^p} - 1 + \epsilon)^C \left[\frac{\tau}{\tau_{base}}\right]^m \tag{4.26}$$

where $\dot{\gamma}_0$, C, τ_{base}, ϵ and m are material parameters, and τ is an effective stress. All the details are given in Bergstrom and Boyce [1998, 2001].

To determine the stress endured by each direction of the micro spherical approach, the same theory as previously is used. By means of the hypothesis of tension compression the stress endured by each direction can be deduced. Furthermore the material is considered as incompressible. The incompressibility is handled for each direction and not globally. It means that the hydrostatic pressure is taken into account for each direction. As the material is considered incompressible the second term of the equations Eq.(4.24) and Eq.(4.25) are useless. The expression of the stress for the network A becomes:

$$\boldsymbol{\sigma}_A^{(i)} = \frac{\mu_A}{\overline{\lambda^{(i)}}} \frac{\mathcal{L}^-1(\overline{\lambda^{(i)}}/\lambda_A^{lock})}{\mathcal{L}^-1(1/\lambda_A^{lock})} dev\left[\overline{\mathbf{B}^{(i)}}\right] \tag{4.27}$$

and for the network B:

$$\boldsymbol{\sigma}_B^{(i)} = \frac{\mu_B}{\overline{\lambda^{(i)}}} \frac{\mathcal{L}^-1(\overline{\lambda^{(i)}}/\lambda_B^{lock})}{\mathcal{L}^-1(1/\lambda_B^{lock})} dev\left[\overline{\mathbf{B}^{(i)}}\right] \tag{4.28}$$

Finally the total stress for each direction is defined as $\sigma^{(i)} = \sigma_A^{(i)} + \sigma_B^{(i)}$. Simple calculus permit to deduce the expression of the stress for each direction with the tension-compression hypothesis. This model is denoted as BB in the following.
It is important to note that the eight chain model is already equivalent to a 3D homogenization, from the micro mechanical point of view, there is no physical meaning to apply a micro spherical approach to an eight chain model. Nevertheless it is still proposed to observed the results that could be obtained for such new phenomenological model.

4.4.3 Bergstrom and Boyce [1998, 2001] with Neo Hookean-$BB - NH$

The third model used is also based on the Bergstrom and Boyce [1998, 2001] model. Indeed, the same equations are used to model the viscous effects but the two springs of the equivalent rheological scheme are not represented by an eight chain model but by a Neo Hookean strain energy. Thus, it can be deduced that the stress endured by each direction, in tension-compression is defined by:

$$\sigma^{(i)} = \sigma_A^{(i)} + \sigma_B^{(i)} = C_{1A}\left(I_{4A}^{(i)} - \frac{1}{\sqrt{I_{4A}^{(i)}}}\right) + C_{1B}\left(I_{4B}^{(i)} - \frac{1}{\sqrt{I_{4B}^{e(i)}}}\right) \tag{4.29}$$

Where $I_{4A}^{(i)}$ is equivalent to the square elongation of the elastic part of the reseau A and $I_{4A}^{e(i)}$ is equivalent elongation of the elastic part of the network B, and is determined by means of the evolution equation proposed by Bergstrom and Boyce [1998]. C_{1A} is the material parameter of the network A and C_{1B} is the material parameter of the network B. As previously the incompressibility is handled for each direction and not globally. This model is denoted as $BB - NH$ in the following.

4.4.4 Bergstrom and Boyce [1998, 2001] with Mooney Rivlin-$BB - MR$

The fourth model used is also based on the Bergstrom and Boyce [1998, 2001] model. As previously the viscous effects are taken into account by means of Bergstrom and Boyce [1998, 2001] equations, but the two spring of the equivalent rheological scheme are not represented by an eight chain model but by a Mooney Rivlin strain energy. The stress endured by each direction is defined by:

$$\begin{aligned}\sigma^{(i)} = {} & C_{1A}\left(I_{4A}^{(i)} - \frac{1}{\sqrt{I_{4A}^{(i)}}}\right) + C_{1B}\left(I_{4B}^{e(i)} - \frac{1}{\sqrt{I_{4B}^{e(i)}}}\right) \\ & + 2C_{2A}\left(I_{1A}^{(i)} I_{4A}^{(i)} - I_{4A}^{(i)2}\right) + 2C_{2B}\left(I_{1B}^{e(i)} I_{4B}^{e(i)} - I_{4B}^{e(i)2}\right)\end{aligned} \tag{4.30}$$

Where C_{1A} and C_{2A} are the material parameters of the network A and C_{1B} and C_{2B} are the material parameters of the network B. $I_{1A}^{(i)}$ is the first invariant for each direction of the network A and $I_{1B}^{e(i)}$ is the first invariant for each direction of the elastic part of the network B. It is recalled that the elongation depends on the fourth invariant ($I_4^{(i)} = {\lambda^{(i)}}^2$), thus first invariant can be expressed in function of the fourth as: $I_1^{(i)} = I_4^{(i)} + \frac{2}{\sqrt{I_4^{(i)}}}$. This model is denoted as $BB - MR$ in the following.

4.4.5 Definition of the global stress

For each one of the four models used, the stress endured by one direction is known. To deduce the global stress endured by the material the micro spherical approach is used and the equation defined previously Eq.(4.16) is used. Indeed for the Huber's model the equation presented in first section is used, for the Bergstrom and Boyce [1998, 2001] the Eq.(4.27) and Eq.(4.28) are injected in Eq.(4.16), for the mixed Bergstrom and Boyce [1998, 2001] with Neo Hooke the Eq.(4.29) is injected in Eq.(4.16), and finally for the mixed Bergstrom and Boyce [1998, 2001] with Mooney Rivlin the Eq.(4.30) is injected in Eq.(4.16). The equations obtained for the four models permit to take into account the hyperelastic and the viscoelastic behavior simultaneously, this part of the stress is denoted as $\boldsymbol{\sigma}_{viscoelastic}$.

4.4.6 Mullins effect

The viscoelasticity is not the only effect to take into account, as highlighted by the experimental data, the NBR used present also an important stress softening. The constitutive equations used previously to describe the Mullins effect are used as in Rebouah *et al.* [2013]. The Mullins effect strain energy $W_{cf}^{(i)}$ associated to each direction is:

$$\mathcal{W}_{cf}^{(i)} = \sqrt{\frac{I_4^{(i)} - 1}{I_4^{(i)}}} \tag{4.31}$$

the global strain energy is deduced by means of the micro spherical approach such as:

$$\mathcal{W} = \sum_{i=1}^{n} \omega^{(i)} \mathcal{F}^{(i)} \mathcal{W}_{cf}^{(i)}(I_4^{(i)}). \tag{4.32}$$

The evolution function $\mathcal{F}^{(i)}$ is similar as previously (cf. Eq.(4.19)). The stress part due to the Mullins effect is deduced from this equation (Eq.4.32) and is denoted as $\boldsymbol{\sigma}_{Mullins}$. For the four model described previously the stress due to the Mullins effect is added to the viscoelastic stress. Finally the total stress is a

$$\boldsymbol{\sigma} = \boldsymbol{\sigma}_{Mullins} + \boldsymbol{\sigma}_{viscoelastic} \tag{4.33}$$

4.4.7 Comparison with experimental data

In this last section, the models are compared to the experimental tests performed at a strain of $\alpha = 0.00025\text{s}^{-1}$ for the cyclic test with imposed relaxation times and the subloop tests. Only one strain rate is used since these modeling approaches are not adapted to the range of rates experimentally studied. The value of the material parameters of the models are given in the table 4.1 and the curve results are presented in Fig.4.26 and in Fig.4.27.

Table 4.1: Material parameters for the *Huber* model

Model	$C_1(MPa)$	$C_2(MPa)$	K (MPa)	$\eta(MPa.s)$	η_m
Huber	1.25	1	1	8000	7

Table 4.2: Material parameters for the BB models

Parameter	unit	BB-MR	BB-NH	BB
μ_a	(MPa)	0	0	2.4
μ_b	(MPa)	0	0	3
C_{1A}	(MPa)	0.75	1.5	0
C_{1B}	(MPa)	1.9	1.8	0
C_{2A}	(MPa)	1.8	0	0
C_{2B}	(MPa)	0	0	0
$\dot{\gamma_0}$	(s^{-1})	0.33	0.33	0.30
K	(MPa)	0.7	0.8	0.9
η_m	()	7	7	7
τ_b	(MPa)	1	1	1
m	()	10	10	8
c	()	-0.1	-0.1	-0.1
$\lambda_{lockA=B}$	()	0	0	2.9

4.4.7.1 Cyclic tests with imposed relaxation times

For the cyclic tests with imposed relaxation times, it appears that all the models described previously are able to take into account the non linear phenomena associated to the material (cf. Fig.4.26). Nevertheless, it also appears that some give a better estimation than other. For instance the $Huber's$ model does not allow an accurate description of the mechanical behavior, first because of the the hyperelastic behavior which is not well described and then because of the viscous effects. The linear evolution equation used do not permit to take into account well the viscous effects. But this model is very simple to use and could give good approximations in a first approach.
Then the mixed models $BB - NH$ and $BB - MR$ give similar results. The hyperelastic behavior is still not very well described but the viscous effects are much better taken into account. It appears that the hyperelastic behavior is not clearly improved by using a Mooney Rivlin model instead of a Neo Hookean. Indeed, for the viscoelastic part the use of the second term do not improve the predictive model at all. The material parameter (C_{2B}) is equal to zero and the model becomes equivalent to the Neo Hookean for the viscoelastic part. The hysteretic loop is well described as long as the deformations reached are not too important. After 50% of global deformation and due to the stress hardening of the material, the hysteretic behavior is not as well described. The low capacity of the model for large deformation are due first to the stress hardening of the material which is not well described and then to the relaxation time imposed during the test. When the material reached its maximal global deformation $\lambda = 2.5$, the unloading starts immediately, no relaxation time is imposed. However, the non linear evolution equation of the viscoelastic part proposed by Bergstrom and Boyce [1998, 2001] improve well the description of the material compared to the $Huber$ model.
Finally the BB model is the one that allows the best description of the mechanical behavior of the material. Nevertheless the micro mechanic based model submitted to a micro

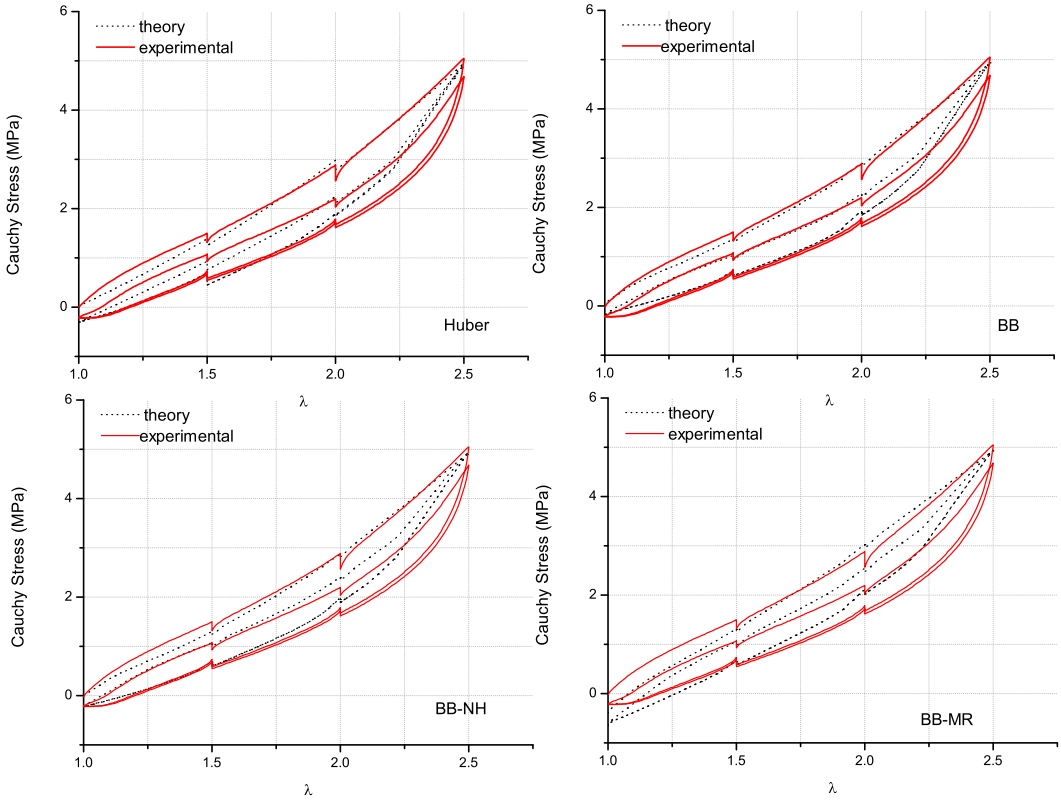

Figure 4.26: Comparison with experimental data of cyclic tensile test with imposed relaxation times at a strain rate $\alpha = 0.00025\text{s}^{-1}$.

spherical approach does not have any physical meaning. In this study, it can be only considered as a phenomenological model.
The Mullins effect is well described for the test and for all the models studied. The rupture of slope is important at the unloading of the largest deformation ($\lambda = 2.5$) because the material present an important stress softening and the evolution equation decreases too fast. It could be improved by using another evolution function associated to the stress softening nevertheless a function that decreases faster than the one proposed will probably not verify the second principle and will not be polyconvex.

4.4.7.2 Subloop tests

The subloop tests, represented in Fig.4.27, are most complex and difficult proposals. Indeed the models are not able to take into account this typical loading. The intern subloops cannot be described with the same mechanical parameters as those used to describe the major loop. Even if, for all the models, the material parameter are identical as those used for the relaxations tests, it does not allowed to take into account this complex loading.

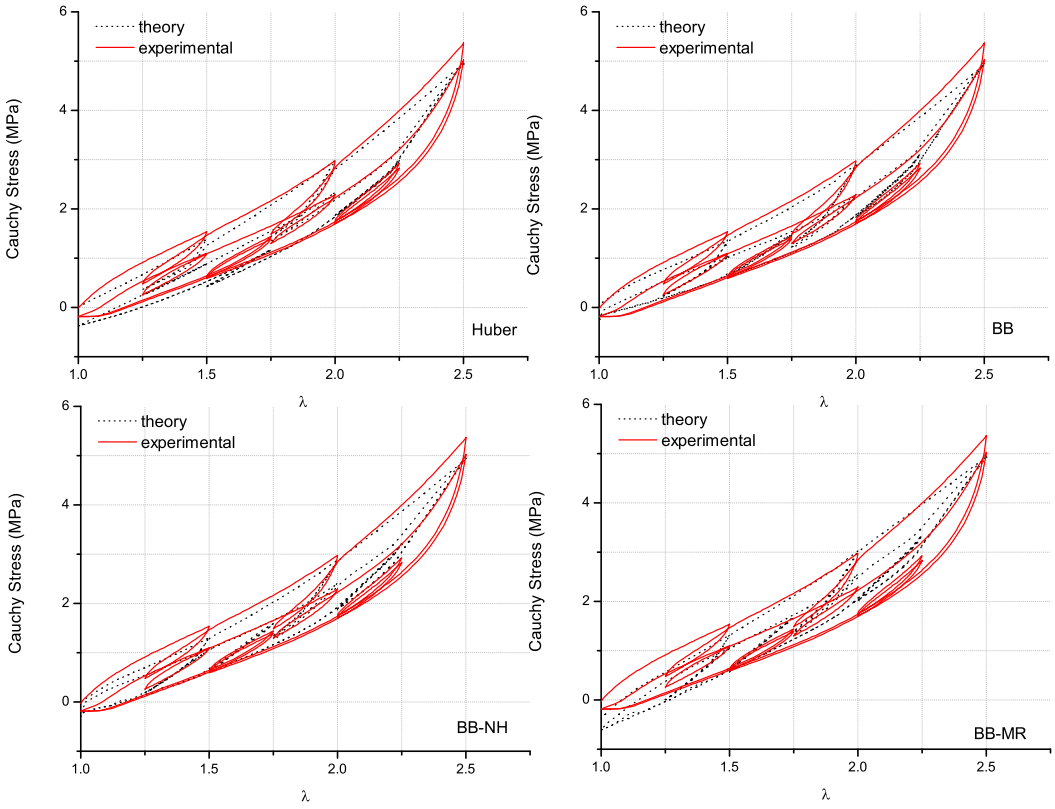

Figure 4.27: Comparison with experimental data of cyclic tensile test with intern subloops at a strain rate $\alpha = 0.00025\text{s}^{-1}$.

The micro spherical approach does not allow an improvement for this typical loading. To take well into account this test, a modeling where the hysteresis is considered as permanent and strain rate independent should be more efficient as proposed by Rey *et al.* [2014]. As for the previous test studied, it is observed that the Mullins effect is well described. The rupture of slope observed is still due to the model used at the large deformation.

4.4.8 Discussion

In this chapter, several modeling choices were made. First, the tension compression hypothesis in each direction of the micro sphere was done. Due to this hypothesis a stress equation was imposed in each direction instead of a strain energy. This non common method influences the predictive model. The mechanical behavior is influenced by using a stress or a strain energy, even if they can be derived one compared to the other in 3D. Then the incompressibility is not handled globally but locally. Indeed for the viscoelastic part, it is handled for each direction. As each direction is considered as incompressible the sum of them is too. The incompressibility of the Mullins effect is by contrast handled

globally.

4.5 General conclusion

This chapter was divided in three major parts, first the experimental part focused on the study of a NBR. Several tests lead on this material exhibit its highly non linear mechanical behavior: stress softening, permanent set, hysteresis, time dependent behavior.

Then a theoretical part focused mainly on the adaption of two classical models already existent into a micro spherical approach. It appears that the use of a micro spherical approach to take into account viscous effects is efficient. The global behavior stays unchanged but by means of this approach an anisotropic mechanical behavior can be modeled. Furthermore it appears that complex loading can be model. This approach permits an improvement of classical and simple models.

Based on the two first parts, the third part presented a comparaison of the experimental data with several viscoelastic models turned into a micro spherical approach. For this, the Huber and Tsakmakis [2000] model and three extended models issue from Bergstrom and Boyce [1998, 2001] are used. It appears that their capacity can be increased by a sphere unit approach, especially for complex loading. Nevertheless it is still very difficult to build a model able to take into account all the non linear phenomena at different strain rates for complex loadings as the cyclic tensile tests with intern subloops.

Chapter

5 Architectured materials

Some part of this chapter have been submitted and can be found in the following reference

- **M. Rebouah, G. Chagnon, D. Favier**, 2014, Development and modeling of filled silicone architectured membranes, Meccanica, submitted

Contents

5.1 General introduction

By means of the rubber like materials, it is possible to create materials with different atypical mechanical behavior as explained in Chapter 1. These new materials are called architectured materials. Their main advantage is to locally modify the material microstructure or structure and to control the mechanical behavior. The objective of this chapter is to induce and control initial anisotropy of an architectured material, while the bulk material is initially isotropic. As presented in the first chapter there are two types of architectured materials. First, some that can be considered as architectured due to their

geometric structure, and secondly, materials considered as architectured due to their microstructure. In this way, this chapter is divided in two main parts. A first section that presents a geometrical architectured material by means of a crenelated membrane made of Room Temperature Vulcanization 3428 (RTV3428) filled silicone. And a second section that presents micro-structural architectured membranes by means of two fabrication processes on two different materials: a RTV3428 and a Thermo Plastic Elastomer (TPE). Both sections present experimental data performed on the different samples and a modeling is proposed for each material. In first section only the Mullins effect is took into account, a numerical implementation is proposed too. In the second section the viscous effects of the materials are added to the modeling, but the proposed constitutive equation is not implemented into a Finite Element code.

5.2 Geometrical architectured membrane

This first section presents a geometrical architectured membrane. It can be separated in three parts, the core of the membrane (the central part) and the upper and lower lattices of crenels that are on the external surfaces of the core of the membrane. Crenelated membranes were already studied by Meunier [2011] with an unfilled silicone rubber which was perfectly hyperelastic but suffered from bad properties in tearing which makes it difficult to use in real applications. In this study, it is chosen to develop the same crenelated membranes, with a filled silicone rubber to improve the resistance of the material. Due to the fillers, the material presents good tearing properties although it shows other phenomena like stress softening or hysteresis as presented in Chapter 1. The aim of this part is to study the mechanical behavior of such architectured membranes when they are stretched in their plans and to develop the associated constitutive equation. A method to develop an equivalent model of the core of the membrane and of the crenels is presented. The membrane properties come from the bulk material, *i.e.* the filled material. Its main properties are to support reversible large deformations and to endure stress softening that induces anisotropy as presented in Chapter 2. First, the experimental set up and the architectured membranes are described. Several tests are performed to highlight the mechanical behavior. Then, a theoretical study presents the constitutive equation developed to build the strain energy of the architectured membranes. Finally, the constitutive equations are implemented into a Finite Element (FE) code. A comparison between the FE simulation and a complex experimental test is proposed. Short conclusions on geometrical architectured materials are presented.

5.2.1 Materials and methods

The same filled silicone rubber (RTV3428) is used to manufacture all the architectured membranes presented in the paper. This material was already used in previous works and some non linear phenomena as hysteresis, relaxation [Machado *et al.*, 2010; Rey *et al.*, 2013] and induced anisotropy [Machado *et al.*, 2012b] were already studied. As illustrated by Rey *et al.* [2013], the Mullins effect is the prevailing phenomenon so the experimental results focus on the study of this phenomenon. The other phenomena are not considered in a first approach.

5.2.1.1 Description of the architectured membrane

The architectured membranes are manufactured according to the process described by Meunier [2011], by injection molding to obtain circular architectured plane membranes. For that purpose, a specific mold was used. The mold is composed of two circular crenellated metallic plates of 16 cm diameter, each one of these plates comes lock another holey metallic plate on each side. When the holey plate is locked, there is a space of 1 mm between the two crenellated plates. Besides, the two crenellated plates can be fixed separately in any wished angular position. Thus, any circular architectured membrane with different crenels orientations can be molded. Once the injection is done, the mold filled out of silicone is put at 70 °C for 4 hours into an oven to accelerate the vulcanization. Finally, flat membranes ascribed of geometrical motifs (lattices of parallel crenels) on the upper and lower external surfaces are obtained. Due to the geometry of the architectured membranes, several coordinate systems have to be defined and are presented in Fig.5.1. Two coordinate systems are defined for the two crenels layers. For the first crenel the basis denoted $R_1(\boldsymbol{E}_1, \boldsymbol{K}_1, \boldsymbol{z})$ is defined and for the second crenel the basis denoted $R_2(\boldsymbol{K}_2, \boldsymbol{E}_2, \boldsymbol{z})$. The vector $\boldsymbol{E}_i$ corresponds to the crenel direction, $\boldsymbol{K}_i$ is an orthogonal vector in the plan of the membrane, and $\boldsymbol{z}$ is orthogonal to the plan $(\boldsymbol{x}, \boldsymbol{y})$ of the membrane. It is to note that the architectured membranes are characterized by the angle δ between the two lattices of the crenels, thus δ is the angle defined by the orientation $\boldsymbol{E}_1$ and $\boldsymbol{E}_2$. Finally, a global coordinate system is introduced $R(\boldsymbol{x}, \boldsymbol{y}, \boldsymbol{z})$. The vector $\boldsymbol{y}$ matches the bisector of the orientations of the crenels and $\boldsymbol{x}$ is an orthogonal vector in the plan of the membrane. For the following the model is defined in the basis R of the architectured membrane.

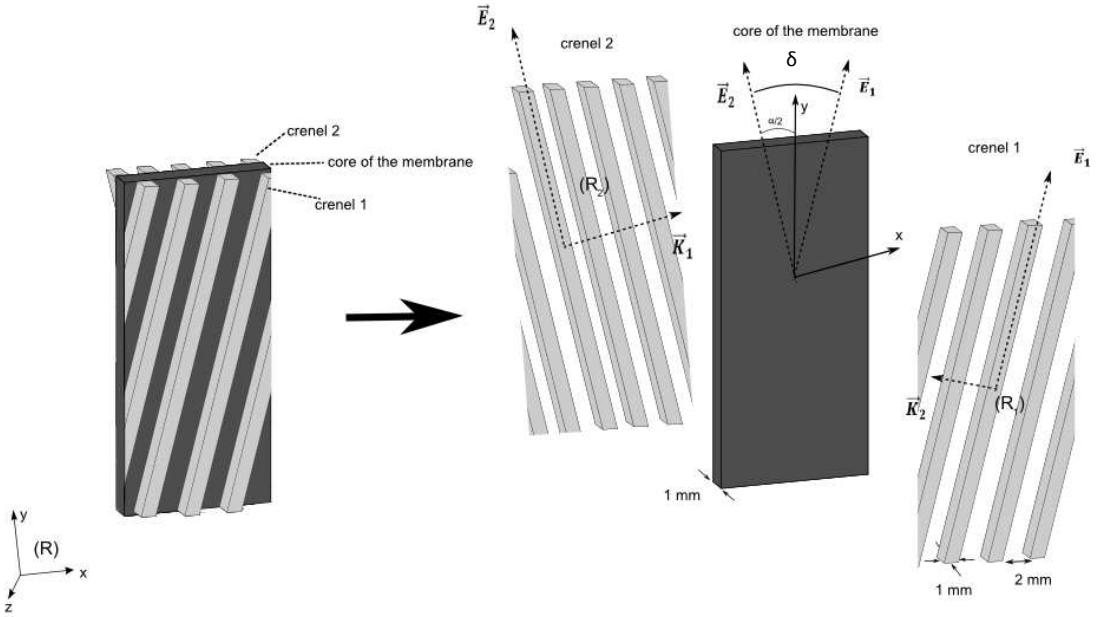

Figure 5.1: Geometry of the architectured membrane, on the left the specimen is presented, on the right the specimen is presented in a cut version to highlight the three layers

In order to study the influence of the crenel orientations, five different circular architectured membranes were molded with the same material and same processing. For each architectured membrane, the only parameter that changes is the relative orientation δ between the crenels, the geometry of the crenels stays the same. Finally, architectured membranes with $\delta = 0°, 45°, 90°, 135°$ and $180°$ are manufactured. Tensile rectangular specimens were cut from the circular plate samples along the direction $\boldsymbol{y}$ (as illustrated in Fig.5.1) *i.e.* along the bisector of the crenels orientations. The initial dimensions of the tensile samples are L=60 mm long, l=21 mm width and e=1 mm thick for the core of the membrane. The crenels on the external surfaces of the membrane are spaced out of 2 mm and the width and thickness of each crenels are 1 mm (cf. Fig.5.1).

5.2.1.2 Experimental set up

For each architectured tensile test sample, a cyclic tensile test along the vector $\boldsymbol{y}$ (corresponding to the bisector of the crenels orientations) was processed. By means of tension device, the samples underwent a cyclic tensile test up at three different elongations λ, where λ represents the current length of the sample over its initial length. The first loading unloading cycle is reached at $\lambda = 1.5$, the second at $\lambda = 2.$, and the third at $\lambda = 2.5$. After these three cycles a reloading at $\lambda = 2.5$ is performed. The measurements are made by means of a 100 N load cell which is synchronized to a Stereo-Dimensional Image Correlation (SDIC) system. This technique enables to determine the 3D contour and the in-plane strain fields of the object surface. Then the strain fields of the architectured membrane can be studied at any point of the surfaces. The specimens present a periodic structure which has to be repeat at least seven times in the width of the specimen to consider a continuum model. Due to the crenel orientations, the section of the specimens is different for each membrane. Thus, it is proposed to analyze the results using the nominal tension T to have a more realistic comparison for all the samples. The nominal tension is defined as:

$$T = \frac{F}{l_0} \tag{5.1}$$

where F is the applied force and l_0 the initial width.

5.2.1.3 Experimental results

The results of the tensile tests are presented in the Fig.5.2 for the five different orientations of crenels. Fig.5.2(a) presents the evolution of the transversal elongation λ_x during the tensile test in the REV, which was measured by means of SDIC, in function of the tensile elongation, *i.e.* λ_y. The solid line represents the theoretical transversal elongation for a tensile test on an incompressible isotropic material and the dashed lines represent the experimental transversal elongation for the membranes with different orientations δ. For an orientation of $\delta = 0°$, the transversal elongation matches perfectly the mechanical behavior of incompressible isotropic material, *i.e.* $\lambda_x = \frac{1}{\sqrt{\lambda_y}}$. For orientations of $\delta = 45°$ and $\delta = 90°$ the curves are overlapping and present a behavior very close to the theoretical behavior of an incompressible isotropic material but with little lower transversal elongations. At the opposite, for $\delta = 135°$ and $180°$, the transversal elongations are largely different from the incompressible isotropic material. Fig.5.2(b) illustrates the evolution

of the nominal tension in function of the tensile elongation. It is observed that the orientation δ between the crenels strongly influences the tension in the membrane. The lower orientation requires the higher tension to deform the architectured membrane. It is to note that few differences are observed for $\delta = 135°$ and $\delta = 180°$. The same results were observed by Meunier [2011] with an unfilled silicone rubber. Nevertheless, compared to Meunier [2011], the bulk material presents phenomena as hysteresis and Mullins effect that can also be observed for the crenelated membranes. As for the bulk material, it appears that the Mullins effect is important and that in comparison the hysteresis is weaker.

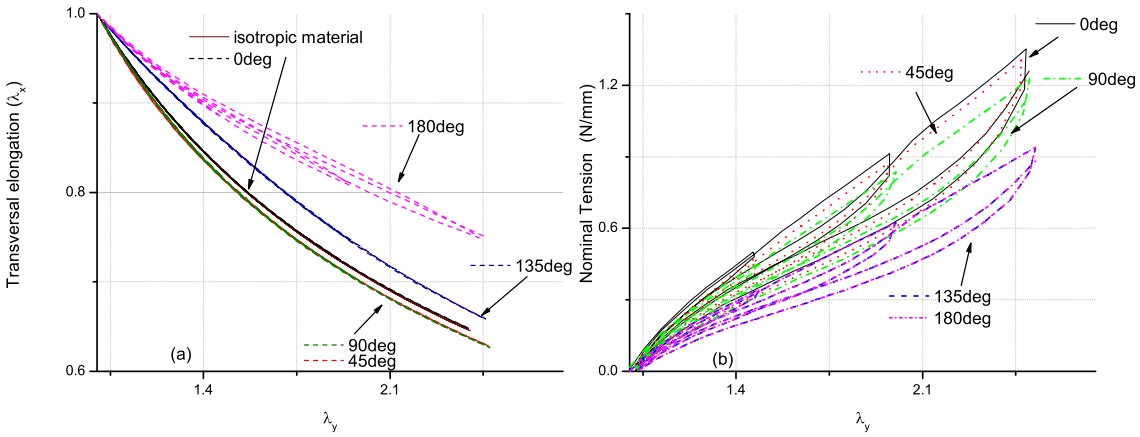

Figure 5.2: Evolution of the transversal elongation (a) and nominal tension (b) of the architectured membrane for different crenel orientations $\delta = 0°, 45°, 90°, 135°$ and $180°$

5.2.2 Architectured filled silicone membrane constitutive equation

5.2.2.1 General form

Rubber like materials are described by means of a strain energy density $\mathcal{W}$. It is proposed to decompose the strain energy function as the sum of the strain energies of the core of the membrane $\mathcal{W}_{\text{core-membrane}}$ and of each crenel $\mathcal{W}_{\text{crenel-1}}$, $\mathcal{W}_{\text{crenel-2}}$ as:

$$\mathcal{W} = \mathcal{W}_{\text{core-membrane}} + \mathcal{W}_{\text{crenel-1}} + \mathcal{W}_{\text{crenel-2}} + \mathcal{W}_{\text{coupling}} \tag{5.2}$$

Another term $\mathcal{W}_{\text{coupling}}$ is added in order to represent the strain energy density of coupling between the crenels and the membrane. The strain energy densities should take into account the observed phenomena during experimental tests. It is proposed in a first approach to develop a constitutive equation taking into account only the hyperelasticity and the stress softening of the architectured membrane.

5.2.2.2 Constitutive equation of the bulk material filled silicone rubber

The filled silicone rubber used in this study presents an induced anisotropy [Machado *et al.*, 2010, 2012b]. Rebouah *et al.* [2013] developed a constitutive equation written with strain invariants to predict the behavior of this material. The strain energy density $\mathcal{W}_{\text{silicone}}$ is additively decomposed into two parts: one that represents the strain energy of the chains

linked to other chains $\mathcal{W}_{cc}$ and another part that represents the strain energy of the chains linked to filler $\mathcal{W}_{cf}$, the total strain energy density is $\mathcal{W}_{\text{silicone}} = \mathcal{W}_{cc} + \mathcal{W}_{cf}$. Rebouah *et al.* [2013] considered that Mullins effect is mainly due to the presence of fillers. Thus, only W_{cf} is evolving with the stress softening. W_{cf} is represented by a microsphere model that can record the deformation history of the material. The 42 spatial initial directions $\mathbf{A}^{(i)}$ proposed by Bazant and Oh [1986] are used. The dilatation in each direction are defined by means of ${I_4}^{(i)}=\mathbf{A}^{(i)}.\mathbf{C}\mathbf{A}^{(i)}$ where $\mathbf{C}$ is the right Cauchy Green strain tensor, defined as $\mathbf{F}\mathbf{F}^T$, where $\mathbf{F}$ is the deformation gradient. The $\mathbf{A}^{(i)}$ directions are transformed in $\mathbf{a}^{(i)}$ after a deformation by $\mathbf{a}^{(i)} = \mathbf{F}\mathbf{A}^{(i)}$. Finally, the general form of the strain energy in an incompressible framework is:

$$\mathcal{W}_{\text{silicone}} = \mathcal{W}_{cc}(I_1, I_2) + \sum_{i=1}^{42} \omega^{(i)} \mathcal{F}^{(i)} \mathcal{W}_{cf}^{(i)}(I_4^{(i)}). \tag{5.3}$$

where I_1, I_2 are the first and second strain invariants of the tensor $\mathbf{C}$, $\omega^{(i)}$ represents the weight of each direction, $\mathcal{F}^{(i)}$ is the Mullins effect evolution function. The Mooney [1940] strain energy is chosen for W_{cc} and the strain energy of each chain $W_{cf}^{(i)}$ is defined as:

$$\mathcal{W}_{cf}^{(i)} = \frac{K}{2} \ln I_4^{(i)} (I_4^{(i)} - 1) \tag{5.4}$$

where K is a material parameter. The form was modified compared to Rebouah *et al.* [2013], as the bundle of RTV3428 material used in this paper presents less stress hardening. The same evolution function as proposed by Rebouah *et al.* [2013] is used:

$$\mathcal{F}^{(i)} = 1 - \eta \sqrt{\frac{I_{1\max} - I_1}{I_{1\max} - 3}} \left(\frac{I_{4\,\max}^{(i)} - I_4^{(i)}}{I_{4\,\max}^{(i)} - 1} \right) \left(\frac{I_{4\,\max}^{(i)}}{I_{4\,\max}} \right)^4 \tag{5.5}$$

where η is a material parameter, $I_{1\max}$, ${I_4}_{\max}^{(i)}$ and $I_{4\max}$ are respectively the maximum values of I_1, ${I_4}^{(i)}$ for direction i and ${I_4}^{(i)}$ for all directions $i = 1...42$. The evolution function cannot be negative since it is considered that each chain can only endure tension and no compression. The Cauchy stress tensor is then the sum of two terms:

$$\boldsymbol{\sigma}_{\text{silicone}} = \boldsymbol{\sigma}_{cc} + \boldsymbol{\sigma}_{cf} \tag{5.6}$$

$\boldsymbol{\sigma}_{cc}$ is the part of the Cauchy stress that represents the chains linked to other chains and $\boldsymbol{\sigma}_{cf}$ the part of the Cauchy stress that represents the chains linked to fillers. Finally the stress is written as:

$$\begin{aligned} \boldsymbol{\sigma}_{\text{silicone}} = -p\mathbf{I} + 2\mathbf{B}\frac{\partial W_{cc}}{\partial I_1} + 2\left(I_1\mathbf{B} - \mathbf{B}^2\right)\frac{\partial W_{cc}}{\partial I_2} + \\ 2\sum_{i=1}^{42} \omega^{(i)} \mathcal{F}^{(i)} \frac{\partial W_{cf}}{\partial I_4^{(i)}}^{(i)} \mathbf{F}(\mathbf{A}^{(i)} \otimes \mathbf{A}^{(i)})\mathbf{F}^T \end{aligned} \tag{5.7}$$

5.2.2.3 Strain energy of the core of the membrane

The core of the membrane is the central part of the architectured membrane and can be described as the bulk material. Thus, this part of the structure is simply represented by the constitutive equation given by Eq.5.7. The model is fitted on the bulk material.

Fig.5.3 presents a comparison between the simulation of the model and a tensile cyclic test performed on the filled silicone rubber. The model parameters are: $C_1 = 0.065$ MPa, $C_2 = 0.045$ MPa, $\eta = 9$, $K = 0.27$ MPa. The first load is well described. Some little errors are observed for the second loads but the fit is quite good.

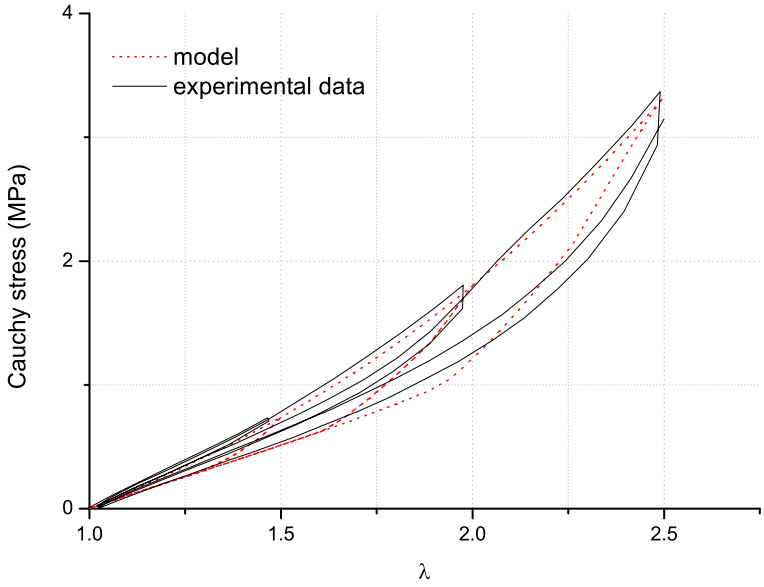

Figure 5.3: Comparison of the model and experimental data for the bulk material

5.2.2.4 Strain energy of the crenels

The crenels are processed with the same material as the core of the membrane, so the mechanical characteristics are the same. During the deformation of the membrane, it is considered that crenels are only submitted to tension-compression loading. It is estimated that there is no flexion in the crenels so they are modeled as bars. To determine the stress of each crenel, it is proposed to write the Eq.(5.7) in term of unidirectional components to represent the uniaxial extension undergone by the crenels. That means that $\boldsymbol{\sigma}_{cf}$ should be described only according to the elongation in the direction $\mathbf{E}_k$, where k represents either the crenel 1 or the crenel 2. Thus, the behavior of each crenel can be modeled only by means of the fourth invariant $I_{4c}^{(k)}$ corresponding to the direction $\mathbf{E}_k$, $I_{4c}^{(k)}$ is defined as

$$I_{4c}^{(k)} = \mathbf{E}_k.\boldsymbol{C}\mathbf{E}_k \tag{5.8}$$

λ_{E_k} represents the elongation in the direction $\mathbf{E}_k$. Thus the strain energy of each crenel depends only on the fourth invariant:

$$\mathcal{W}_{\text{crenel-k}} = \mathcal{W}(I_{4c}^{(k)}) \tag{5.9}$$

The loading state in the crenel can be expressed by the right Cauchy-Green strain tensor

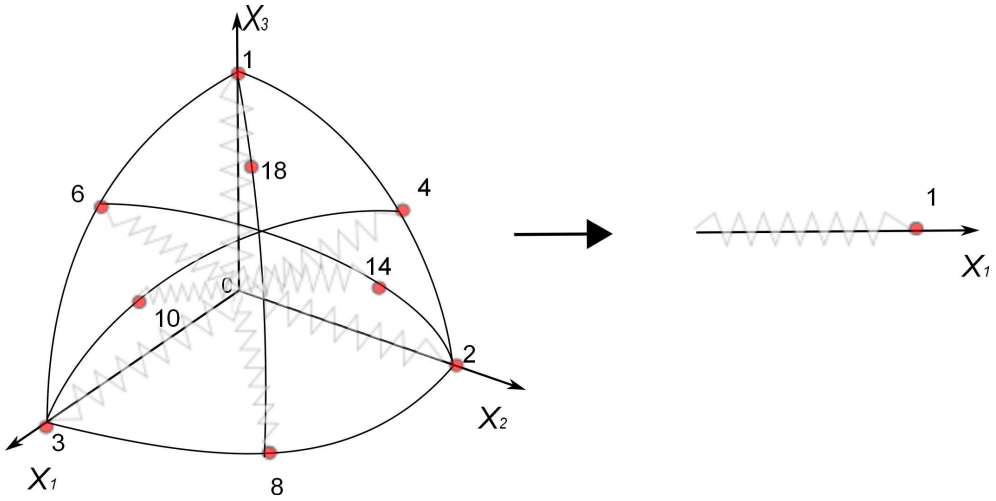

Figure 5.4: Representation of a eighth of the 42 directions of Bazant and Oh; replacement of these directions by only one direction for tensile test adapted to one direction for the crenel

$\mathbf{C_c}^{(k)}$ written in the basis R_k as:

$$\mathbf{C}_c^{(k)} = \begin{pmatrix} \lambda_{\mathbf{E}_k}^2 & 0 & 0 \\ 0 & \frac{1}{\lambda_{\mathbf{E}_k}} & 0 \\ 0 & 0 & \frac{1}{\lambda_{\mathbf{E}_k}} \end{pmatrix}_{R_k} \tag{5.10}$$

As a consequence, the first and second invariants can be expressed in function of ${I_{4c}}^{(k)}$:

$$I_{c1}^{(k)} = I_{4c}^{(k)} + \frac{2}{\sqrt{I_{4c}^{(k)}}} \tag{5.11}$$

$$I_{c2}^{(k)} = \frac{1}{2}\left((I_{c1}^{(k)})^2 - \left((I_{4c}^{(k)})^2 + \frac{2}{{I_{4c}}^{(k)}}\right)\right) \tag{5.12}$$

The term $\boldsymbol{\sigma}_{cf}$ in Eq.(5.7) should be modified in order to be expressed only by means of ${I_{4c}}^{(k)}$. The objective is to replace the 42 directions by 1 with a new weight $\omega_c^{(i)}$ as illustrated in Fig.5.4. First, it is necessary to focus on the first loading curve where the evolution functions $\mathcal{F}^{(i)}$ do not evolve and stay equal to 1. To evaluate the new value of $\omega_c^{(i)}$ noted $\tilde{\omega}$ in the direction $\mathbf{E}_k$ a comparison of the stress $\boldsymbol{\sigma}_{cf}$ with 42 directions

$$\boldsymbol{\sigma}_{\text{cf}} = 2\sum_{i=1}^{42} \omega_c^{(i)} \mathcal{F}^{(i)} \frac{\partial W_{cf}}{\partial I_4} \mathbf{F}\mathbf{A}^{(i)} \otimes \mathbf{A}^{(i)}\mathbf{F}^T. \tag{5.13}$$

and with only the E_k direction is done.

$$\boldsymbol{\sigma}_{\text{cf-crenel}} = 2\tilde{\omega}\mathcal{F}_c^{(k)} \frac{\partial W_{cfc}}{\partial I_{4c}^{(k)}} \mathbf{F}\mathbf{E}_k \otimes \mathbf{E}_k\mathbf{F}^T \tag{5.14}$$

This comparison allows to deduce the value of the weight for one direction. A value of $\tilde{\omega} = 0,21$ is obtained for the first loading curves to coincide as illustrated in Fig.5.5. The

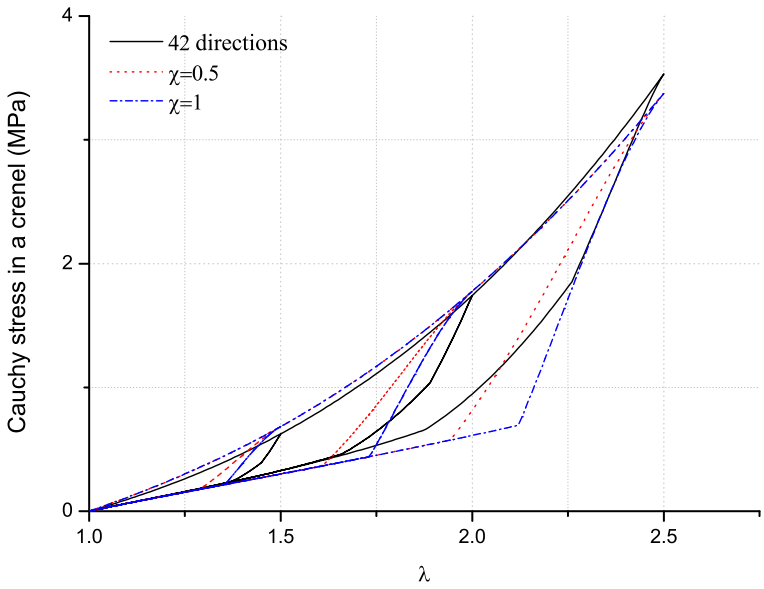

Figure 5.5: Cauchy stress for the directional part of the Cauchy stress with 1 direction for $\tilde{\omega} = 0.21$ and $\chi = 0.5$ or $\chi = 1$, and with 42 directions

parameter used for the representation is $K = 1.07$ MPa but the value of $\tilde{\omega}$ is independent of K. In Eq.(5.14) W_{cfc} is the strain energy for only one direction, *i.e.* for a crenel, which is identical as the strain energy of the core of the membrane given in Eq.(5.4).
For the second loading curves, the evolution function $\mathcal{F}^{(i)}$ must be considered. It was described as the product of three terms (cf Eq.(5.5)). The third term of the product is useless since with only one direction $I_{4\,\max}^{(k)} = I_{4\,\max}$, there is no influence of the other directions on the considered one. In tension, the first invariant can be expressed by means of the fourth invariant (cf. Eq.(5.11)), that means that I_{1c} and I_{4c} are no longer independent variables. Thus the evolution function can only be expressed by way of $I_{4c}^{(k)}$ or $I_{1c}^{(k)}$. It is chosen to express it in function of $I_{4c}^{(k)}$. The evolution function is adapted as:

$$\mathcal{F}_c^{(k)} = 1 - \eta\chi \left(\frac{I_{4c\,\max}^{(k)} - I_{4c}^{(k)}}{I_{4c\,\max}^{(k)} - 1} \right)^2 \tag{5.15}$$

A new parameter χ is introduced to represent the transformation of 42 directions to 1. Fig.5.5 highlights the role of the intensity χ of the crenels evolution function for a value of $K = 1.07$ MPa and $\eta = 9$. χ has an important role in the form of the second loading curve. It must be a value of 0.5 to limit important slope discontinuities and to represent a behavior closer to the microsphere formulation. As for $\tilde{\omega}$, the determination of χ is independent of the value of the material parameter K and η. Thus, the strain energy of the crenel is defined as:

$$\mathcal{W}_{\text{crenel-k}} = \mathcal{W}_{cc}(I_{4_c}^{(k)}) + \tilde{\omega}\mathcal{F}_c^{(k)}\mathcal{W}_{cf}(I_{4_c}^{(k)}) \tag{5.16}$$

Finally, the contribution of the crenel in the membrane stress is defined as:

$$\boldsymbol{\sigma}_{crenel(k)} = \left(2C_1 \left(I_{4c}^{(k)} - \frac{1}{\sqrt{I_{4c}^{(k)}}} \right) + 2C_2 \left(\sqrt{I_{4c}^{(k)}} - \frac{1}{I_{4c}^{(k)}} \right) + 2\tilde{\omega}\mathcal{F}\frac{\partial W_{cf}}{\partial I_{4c}^{(k)}} \right) \mathbf{e}_n^{(k)} \otimes \mathbf{e}_n^{(k)} \quad (5.17)$$

where $\mathbf{e}_n^{(k)}$ represents the normed instantaneous direction of the crenels such as $\mathbf{e}^{(k)} = \mathbf{F}\mathbf{E}_k$ and $\mathbf{e}_n^{(k)} = \mathbf{e}^{(k)} / \left\| \mathbf{e}^{(k)} \right\|$. To determine the tension, a parameter β must be introduced to quantify the proportion of crenels. In fact the crenels have the same height as the core of the membrane but also recover a third of the surface of the membrane (see section 2), that means that $\beta = \frac{1}{3}$.

5.2.2.5 Coupling strain energy

It is proposed to develop this term to take into account the coupling effect between the crenels and the core of the membrane. The coupling strain energy term has to take into account the shear induced by the crenels on the external faces of the core of the membrane, *i.e.* along the two directions $\boldsymbol{E}_1$ and $\boldsymbol{E}_2$. The coupling term can be taken into account in different ways. Reese *et al.* [2001] developed a strain energy coupling between orthotropic directions composed by the product of terms isotropic (*i.e.* I_1) and anisotropic (here $I_{4c}^{(1)}$ and $I_{4c}^{(2)}$). Natali *et al.* [2009], Göktepe *et al.* [2010] and Nerurkar *et al.* [2011] defined also a constitutive equations by using two other invariants that take into account the shear in the material to model living tissues as heart or annulus fibrosus of the intervertebral disc. In each case, it is proposed to develop a coupling term by using the eighth and ninth invariants. This approach is considered here:

$$\mathcal{W}_{coupling} = \mathcal{W}(I_8, I_9) \quad (5.18)$$

By adaptation of invariants developed by Spencer [1971], we used:

$$I_8 = \frac{1}{2} \left(\mathbf{C} : (\mathbf{E}_1 \otimes \mathbf{E}_2) + \mathbf{C} : (\mathbf{E}_2 \otimes \mathbf{E}_1) \right) \quad (5.19)$$

$$I_9 = \mathbf{E}_1 . \mathbf{E}_2 \quad (5.20)$$

Finally a new strain energy density is proposed:

$$\mathcal{W}_{coupling} = C_8(\delta) \int \ln(1 + \mathrm{abs}\,|I_8 - I_9|)\, dI_8 \quad (5.21)$$

where $C_8(\delta)$ represents a material parameter which depends on the orientation δ between the crenels to be adapted to every membrane. It represents the torsion stiffness of the core of the membrane according to the initial orientation of the crenels. The coupling Cauchy stress is deduced:

$$\boldsymbol{\sigma}_{coupling} = C_8(\delta) \ln(1 + |I_8 - I_9|) \mathbf{F}(\mathbf{E}_1 \otimes \mathbf{E}_2 + \mathbf{E}_2 \otimes \mathbf{E}_1)\mathbf{F}^T \quad (5.22)$$

A quadratic evolution of the parameter with the angle is chosen:

$$C_8(\delta) = a\delta^2 \quad (5.23)$$

where a is a material parameter.

5.2.3 Numerical study

The equivalent model, *i.e.* Eqs.(5.7)-(5.17)-(5.22), was implemented into a Finite Element (FE) code (Abaqus 2002) via an UMAT. Details about implementation can be read in Holzapfel [2000]; Federico *et al.* [2008] and Rebouah *et al.* [2013]. To validate the model, it is proposed to compare FE simulations to the experimental data of the architectured membranes. The equivalent model simplifies the FE calculus by not representing the details of the geometry of the crenelated membrane. Indeed the crenels add a lot of complexity and increase the number of needed elements in the meshes, so by means of the equivalent model it is now possible to sketch a simple geometry (a rectangular plate) and to deduce the behavior of real crenelated plate.

5.2.3.1 Validation of the model with experimental data without coupling

According to the experimental results presented in the first part, a comparison of the analytical simulations of the equivalent model is realized for each angle δ=0°, 45°, 90°, 135° and 180°. The results are presented in Fig.5.6. The values of the mechanical parameters used for the simulations are those of the bulk material and are the same as presented in section (3.3). In a first approach, the coupling term is not taken into account. It is observed that for $\delta = 0°$ and $\delta = 180°$ a good match between the model and the experimental results is obtained. Nevertheless for every other values of δ the model does not match perfectly with the experimental data, a little difference is observed for $\delta = 45°$ and $\delta = 135°$ and a more important difference is observed for $\delta = 90°$. These differences can be explained by the shear stresses between the core of the membrane and the crenels that were neglected in this first approach. As no angle variation are observed for 0 and 180°, there is no shear stress. It explains why the comparison between experimental data and analytical calculus are much better for these two orientations.

5.2.3.2 Validation of the model with experimental data with the coupling term

- Tensile tests

In this part, the coupling term is no longer neglected and the results of the analytical simulation are compared to the experimental data as illustrated in Fig.5.7. The only parameter fitted with the equivalent model is the parameter a for the quadratic function (Eq.5.23) which describes the evolution of the coupling term with the angle, a value of $a = 0.028$ MPa is obtained. It is observed that the use of the coupling term allows to have a better matching with the experimental results for each orientation of the crenels. The coupling term permits to take into account the amount of energy used to change the angle between the two crenels. It is important to note that by taking into account the coupling term, good comparison between experimental data and analytical results are obtained. The coupling term is thus a very important term and should not be neglected.

- Bulge test

It is proposed to test the constitutive equation in a complex loading FE calculation. A circular architectured membrane of 180 mm diameter with an orientation $\delta = 45°$ is

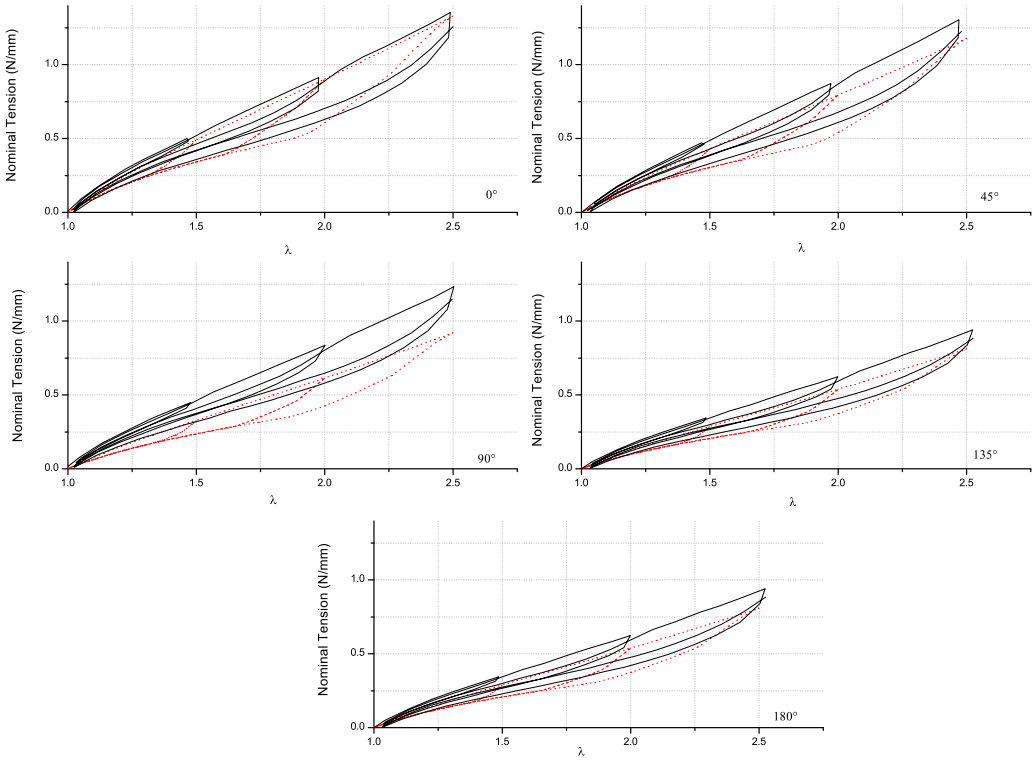

Figure 5.6: Comparison of experimental tests and the model of architectured membranes for different orientations of the crenels neglecting the shear between the crenels and the core of the membrane

simulated for a numerical bulge test. An experimental cyclic bulge test is also performed on this membrane. The strain state is controlled by pressure, thus the first cycle is reached for a pressure $p = 1.49$ kPa, the second for $p = 3.48$ kPa, the third $p = 5.31$ kPa and finally $p = 7.31$ kPa for the fourth loading. It is proposed to compare the results obtained along a radius of the circular plate. This path is defined to take into account the different biaxial loading states reached during a bulge test. As presented in Fig.5.8(a), the start point is the center of the plate which is close to an equibiaxial point (the equibiaxial point is only reached for an isotropic material) and the second point is at the fixing of the plate, it corresponds to pure shear [Machado *et al.*, 2012a]. Fig.5.8(b) represents the biaxility ratio along the path, defined as $\mu = \ln(\lambda_{\min})/\ln(\lambda_{\max})$ (where $\lambda_{\min}$ and $\lambda_{\max}$ are the minimum and maximum in-plane principal elongations) for a pressure level p=1.49 kPa. It is observed that the biaxiality ratio varies a lot between the two extremal loading points. Thus, this test permits to verify the robustness of the model on very different biaxial strain states. As observed in Fig.5.9, the logarithmic strain reached lasting the bulge test are not very important. Due to the geometry of the sample, it is not possible to

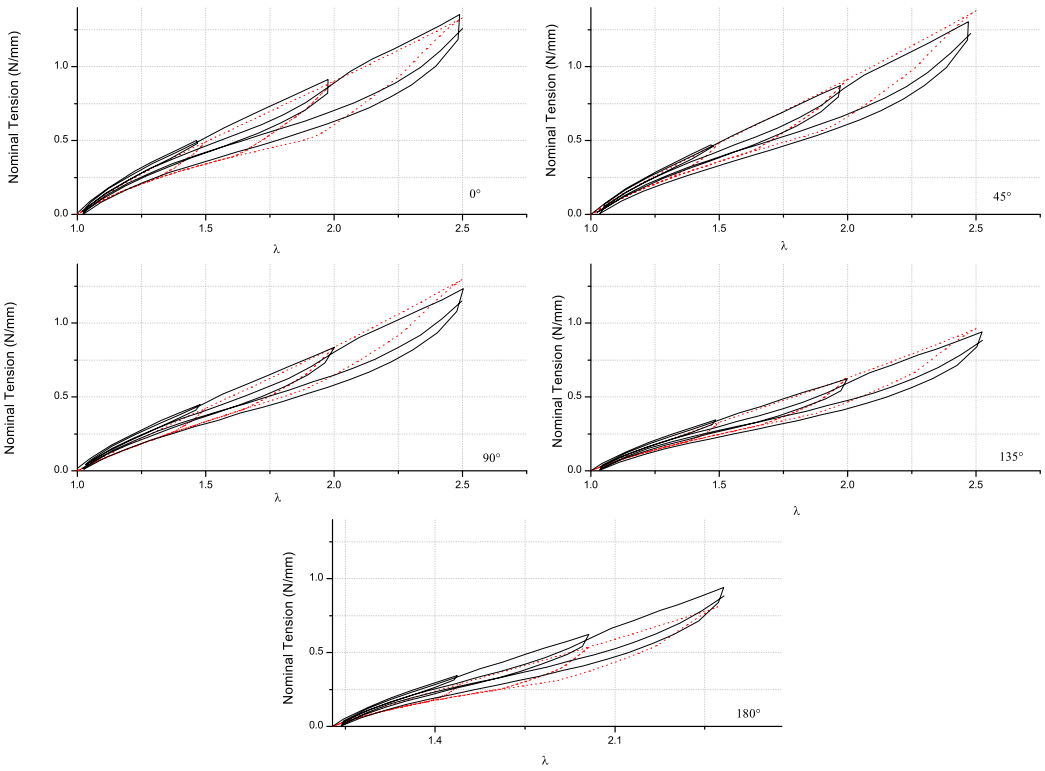

Figure 5.7: Comparison of experimental tests and the model of architectured membranes for different orientations of the crenels with coupling

reach a more important deformation state. For higher deformation levels, the crenels of the membranes do not allowed a 3D reconstruction of the image. Indeed, for high level of deformation some areas of the sample are not observed by the two cameras of the SDIC system, thus the reconstruction is impossible.

To highlight the stress softening, the mechanical behavior of the crenelated membrane is studied for the same pressure level for the different cycles performed during the test. Data were studied each time that the pressure level reached the values of 1.49 kPa and 3.48 kPa during the test as highlighted in Fig.5.10. The study of the different loads for the first pressure level is denoted as C_a, and four different load histories are considered $(1C_a, 2C_a, 3C_a, 4C_a)$. In the same way, the study of the second pressure level is denoted as C_b, in this case three different load histories are considered $(1C_b, 2C_b, 3C_b,)$.

The results obtained for the first and the second pressure levels are illustrated and compared to FE simulation in Fig.5.11. The figure highlights that the maximal in plane elongation λ_{max} and the minimal in plane elongation λ_{min} are approximately the same for the experimental results and for the FE simulations for the two pressure levels studied.

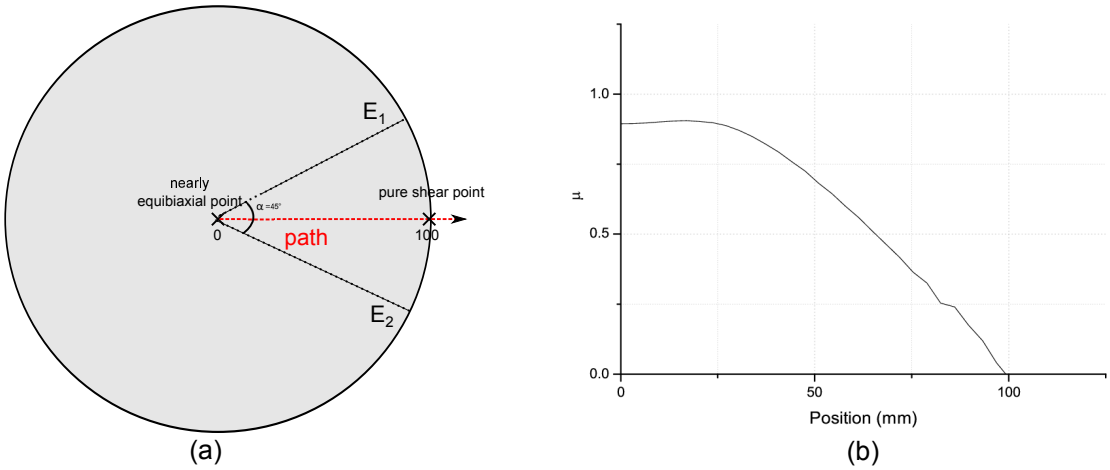

Figure 5.8: (a) representation of the studied path on the bulge test [Machado *et al.*, 2012b]. (b) Biaxility ratio along the path

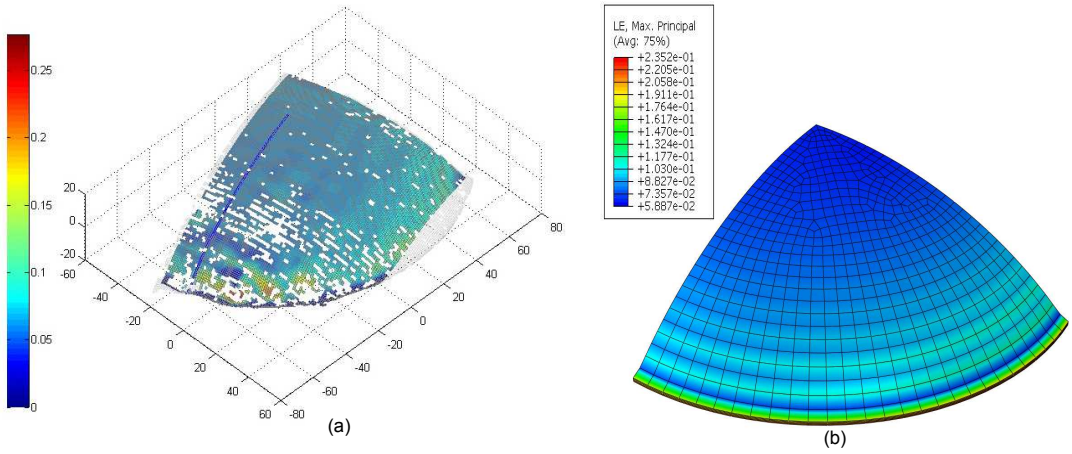

Figure 5.9: Comparison of the maximal logarithmic strain field of (a) experimental tests and (b) FE simulation with coupling for bulge test, δ=45°.

Nevertheless, for a pressure level of 1.49 kPa (C_a), it is observed that λ_{max} is more important for the fourth load ($4C_a$) than for the first load ($1C_a$), this is due to the Mullins effect. For λ_{min} the behavior is identical for the different loadings since the maximal deformations are endured by direction 1 and thus the stress softening is more important for this direction.

For a pressure level of 3.48 kPa (C_b), λ_{max} is a few superior for the third cycle ($3C_b$) than for the first loading ($1C_b$) and λ_{min} is equal for the three different histories. As for the previous pressure level this can be explained by the Mullins effect endured by the material. Moreover, for these two pressure levels, it can be assumed that the direction of the material in the third direction, *i.e.* along the thickness, is modified between the different loadings (but it cannot be studied with SDIC measurements). Since the material is considered incompressible, if the material does not endured deformation due to the Mullins effect

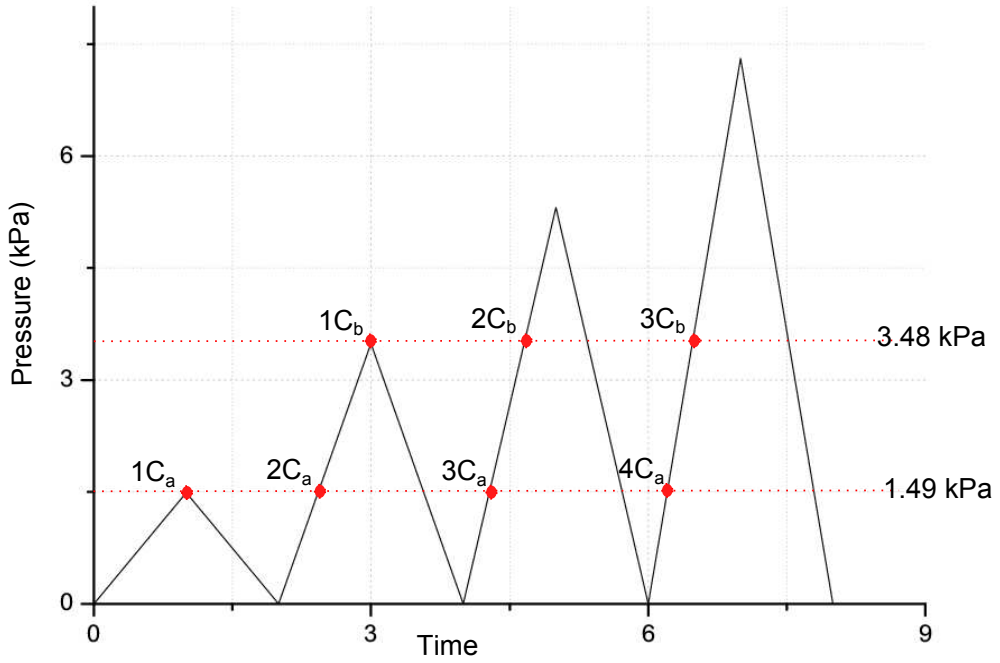

Figure 5.10: Representation of the two pressure levels studied for the bulge test

along direction 2 it supposed that the third direction endured deformations to respect the volume conservation. Nevertheless, all these simulations prove that the equivalent model is able to well describe the strain states in a complex structure calculation *i.e.* for non uniaxial loading states whereas the model was developed by means of uniaxial data.

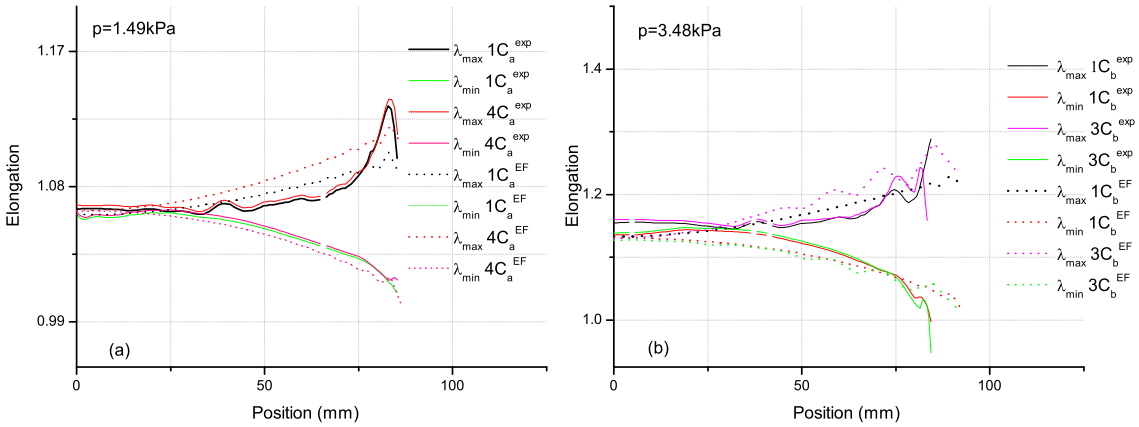

Figure 5.11: Comparison of experimental tests and FE simulation with coupling for bulge test on a sample with an angle δ=45°.

5.2.3.3 Discussion

About the model Two main points can be discuss, first an interpretation of the model and then an extension of the model to soft tissue. First for this equivalent model, it is

important to note that five different mechanical parameters exist. Four of them describe the behavior of the bulk material, and are fitted on a classic tensile test sample. The fifth parameter a of Eq.5.23 is the only one fitted on the crenellated membranes tensile tests. Then, by means of a theoretical analysis the influence of each part of the constitutive equation is evaluated for the different orientations of the crenels. The behaviors of the core of the membrane, of the crenels and of the coupling term are presented in Fig.5.12. For $\delta = 0°$, there is no coupling but the crenels represent 40% of the stress. For $\delta = 45°$, there is an influence of each part of the constitutive equation, whereas for $\delta = 90°$, the influence of the crenels becomes less important. For $\delta = 135°$, the influence of the crenels becomes almost equal to zero and the coupling term tends to zero that means that the crenels can quasi be neglected. Finally for $\delta = 180°$ it is observed that the crenels and the coupling do not have any influence on the behavior of the crenelated membrane, the core of the membrane endures all.

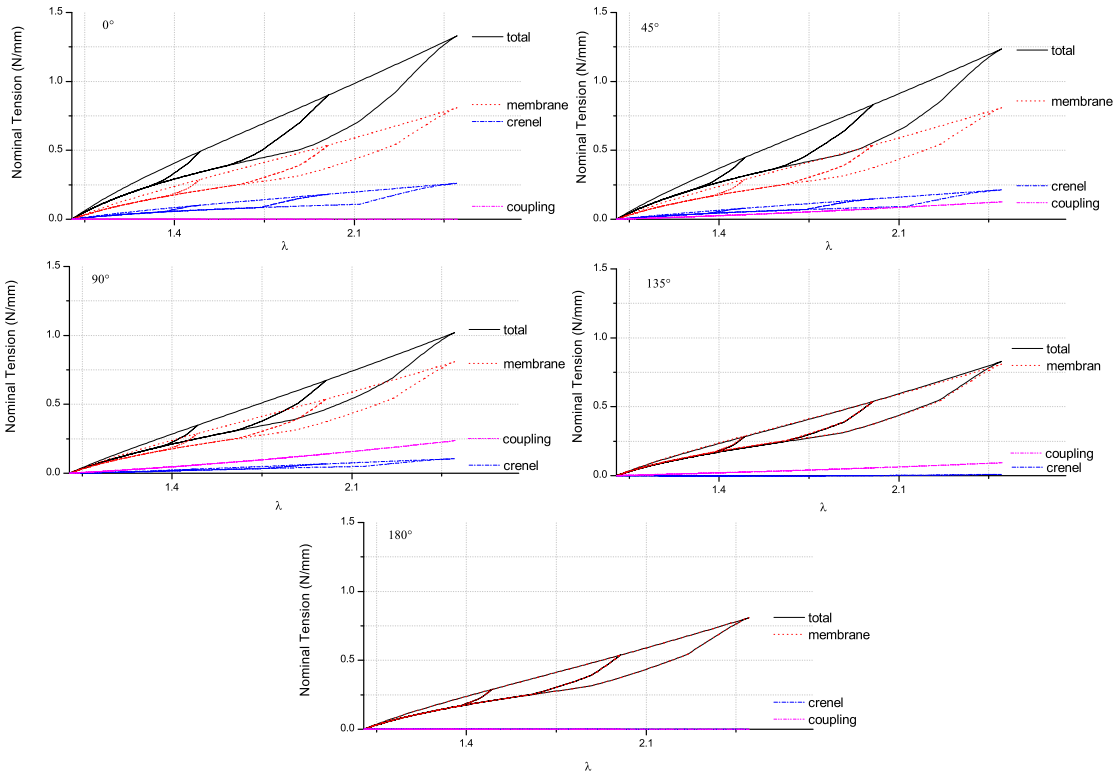

Figure 5.12: Influence of each term of tension for different values of δ.

- Extension of the model

As exposed in literature [Dunlop and Fratzl, 2013], it is to note that soft tissues can be considered as architectured materials. The presence of collagen [Holzapfel, 2000], into the matrix of the tissues creates an initial anisotropy in this natural material. The reinforcement of fibers induces different anisotropic behavior which depends on the orientation of the fibers. The equivalent model presented here can perfectly be adapted to soft tissue. The reinforcement of fibers corresponds to the crenel and the core of the membrane corresponds to the matrix. In an aim to create biomimetic membranes that can present behavior similar to soft tissues, the use of crenelated membranes is extrapolated. Living tissues are often characterized by a very different behavior into the two planar orthogonal directions which correspond to the tensile direction $\boldsymbol{x}$ and $\boldsymbol{y}$ for crenelated membrane (*i.e.* tension for δ and $180° - \delta$). In this way, Fig.5.13 presents some simulations for two orientations of the crenels. The Fig.5.13(a) presents exactly the behavior of the developed membranes ($\beta = \frac{1}{3}$). The anisotropy already important presents a difference of stiffness about 30%. Moreover, Fig.5.13(b) presents simulations for $\beta = \frac{2}{3}$, that means that the thickness of the crenels is now of 2 mm. In this case, the difference of stiffness is about 2. That means that it is possible to generate a membrane with two directions with very different mechanical behaviors. In order to come closer from soft tissues it would be necessary to use a silicone rubber that presents a more important strain hardening.

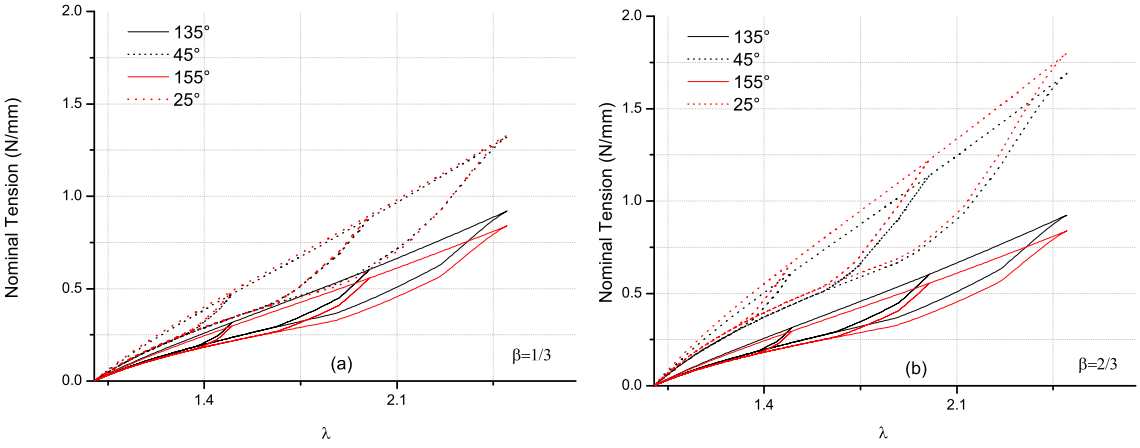

Figure 5.13: Representation of the behavior of a crenelated membrane for different orientation of the crenel for $\beta = \frac{1}{3}$ (a) or for $\beta = \frac{2}{3}$ (b).

5.2.4 Conclusion

Filled silicone crenelated membranes were molded for different orientations of the crenels. According to literature, and previous works, an existing model of filled silicone rubber was used. This model was adapted to the crenels and a coupling term was developed. Thus, every parts of the crenelated membrane can be evaluated. The constitutive equation obtained was implemented into a finite element code via an Umat. Several experimental tests were performed to validate the model. It was proved that the coupling term could not be neglected during cyclic tensile tests for different orientations of the crenels. Finally, a bulge test was performed to test the robustness of the model. Even if the deformations

reached are not very important for silicone rubber, it is observed that a good comparison between FE simulation and experimental results is obtained. By means of the equivalent model, complex structures can be easily simulated with one parameter more than the material parameters of the bulk material. Finally, the crenellated architectured membranes could be used in a biomimetic approach to be adapted to soft tissues.

5.3 Micro structural architectured membrane

This second section presents two microstructural architectured materials. The first material used is a RTV3428 but the fabrication process was changed in order to create a privileged direction of the macromolecular chains orientation. Thus, an initial anisotropy is imposed to the material. As previously, the material presents a stress softening, an induced anisotropy, a permanent set and hysteresis.
The second material used is a thermoplastic elastomer (TPE). This material was provided by "*Laboratoire de recherches et de contrôle du caoutchouc et des plastiques*" (LRCCP), its composition and process are few described in order to safeguard confidentiality of the project. As for the RTV3428, stress softening, permanent set and hysteresis are experimentally observed.
By means of the performed tests, a model is proposed to take into account all the non linear phenomena associated to the materials. It is proposed to take into account the hysteresis and the permanent set by means of viscoelastic constitutive equations and the stress softening and induced anisotropy by means of the constitutive equation presented in Chapter 2. Both are presenting a strong initial anisotropy, this typical material behavior is taken into account by means of a micro spherical approach. First section describes the elaboration of both materials and the mechanical tests carried out. Then a theoretical section presents the constitutive equations developed and finally a comparison with experimental data is done.

5.3.1 Materials and methods

5.3.1.1 RTV3428a

This section presents the first material used: a RTV3428 filled silicone. This silicone was already highly used in this thesis work, and particularly in the section (5.2) for geometrical architectured materials and Chapter 2. As previously observed by means of experimental tests, this filled silicone is initially isotropic. It is proposed to modify its microstructure to have an anisotropic behavior. To modify its behavior, the process to obtain a membrane was changed, the different steps are described in Fig.5.14. It is recalled that to obtain an isotropic RTV3428 membrane two components are mixed. The mixture is then put into a vacuum pump and finally injected into a mold. The mold is then placed into a oven for four hours at a temperature of $70°C$. But, here it is different, to obtain an anisotropic membrane with the same material, the injected mold is put 22 minutes in the oven at $70°C$. The vulcanization of the obtained membrane is not fully performed after being remove from the mold, then the membrane is put into a clipping system that imposed a tension deformation of approximately 60%. The system is put in the oven at a

temperature of 150°C for two hours. The new material obtained is denoted as RTV3428a and represents the anisotropic membrane made of filled silicone rubber RTV3428. The isotropic membranes are still denoted as RTV3428. The step 5 represented in Fig.5.14

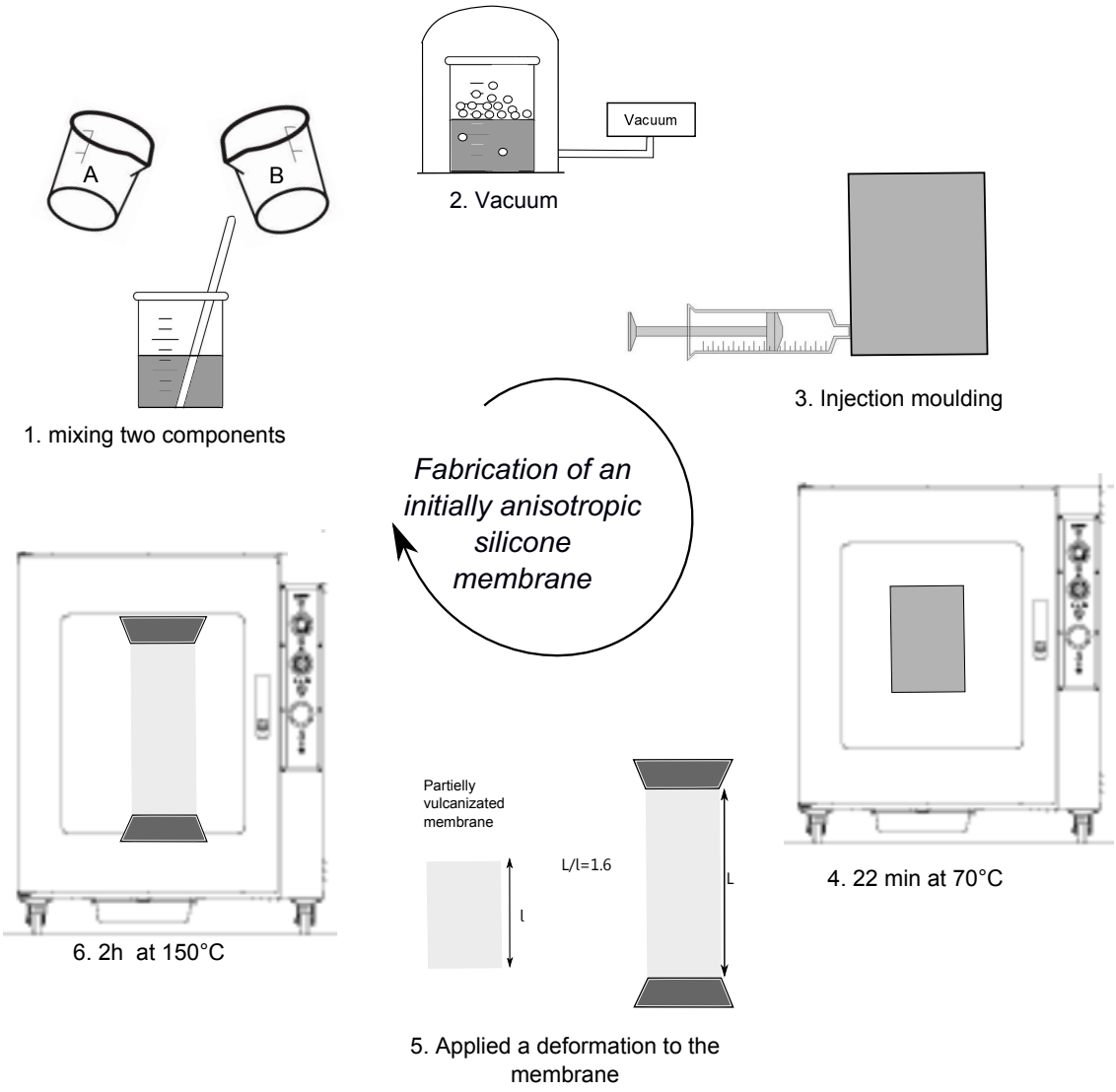

Figure 5.14: Elaboration of the micro structural architectured membrane of filled silicone

is the step that permits to create a preferential orientation of the macromolecular chains in the material. Since the membrane is put in the oven for a second vulcanization in a deformed state, the chain directions stay as imposed by the system (in the tensile direction).

5.3.1.2 TPE

As this material was provided by the LRCCP, the elaboration and the composition of this material is confidential. Nevertheless, it is assumed that during the process of the membrane elaboration a preferential direction is imposed to the chains by calendaring.

5.3.1.3 Experimental tests

To highlight the mechanical behavior of the two materials, two typical tests were performed. Each material is initially presented as a membrane as presented in Fig.5.15. The RTV3428a membrane dimensions after the second vulcanization are 150mm long, 70mm wide and 1.6mm thick, for the TPE the membrane dimensions are 150mm long, 100mm wide and 2mm thick. For each material three oriented samples at 0°, 45° and 90° are cut in the middle of the membrane to avoid edge effects, considering that 0° matches to the preferential direction imposed to the macromolecular chains for both processes as illustrated in Fig.5.15.

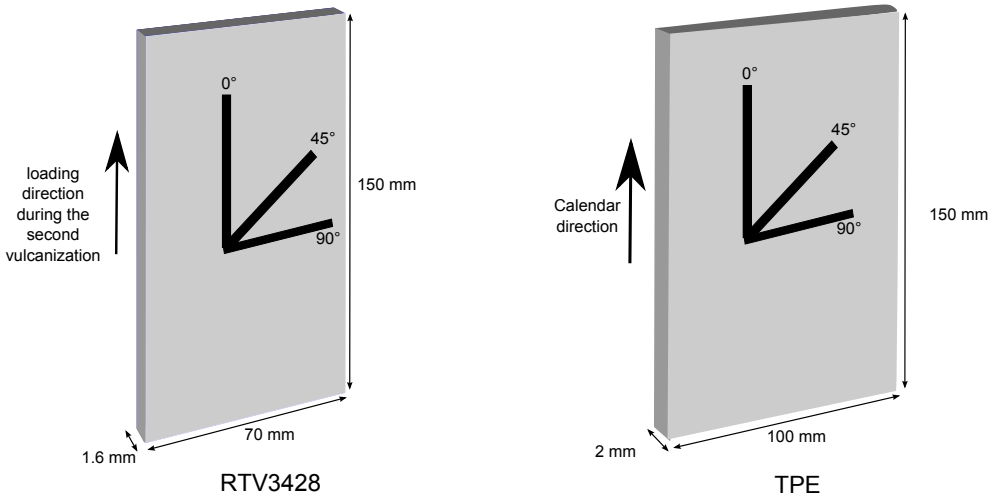

Figure 5.15: Representation of the membrane and the oriented samples for the RTV3428a and the TPE materials

For the first test, each one of the oriented samples are submitted to a cyclic loading up to $\lambda = 1.5$, then up to $\lambda = 2$ and finally up to $\lambda = 2.5$. Each cycle is repeated twice before to reach a new strain state, this test is represented at the top of the Fig.5.16 and Fig.5.17 and is carried out at a strain rate of $\alpha = 0.016\text{s}^{-1}$. The results obtained for both materials are presented on the same figures.

Fig.5.16 highlights the mechanical behavior of the RTV3428a for the three oriented samples. It appears that the material presents a stress softening, a hysteretic behavior and a permanent set. Furthermore, the results highlight that the elaborating process is efficient to generate anisotropy in the RTV3428a. The sample cut at 0° (which is the same direction as the loading direction imposed during the second vulcanization) presents the most important stress hardening. Then the sample cut at 45° presents less stress hardening and finally the sample cut a 90° is the softest. A multiplicative factor of approximately 1.3 is calculated according to the maximal stress reached between the sample cut at 0° and the one cut at 90°. This proves that the second vulcanization undergone by the membrane modified the micro-structure of this filled silicone. As the test was performed at a high strain rate, it appears that the material presents a permanent set (at the unloading and re-loading), whereas it was not observed in the previous studies on the RTV3428 at slower strain rates.

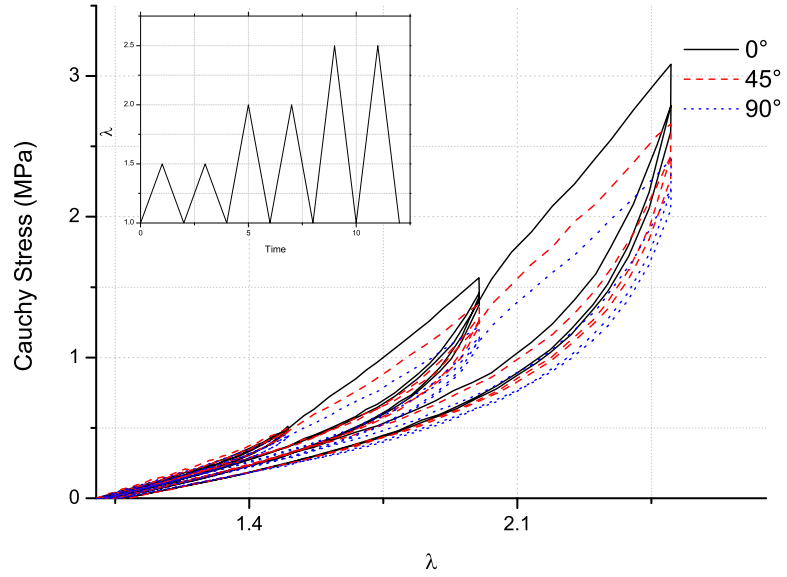

Figure 5.16: Cyclic tensile test performed on the RTV3428a architectured membrane

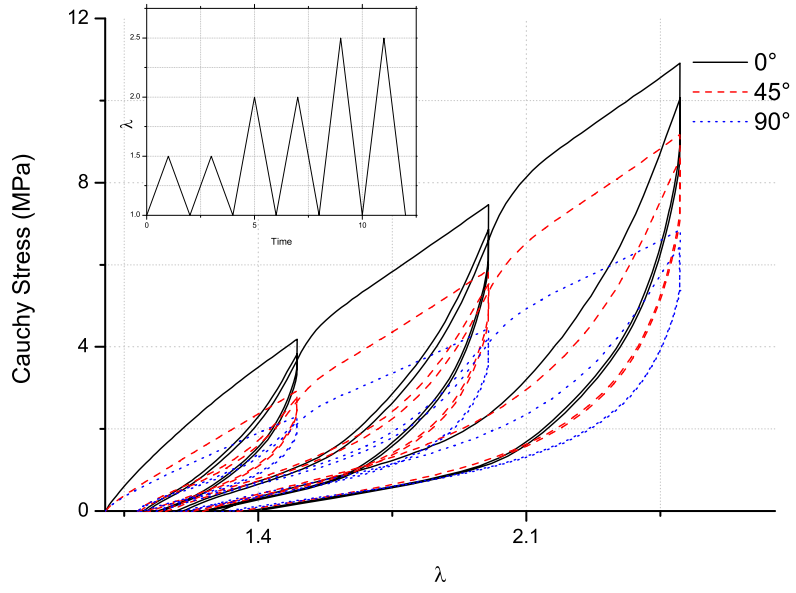

Figure 5.17: Cyclic tensile test performed on the micro architectured membrane of TPE

Similar results are obtained for the TPE in Fig.5.17, the same phenomena observed for the RTV3428a are also observed for the TPE. Indeed, stress softening, hysteretic behavior, permanent set and initial anisotropy are also observed. Unlike for the RTV3428a, all these effects are more important for the TPE. The stress softening observed is very important as the permanent set which is approximately equal to a third of the imposed strain. In the same way, the anisotropic factor, based on the maximal stress reached, obtained between the sample cut at 0° and the one cut at 90° is approximately of 1.5. This factor is greater than the one obtained for the RTV3428a, it proves that the TPE presents a more important initial anisotropy.
The second test performed is a cyclic tensile test where relaxation times are imposed at different strain states during loadings and unloadings. As previously, three oriented samples are cut in the micro architectured membranes of both materials. Each sample is submitted to a load up to $\lambda = 1.5$ followed by a relaxation time of 30 minutes, then up to $\lambda = 2$ followed by a relaxation time of 30 minutes and up to $\lambda = 2.5$, then an unload until $\lambda = 2$ followed by a relaxation time of 30 minutes and then up to $\lambda = 1.5$ followed by a relaxation time of 30 minutes and back to $\lambda = 1$. This cycle is repeated twice at a strain rate of $\alpha = 0.016\text{s}^{-1}$. The obtained results and the imposed loading are represented in Fig.5.18 for the RTV3428a and Fig.5.19 for the TPE.

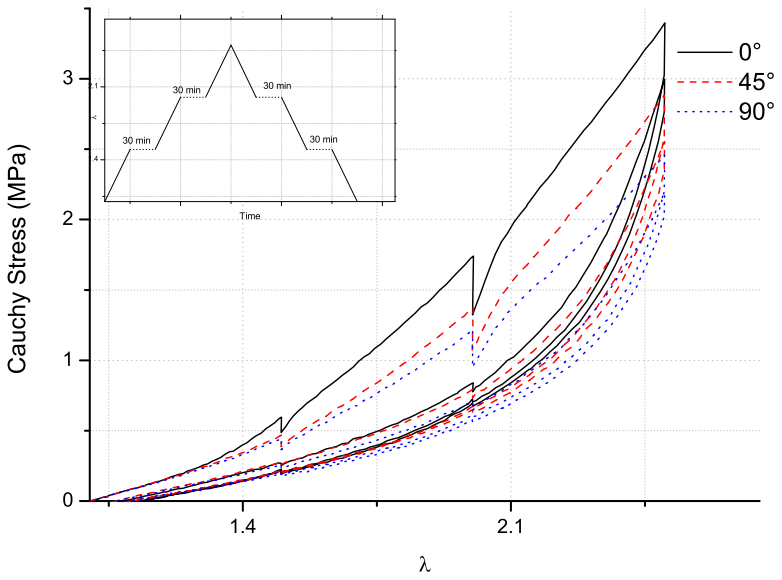

Figure 5.18: Cyclic tensile test with imposed relaxation time performed on the RTV3428a membrane

For the RTV3428a, this test highlights that the material presents few viscous effects. The stress softening is still the major non linear effect associated to the mechanical behavior. Nevertheless, the test shows that the relaxation time imposed during the first loading lead to an important decrease of the stress compared to the unloading and the second loading. These results supposed that an important part of the relaxation of the first loading is due

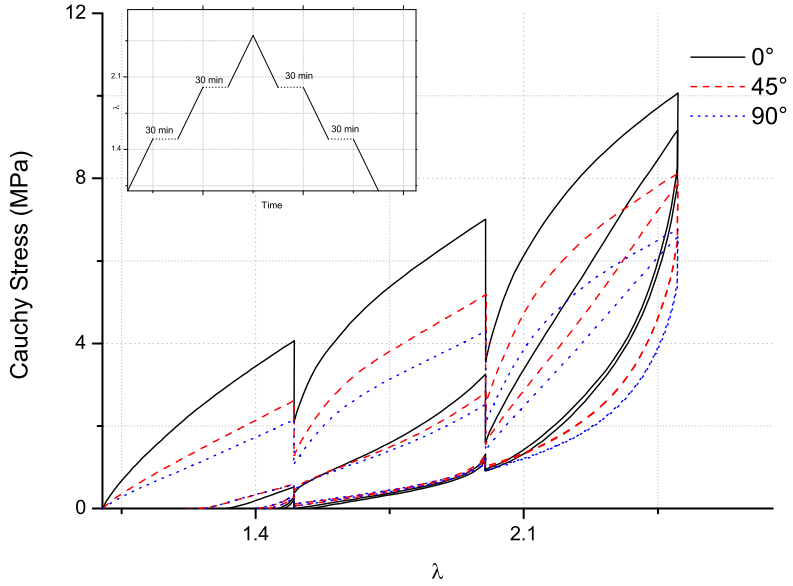

Figure 5.19: Cyclic tensile test with imposed relaxation time performed on the TPE

to the Mullins effect. The test highlights too that the material presents a weak hysteresis for the second loading. In the same way there is very few permanent set observed, even at a strain rate of $\alpha = 0.016\text{s}^{-1}$.
At the opposite, the TPE presents very important viscous effects. Relaxations are very important for the first and second loadings. It is observed that for the second loading and unloading, the stress relaxations are weaker at $\lambda = 1.5$ than at $\lambda = 2$, this is due to the permanent set of the material which appears at 50% of global deformation, where the first relaxation time is imposed. However, this material presents a weak hysteretic behavior, indeed if equilibrium curves are considered, it appears that they would be identical for the second unloading and the unloading, the relaxation point of the second loading and the unloading reached the same stress state. The mechanical behavior observed for both materials is identical for the three oriented samples. The initial anisotropy influences all the non linear phenomena but the mechanical behavior is still similar.

5.3.2 Constitutive equations

This section aims to propose a constitutive equation that permits to take into account the mechanical behavior of the architectured materials. The materials experimentally studied have a homogeneous structure. No geometric assumptions are needed unlike it was proposed for the crenelated membranes. As all non linear phenomena have already been taken into account in the last chapters, the previous models based on micro spherical approach are used to take into account the mechanical behavior of these architectured materials.
In a first approach, the new constitutive equation proposed were built by using only simple

strain energy. Indeed, the aim is first to take all the phenomena into account. In this way, qualitative predictions are expected here, to permit a better understanding of the functionality of the model, which can be divided in three parts.
First, the hyperelastic behavior is taken into account by means of a Neo Hookean model. Then the second part described the visoelasticity by means of the simplest model proposed Huber and Tsakmakis [2000], and finally the stress softening is taken into account by means of the model proposed in Chapter 2. The determination of the total stress is identical as the one presented in the last chapter in Eq.(4.20) for both studied materials:

$$\sigma = \sum_{i}^{42} \omega^{(i)} \left(2C_1 \left({\lambda^{(i)}}^2 - \frac{1}{\lambda^{(i)}} \right) + 2C_2 \left({\lambda_e^{(i)}}^2 - \frac{1}{\lambda_e^{(i)}} \right) + 2{\lambda^{(i)}}^2 \mathcal{F}^{(i)} \frac{\partial W_{cf}}{\partial I_4^{(i)}}^{(i)} \right) \mathbf{a}_n^{(i)} \otimes \mathbf{a}_n^{(i)} \tag{5.24}$$

To take into account the initial anisotropy of the materials, the parameters of the different parts of the model are considered as dependent of the direction in the micro sphere. First, the hyperelastic behavior is turned anisotropic by means of C_1 which becomes different for each direction of the micro sphere to become ${C_1}^{(i)}$. In the same way the material parameter of the viscoelastic part represented by C_2 becomes ${C_2}^{(i)}$. It is important to note that the initial anisotropy can also be induced by means of the material parameter $\eta_0^{(i)}$ used in the viscoelastic part to describe the evolution equation of $\lambda_e^{(i)}$ in Eq.(4.22) as $\dot{\lambda}_e^{(i)} = {\lambda_e}^{(i)} \frac{\dot{\lambda}^{(i)}}{\lambda^{(i)}} - 4\frac{C_2}{3\eta_0^{(i)}} \left({\lambda_e^{(i)}}^3 - 1 \right)$ can also be considered as dependent of each direction.
For the stress softening part the equations presented in last chapters are used. For both materials the same evolution function $\mathcal{F}^{(i)}$ is used as presented is Eq.(2.3) such as:

$$\mathcal{F}^{(i)} = 1 - \eta_m^{(i)} \sqrt{\frac{I_{1\max} - I_1}{I_{1\max} - 3}} \left(\frac{I_{4\max}^{(i)} - I_4^{(i)}}{I_{4\max}^{(i)} - 1} \right) \left(\frac{I_{4\max}^{(i)}}{I_{4\max}} \right)^4 \tag{5.25}$$

Where the material parameter $\eta_m^{(i)}$ can be considered as dependent of each direction to induced initial anisotropy.
Due to the differences observed experimentally between both materials, the strain energy used to describe the RTV3428a and the TPE are different.

- Indeed, for the the same strain energy as the one used for the RTV3428 in Chapter 2 is used: $\mathcal{W}_{cf}^{(i)} = K(I_4^{(i)} - 1)^2$, where K is a material parameter. To take into account the initial anisotropy of the material a different value is assigned to K for each direction and the following strain energy is used $\mathcal{W}_{cf}^{(i)} = K^{(i)}(I_4^{(i)} - 1)^2$.
- For the TPE, which is a new studied material, the strain energy used is identical as the one used in Chapter 3 in Eq.(3.2), and is defined as $\mathcal{W}_{cf}^{(i)} = \frac{K^{(i)}}{2} \int \sqrt{\frac{I_4^{(i)} - 1}{I_4^{(i)}}} dI_4^{(i)}$. As for the RTV3428a, K became $K^{(i)}$ to take into account the initial anisotropy.

Finally the stress endured by each direction for the two materials is:

$$\sigma = \sum_{i}^{42} \omega^{(i)} \left(2{C_1}^{(i)} \left({\lambda^{(i)}}^2 - \frac{1}{\lambda^{(i)}} \right) + 2{C_2}^{(i)} \left({\lambda_e^{(i)}}^2 - \frac{1}{\lambda_e^{(i)}} \right) + 2{\lambda^{(i)}}^2 \mathcal{F}^{(i)} \frac{\partial W_{cf}^{(i)}}{\partial I_4^{(i)}} \right) \mathbf{a}_n^{(i)} \otimes \mathbf{a}_n^{(i)} \tag{5.26}$$

To conclude, five parameters permit to handle the initial anisotropy, ${C_1}^{(i)}$ for the hyperelastic part, ${C_2}^{(i)}$ and $\eta_0^{(i)}$ for the viscoelastic part and $K^{(i)}$ and $\eta_m^{(i)}$ for the stress softening part.

5.3.3 Comparison with experimental data

5.3.3.1 RTV3428a

According to the constitutive equations defined previously a comparison is proposed with the experimental data. To have good match, the parameters values are chosen according to the experimental observations. First, the stress softening is considered as similar for each oriented tensile test as illustrated in Fig.5.18, so the material parameter $\eta_m^{(i)}$ is considered as identical for all the directions such as $\eta_m^{(i)} = 4$. In the same way, the material parameter $\eta_0^{(i)}$ that takes into account the dependance of the behavior on the strain and that permits to define the increase stiffness and the size of the hysteresis loop, is also considered as similar for all directions. the value for this material parameter is equal to $\eta_0^{(i)} = 200\text{MPa.s}^{-1}$.
The three other mechanical parameters are considered as dependent on the directions. By means of the variation of the parameter ${C_1}^{(i)}$ for each direction the hyperelasticity is represented as initially anisotropic, in the same way the viscoelasticity is turned anisotropic by means of the parameters ${C_2}^{(i)}$ that represent the additional stiffness reached at high strain rate, and the parameters $K^{(i)}$ that represent the stiffness of the stress softening of each direction, vary also according to the spatial repartition.
It was experimentally observed that the stress is maximal for the tension direction, and at the opposite the orthogonal direction is less stressed. As all the phenomena are maximal for the tension direction, the material parameters for each direction are chosen to be maximal in the tension direction (also the imposed direction during the process) and minimal in the orthogonal direction. The variation of the mechanical parameters according to the spatial repartition permits to increase or decrease the initial anisotropy of the material. According to the representation of the spatial repartition of Bazant as represented in Fig.4.11, the closest directions of the micro sphere to the preferential direction induced by the process (i.e. direction 1 in Fig.4.11) are the directions with the highest material parameter values. A more important variation in the parameter is imposed for the hyperalsatic and stress softening part than for the viscoelastic part. Indeed, only a few anisotropy is observed for the viscoelastic behavior (Fig.5.18). This repartition for the material parameters can be adjusted for any material. The proposed values were fitted to propose one solution. Other distributions of the material parameters could be proposed, for instance by considering that the material parameter η_0 depends on each directions. The materials parameter used in each direction are presented in the table.5.1.

Table 5.1: Material parameters for the RTV3428a

n°	${C_1}^{(i)}$ MPa	${C_2}^{(i)}$ MPa	$K^{(i)}$ MPa
1	0.1900	0.350	0.360
2	0.1330	0.280	0.252
3	0.1330	0.280	0.252

4	0.1615	0.280	0.306
5	0.1615	0.280	0.306
6	0.1615	0.280	0.306
7	0.1615	0.280	0.306
8	0.1235	0.315	0.144
9	0.1235	0.315	0.144
10	0.1615	0.210	0.216
11	0.1615	0.210	0.216
12	0.1615	0.210	0.216
13	0.1615	0.210	0.216
14	0.1615	0.210	0.216
15	0.1615	0.210	0.216
16	0.1615	0.210	0.216
17	0.1615	0.210	0.216
18	0.1710	0.315	0.324
19	0.1710	0.315	0.324
20	0.1710	0.315	0.324
21	0.1710	0.315	0.324

The results are presented in Fig.5.20 for the three oriented samples studied. It appears that, even if the mechanical behavior is not perfectly represented, all the non linear phenomena are described: the initial anisotropy, the stress softening and the viscous effects are taken into account.
To have a better match with the experimental data it would be necessary to use a most robust model. Particularly for the viscous effects, a non linear evolution equation would be necessary. In the same way, a Neo Hookean model is not the most adapted to represent this typical mechanical behavior. The stress softening is not well described at large deformations, a different evolution function should be used to represent the fast decrease of the stress at large strain states. Nevertheless, even with this simple model, all the non linear phenomena are described.

5.3.3.2 TPE

The constitutive equation proposed previously is also applied to the TPE. The determination of the material parameters is similar as the one proposed for the RTV3428a. In this way, and based on the experimental observations, it was chosen to consider that the stress softening of the material and the viscous effects endured by each directions are similar. The material parameters $\eta_0^{(i)} = 500\text{MPa.s}^{-1}$, $\eta_m^{(i)} = 8$ are identical for each directions. The initial anisotropy is induced by means of the material parameters ${C_1}^{(i)}$ for hyperelasticity, ${C_2}^{(i)}$ for the viscoelasticity and $K^{(i)}$ for the Mullins effect. It is important to note that for this material, the anisotropy is considered as important for the stress softening part and for the hyperelastic part. The anisotropy of the viscoelastic part is less important than for the two other parts as for the RTV3428a. As previously the material parameters values depend on the spatial repartition of the directions proposed by Bazant in Fig.4.11.

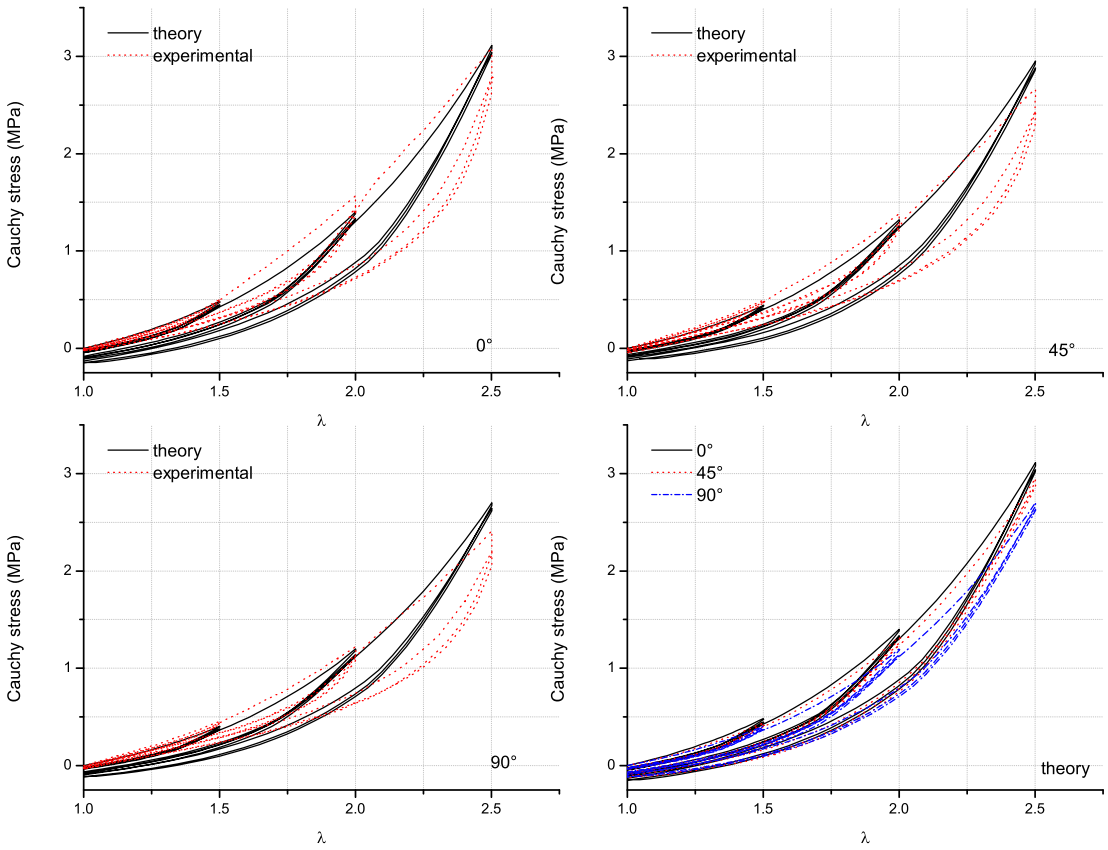

Figure 5.20: Comparison with the experimental data of cyclic tensile test on RTV3428 for the different oriented samples

More the direction is close to the direction 1 more the value is important. The parameter values are presented in the table.5.2 and the results are presented in Fig.5.21.

Table 5.2: material parameter TPE

n°	$C_1{}^{(i)}$ MPa	$C_2{}^{(i)}$ MPa	$K^{(i)}$ MPa
1	1.20	1.900	4.80
2	0.48	0.570	1.92
3	0.48	0.570	1.92
4	0.96	1.235	3.84
5	0.96	1.235	3.84
6	0.96	1.235	3.84
7	0.96	1.235	3.84
8	0.48	0.570	1.92
9	0.48	0.570	1.92

10	0.72	1.045	2.88
11	0.72	1.045	2.88
12	0.72	1.045	2.88
13	0.72	1.045	2.88
14	0.72	1.045	2.88
15	0.72	1.045	2.88
16	0.72	1.045	2.88
17	0.72	1.045	2.88
18	1.08	1.520	4.32
19	1.08	1.520	4.32
20	1.08	1.520	4.32
21	1.08	1.520	4.32

For this material, the comparison with the experimental data is not well described. This is partially due to the non linear phenomena which are very important for this material compared to the RTV3428a and due to the limits of00 the present model. The initial anisotropy that represents the hardening of the material is well described for the three oriented samples compared to the stress softening which is very important and the viscous effects that imposed too much permanent set to be properly described. Nevertheless, the proposed model is a first approach and all the phenomena are qualitatively described. The limits are well highlighted too, and the results permit to define a new way for the development of an efficient model.

5.3.4 Discussion

This section presented two different materials initially anisotropic by means of a microstructural architecture issued from two different processes. Both materials present non linear phenomena as initially anisotropy, stress softening, and viscous effects. It appears that with simple linear constitutive equations these non linear phenomena can be qualitatively described by the proposed model but a perfect match cannot be obtained, particularly if the non linear phenomena are very important. Indeed, a most robust constitutive equation for hyperelasticity, stress softening and viscous effects should be used. Non linear law are needed to represent the highly non linear mechanical behavior of these materials. For instance the Bergstrom and Boyce [1998] model to take into account the viscous effect is more efficient than the Huber and Tsakmakis [2000] model as illustrated in Chapter 4.

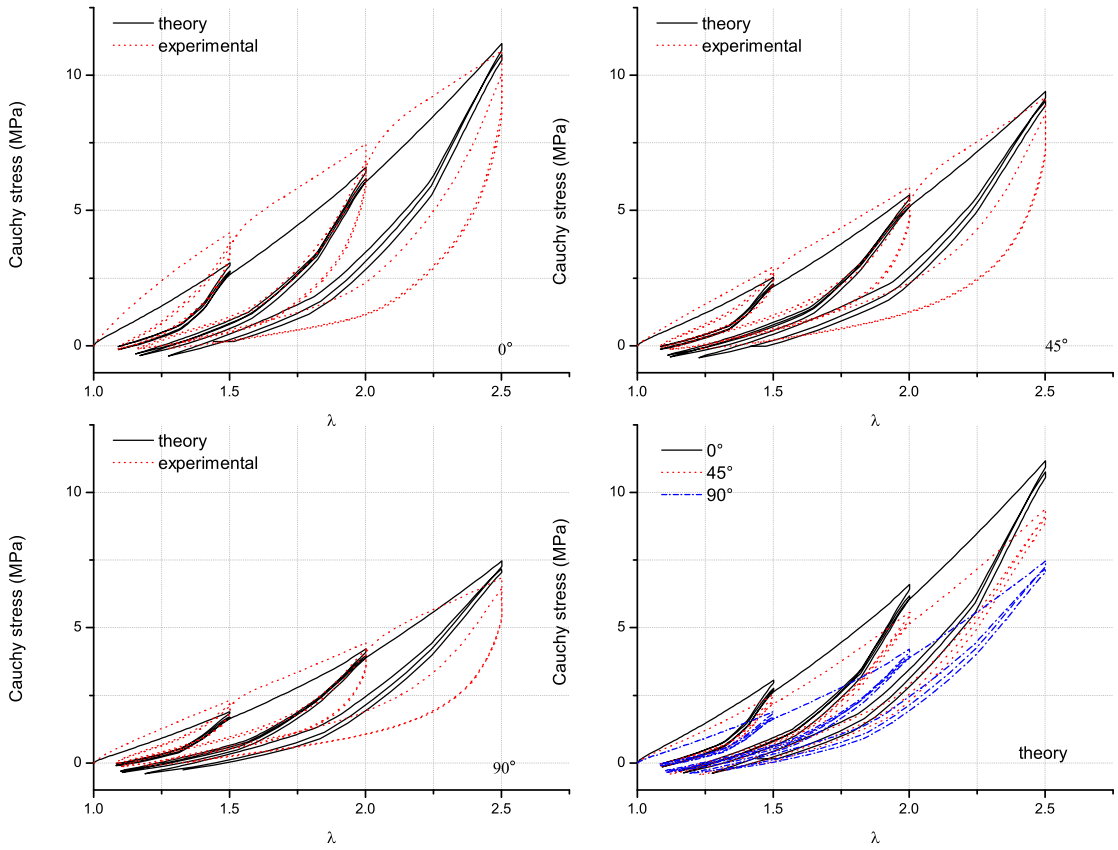

Figure 5.21: Comparison with the experimental data of cyclic tensile test on TPE for the different oriented samples

5.4 General conclusion

This chapter presented a study of architectured materials. These materials are more and more used due to their particular mechanical properties. Two types of architectured material were presented, first a geometrically architectured one and then a micro structural architectured one. The geometrically architectured material was obtained by injection molding and a control of the initial anisotropy is induced by means of oriented crenels on the external surfaces of the central membrane. The main advantage of this material is that the bulk material is isotropic, thus even if initially anisotropy is induced by means of the geometry the material parameters are identical on all the sample, the anisotropy is controlled by means of geometrical parameters. Furthermore all the other non linear phenomena as stress softening or permanent set are similar in the membrane and in the crenels. The assumption of tension compression was made for the crenels, and good approximation with experimental data was obtained with the use of a coupling term. Only

one mechanical parameter is added to the constitutive equation compared to the constitutive equation of the bulk material. Furthermore an equivalent constitutive equation was proposed and implemented into a FE code via UMAT. Validation for complex loading was obtained between an experimental and a numerical bulge test.
Then, two micro mechanical architectured materials were obtained in two different ways. First, the RTV3428 is turned anisotropic by means of a second vulcanization by applying a deformation state and is called RTV3428a, and a TPE is initially anisotropic by means of another process. In both cases an orientation of the chains is imposed to the material to create a micro structural architecture. Those materials present stress softening, initial anisotropy and for these two specific materials the viscous effects are no longer neglected. The hysteretic behavior and the permanent set are taken into account, even if for the RTV3428a the effects are weak. It appears that the proposed constitutive equation can qualitatively describe all the non linear phenomena. The constitutive equations are not able to described well the mechanical behavior. Most robust laws are required to take well into account such mechanical behavior.
The two proposed model are based on two different modeling approaches. In the case of the architectured membrane, a matrix is considered isotropic and 42 identical directions are used for the 3D homogeneization. Moreover, the two reinforced directions (crenels) induced the anisotropy of the material. Two other directions are added in the modeling, it is considered that both directions have the same mechanical behavior. This approach is close to the experimental observations and hypothesis applied to soft tissues. For example, in arteries or esophageal tissues, an extra cellular matrix (isotropic) which contain oriented fibers (collagen).
The second approach permits to consider a homogeneous material, but the modeling approach is different. By considering a homogenization with the 42 directions of Bazant and Oh [1986], it is assumed that all the directions can be different, in this way an initial anisotropy is induced to the material by considering that the mechanical properties of each directions are different

General conclusion

Conclusions

This thesis work presented a study mainly lead on rubber like materials. Experimental tests were performed on different rubber like materials such as: filled silicone rubber (RTV3428), Hot Temperature Vulcanization filled rubber (HTV), Nitril Butadien Rubber (NBR) and ThermoPlastic Elastomers (TPE). Each one of these materials presents a different mechanical behavior, and permits to focus on one particular phenomenon as stress softening, induced anisotropy, permanent set and viscous effects. In this way, a model was built step by step by adding gradually non linear phenomena.

First, only the stress softening and the induced anisotropy were taken into account. The proposed model permit to take into account simultaneously the global and the directional maximal deformation endured by the material during loadings by means of the micro spherical approach. Then the permanent set was added to the model without adding new material parameters. It involves that the stress softening and the permanent set of a material are dependent. Comparisons of these tests with experimental data performed on a HTV were proposed. Thereafter, an extension to soft tissues was proposed by taking into account the initial anisotropy. The model, able to described stress softening, permanent set and initial anisotropy, was validated on experimental tests performed on ovine vena cava. These data were issue from literature Peña *et al.* [2009]. These models were implemented in a FE code by means of a strain invariant formulation. The robustness of the model was validated on complex structures or complex loading such as an holey plate or a bulge test.

Next, the time dependency of the material was then analyzed. In this way, classical viscoelastic models were studied and adapted to a micro spherical approach. One simple Internal Variable Model (IVM) and one simple Convolution Integral Model (CIM) were used in a first approach to highlight that a micro sphere approach permits to improve the classical formulation. Numerical tests highlighted that by means of the micro spherical approach, classical mechanical tests such as equibiaxial and pure shear tests can be well taken into account with this approach.

Experimental tests were carried out on a NBR to study the influence of the viscous effects,

and four preexistent models (only the IVM approach was used), issue from literature, were extended to a micro spherical approach. The stress softening was added to the modeling and the ability of the models were validated on experimental data. It appears that simple linear evolution equations permit to qualitatively describe the experimental data, even if the non linear evolution equation permits to have better matches.
Finally, architectured materials were used to develop a way to take into account and control the initial anisotropy of the materials. In this way, geometrical and micro structural architectured materials were used. For geometrical architectured materials, a crenellated membrane with different orientations of the crenels was studied and an equivalent model that takes into account geometrical parameters, stress softening, induced anisotropy and initial anisotropy was proposed and implemented in a FE code. In the case of micro structural architectured materials the viscoelasticity was added to the modeling. By means of the micro spherical approach, the initial anisotropy of the material can be handled for all non linear phenomena by applying a different value of the mechanical parameters according to the considered direction. The model was validated on experimental data. In a first approach simple laws were used to highlight qualitative comparisons, but more complex models can be adapted to have a better comparison with experimental data.

Perspectives

New models and modeling principles were developed on rubber like materials, and can be now easily extended to soft tissues. It would be, for instance, necessary to adapt the different strain energies, but the structure of the model would not be changed. The main advantage to have built the model on rubber like materials is that the model is now perfectly controlled.
Nevertheless, there exist still difficulties to properly determine the values of the mechanical parameter especially to take well into account the anisotropic mechanical behavior of materials. Another important perspective of this work is to carry out experimental tests on soft tissues to test abilities of the models.
Another aim would be to implement the viscoelastic part of the model, in this way all the phenomena could be anticipated and predicted. This model would be useful for rubber like materials and soft tissues. The viscoelastic models proposed need to be improve to have a good matches with experimental data. It would interesting to work on a new formulation that would permit for instance to take into account simultaneously the different size of hysteresis that could be observed on complex loading such as cyclic tensile test with intern subloops.
Finally, all numerical tools, to propose new biomimetic materials, are available. By considering geometrical architectured materials, a numerical implementation of the equivalent model is already efficient. It could be a good way to investigate optimized design for prosthesis.

Appendix

A The material directions construction

The proposed model uses $n = 2 \times 21$ integration points with cartesian coordinates defined in Table A.1. Only the 21^{st} direction are summarized, the 21 others are their opposite. The directions are represented on the unit sphere by the end point of each vector, the origin being the point O for each vector. Some points are represented for a eighth of space in Fig. A.1. The other directions are obtained by a symmetry with respect to the plan (O, X_1, X_2); (O, X_2, X_3) et (O, X_1, X_3).

Table A.1: Direction cosines and weights for 2×21 points (orthonormal symmetries) of each vector $\mathbf{a}_0^{(i)}$.

i direction	X_1	X_2	X_3	w
1	0	0	1	0.0265214244093
2	0	1	0	0.0265214244093
3	1	0	0	0.0265214244093
4	0	0.707106781187	0.707106781187	0.0199301476312
5	0	-0.707106781187	0.707106781187	0.0199301476312
6	0.707106781187	0	0.707106781187	0.0199301476312
7	-0.707106781187	0	0.707106781187	0.0199301476312
8	0.707106781187	0.707106781187	0	0.0199301476312
9	-0.707106781187	0.707106781187	0	0.0199301476312
10	0.836095596749	0.387907304067	0.387907304067	0.0250712367487
11	-0.836095596749	0.387907304067	0.387907304067	0.0250712367487
12	0.836095596749	-0.387907304067	0.387907304067	0.0250712367487
13	-0.836095596749	-0.387907304067	0.387907304067	0.0250712367487
14	0.387907304067	0.836095596749	0.387907304067	0.0250712367487
15	-0.387907304067	0.836095596749	0.387907304067	0.0250712367487
16	0.387907304067	-0.836095596749	0.387907304067	0.0250712367487
17	-0.387907304067	-0.836095596749	0.387907304067	0.0250712367487
18	0.387907304067	0.387907304067	0.836095596749	0.0250712367487
19	-0.387907304067	0.387907304067	0.836095596749	0.0250712367487
20	0.387907304067	-0.387907304067	0.836095596749	0.0250712367487
21	-0.387907304067	-0.387907304067	0.836095596749	0.0250712367487

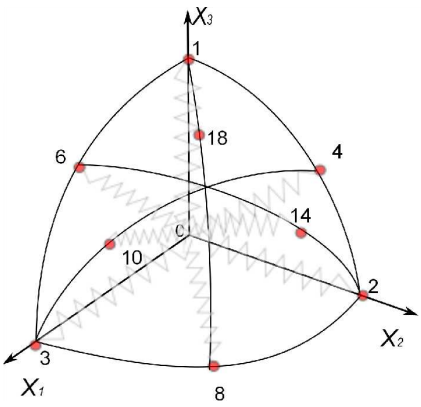

Figure A.1: The material directions construction. The set of direction $\mathbf{a}_0^{(i)}$ is defined by the polyhedron vertices.

Appendix

B Stress softening and Shear tests

This appendix presents an application of the model presented in Chapter 2 to take into account the stress softening and the induced anisotropy for a simple shear test. In this way, an experimental dual shear test was carried out on a Natural Rubber (NR) at the Trellborg Company. This test is represented in Fig.B.1. The gradient of deformation $\mathbf{F}$

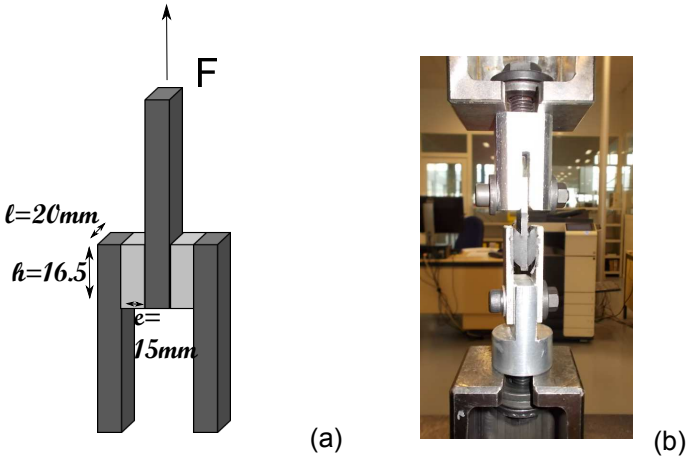

Figure B.1: Quad shear test performed on a Natural Rubber (a) dimension and (b) picture.

and the stress tensor $\boldsymbol{\pi}$ for a shear test are given by:

$$\mathbf{F} = \begin{pmatrix} 1 & \gamma & 0 \\ 0 & 1 & 0 \\ 0 & 0 & 1 \end{pmatrix} \tag{B.1}$$

$$\boldsymbol{\pi} = \begin{pmatrix} \tau_x & \tau_{xy} & 0 \\ \tau_{yx} & \tau_y & \\ 0 & 0 & \tau_z \end{pmatrix} \tag{B.2}$$

where γ represents the shear strain. It is known that the shear stress for a simple shear test is given by:

$$\tau_{xy} = \frac{F/2}{h.l} \tag{B.3}$$

Where F is the applied force, h the height of the sample and l its length (as represented in Fig.B.1). As presented in literature by Charlton *et al.* [1994]; Chagnon [2003], a simple shear test is equivalent to pure shear test. In this way, the expression of the principal elongation λ and of the stress for π_{ps} for the pure shear test can be deduced by means of few calculation (eigenvalues and changed of framework) such as:

$$\lambda = 1 + \frac{\gamma^2}{2} + \gamma\sqrt{1 + \frac{\gamma^2}{4}} \tag{B.4}$$

$$\tau_{xy} = \frac{\pi_{ps}}{2\sqrt{1 + \frac{\gamma^2}{4}}} \tag{B.5}$$

The comparison between the experimental data and the model is presented in Fig.B.2. It appears that the model presented in Chapter 2 is also efficient to take into account a dual shear test. The material parameter used for the modeling are: C1=0.6MPa, C2=0.5MPa, K=1.3MPa, η=6.

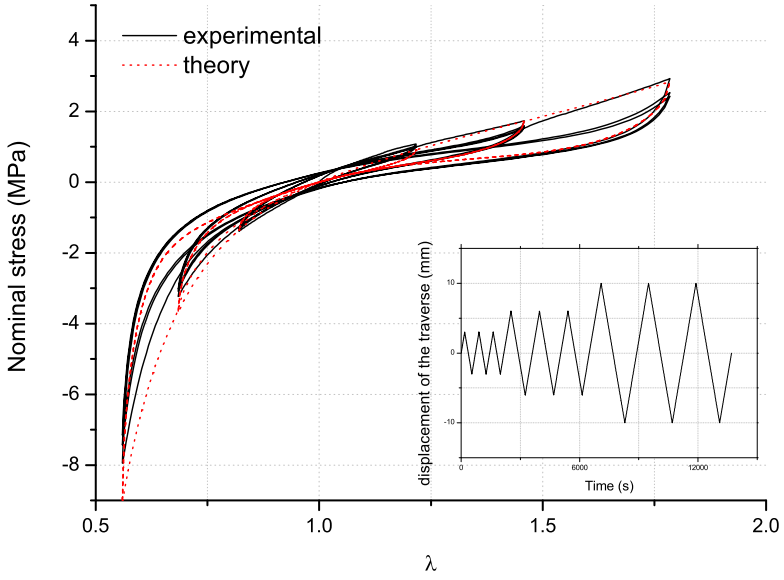

Figure B.2: Comparison of experimental data between the experimental test of quad shear test (black line) equivalent to planar tension and a simulation of the model in planar tension (red dotted line)

Bibliography

Abaqus (2002). *Theory Manual, ver 6.2.* HKS.

Abraham, A. C., Moyer, J. T., Villegas, D. F., Odegard, G. M., and Haut Donahue, T. L. (2011). Hyperelastic properties of human meniscal attachments. *J. Biomech.*, **4**4, 413–418.

Alastrué, V., Peña, E., Martinez, M. A., and Doblaré, M. (2008). Experimental study and constitutive modelling of the passive mechanical properties of the ovine infrarenal vena cava tissue. *J. Biomech.*, **4**1, 3038–3045.

Alastrué, V., Martinez, M. A., Doblaré, M., and Menzel, A. (2009). Anisotropic microsphere-based finite elasticity applied to blood vessel modelling. *J. Mech. Phys. Solids*, **5**7, 178–203.

Amin, A. F. M. S., Lion, A., Sekita, S., and Okui, Y. (2006). Nonlinear dependence of viscosity in modeling the rate-dependent response of natural and high damping rubbers in compression and shear: experimental identification and numerical verification. *Int. J. Plast.*, **2**2, 1610–1657.

Arruda, E. M. and Boyce, M. C. (1993). A three dimensional constitutive model for the large stretch behavior of rubber elastic materials. *J. Mech. Phys. Solids*, **4**1(2), 389–412.

Ashby, M. (2013). Designing architectured materials. *Scripta Mater.*, **6**8, 4 – 7.

Ayoub, G., Zairi, F., Nait-Abdelaziz, M., Gloaguen, J., and Kridli, G. (2014). A visco-hyperelastic damage model for cyclic stress-softening, hysteresis and permanent set in rubber using the network alteration theory. *Int. J. Plasticity*, **5**4, 19 – 33.

Azar, F. S., Metaxas, D. N., and Schnall, M. D. (2001). A deformable finite element model of the breast for predicting mechanical deformations under external perturbations. *Acad. Radiol.*, **8**, 965–975.

Basciano, C. A. and Kleinstreuer, C. (2009). Invariant-based anisotropic constitutive models of the healthy and aneurysmal abdominal aortic wall. *J. Biomech. Eng. ASME*, **1**31, 1–11.

Bazant, Z. P. and Oh, B. H. (1986). Efficient numerical integration on the surface of a sphere. *Z. Angew. Math. Mech.*, **6**6, 37–49.

Bergstrom, J. S. and Boyce, M. C. (1998). Constitutive modeling of the large strain time dependant behavior of elastomers. *J. Mech. Phys. Solids*, **4**6(5), 931–954.

Bergstrom, J. S. and Boyce, M. C. (2001). Constitutive modeling of the time-dependent and cyclic loading of elastomers and application to soft biological tissues. *Mech. Mater.*, **3**3, 523–530.

Berstein, B., Kearsley, E. A., and Zapas, L. J. (1963). A study of stress relaxation with finite strain. *Trans. Soc. Rheol.*, **7**, 391–410.

Besdo, D. and Ihlemann, J. (2003). Properties of rubber like materials under large deformations explained by self-organizing linkage patterns. *Int. J. Plast.*, **1**9, 1001–1018.

Bischoff, J. E., Arruda, E. M., and Grosh, K. (2002). A microstructurally based orthotropic hyperelastic constitutive law. *J. Appl. Mech. Trans. ASME*, **6**9, 570–579.

Bonet, J. and Burton, A. J. (1998). A simple orthotropic, transversely isotropic hyperelastic constitutive equation for large strain computations. *Comput. Methods Appl. Mech. Engrg.*, **1**62, 151–164.

Bose, K. and Dorfmann, A. (2009). Computational aspects of a pseudo-elastic constitutive model for muscle properties in a soft-bodied arthropod. *Int. J. Non-Linear Mech.*, **4**4, 42–50.

Bouasse, H. and Carrière, Z. (1903). Courbes de traction de caoutchouc vulcanisé. *Ann. Fac. Sciences de Toulouse*, **5**, 257–283.

Bouaziz, O. (2013). Geometrically induced strain hardening. *Scripta Mater.*, **6**8, 28 – 30.

Bouaziz, O., Brechet, Y., and Embury, J. D. (2008). Heterogeneous and architectured materials: a possible strategy for design of structural materials. *Adv. Engrg. Mater.*, **1**0, 24–36.

Boubaker, M. B., Haboussi, M., Ganghoffer, J. F., and Aletti, P. (2009). Finite element simulation of interactions between pelvic organs: predictive model of the prostate motion in the context of radiotherapy. *J. Biomech.*, **4**2, 1862–1868.

Boyce, M. C. and Arruda, E. M. (2000). Constitutive models of rubber elasticity: a review. *Rubber Chem. Technol.*, **7**3, 504–523.

Brechet, Y. and Embury, J. (2013). Architectured materials: Expanding materials space. *Scripta Mater.*, **6**8, 1 – 3.

Bueche, F. (1960). Molecular basis for the Mullins effect. *J. Appl. Polym. Sci.*, **3**(10), 107–114.

Calvo, B., Peña, E., Martins, P., Mascarenhas, T., Doblaré, M., Natal Jorge, R. M., and Ferreira, A. (2009). On modelling damage process in vaginal tissue. *J. Biomech.*, **4**2, 642–651.

Cantournet, S., Desmorat, R., and Besson, J. (2009). Mullins effect and cyclic stress softening of filled elastomers by internal sliding and friction thermodynamics model. *Int. J. Solids Struct.*, **4**6, 2255 – 2264.

Chagnon, G. (2003). *Modélisation de l'effet Mullins dans les élastomères*. Ph.D. thesis, Ecole Centrale de Nantes.

Chagnon, G., Verron, E., Gornet, L., Marckmann, G., and Charrier, P. (2004). On the relevance of continuum damage mechanics as applied to the Mullins effect: theory, experiments and numerical implementation. *J. Mech. Phys. Solids*, **5**2, 1627–1650.

Chagnon, G., Verron, E., Marckmann, G., and Gornet, L. (2006). Development of new constitutive equations for Mullins effect in rubber using the network alteration theory. *Int. J. Solids Struct.*, **4**3, 6817–6831.

Chagnon, G., Rebouah, M., and Favier, D. (2014). Hyperelastic energy densities for soft tissues: a review. *J. Elasticity*, **s**ubmitted.

Charlton, D. J., Yang, J., and Teh, K. K. (1994). A review of methods to characterize rubber elastic behavior for use in finite element analysis. *Rubber Chem. Technol.*, **6**7, 481–503.

Cheng, T. and Gan, R. Z. (2008). Mechanical properties of anterior malleolar ligament from experimental measurement and material modeling analysis. *Biomech. Model. Mechanobiol.*, **7**, 387–394.

Choi, H. S. and Vito, R. P. (1990). Two-dimensional stress-strain relationship for canine pericardium. *J. Biomech. Engr*, **1**12, 153–159.

Christensen, R. M. (1980). A nonlinear theory of viscoelasticity for application to elastomers. *J. Appl. Mech.*, **4**7(4), 762–768.

Chuong, C. J. and Fung, Y. C. (1983). Three-dimensional stress distribution in arteries. *J. Biomech. Engrg*, **1**05(3), 268–274.

Coleman, B. D. and Gurtin, M. E. (1967). Thermodynamics with internal state variables. *J. Chem. Phys.*, **4**7, 597–613.

Coleman, B. D. and Noll, W. (1961). Foundations of linear viscoelasticity. *Rev. Mod. Phys.*, **3**3, 239–249.

Coleman, B. D. and Noll, W. (1963). The thermodynamics of elastic materials with heat conduction and viscosity. *Arch. Ration. Mech. Anal.*, **1**3, 167–178.

Costa, K. D., Hunter, P. J., Waldman, L. K., Guccione, J. M., and McCulloc, A. (1996). A three-dimensional finite element method for large elastic deformations of ventricular myocardium: part II - prolate-spherical coordinates. *J. Biomech. Eng.*, **1**18, 464–472.

Dal, H. and Kaliske, M. (2009). Bergström - Boyce model for nonlinear finite rubber viscoelasticity: theoretical aspects and algorithmic treatment for the FE method. *Comput Mech*, **4**4, 809–823.

Dannenberg, E. M. (1974). The effects of surface chemical intercations on the properties of filled-reinforced rubbers. *Rubber Chem. Technol.*, **4**8, 410–444.

Dargazany, R. and Itskov, M. (2009). A network evolution model for the anisotropic Mullins effect in carbon black filled rubbers. *Int. J. Solids Struct.*, **4**6, 2967–2977.

De Tommasi, D., Puglisi, G., and Saccomandi, G. (2006). A micromechanics-based model for the Mullins effect. *J. Rheol.*, **5**0, 495–512.

Delfino, A., Stergiopulos, N., Moore Jr, J. E., and Meister, J. J. (1997). Residual strain effects on the stress field in a thick wall finite element model of the human carotid bifurcation. *J. Biomech.*, **3**0, 777–786.

Demiray, H. (1972). A note on the elasticity of soft biologicalt issues. *J. Biomech.*, **5**, 309–311.

DeSouza Neto, E. A., Djordje Peric, and Owen, D. R. J. (1994). A phenomenological three dimensional rate independent continuum damage model for highly filled polymers: formulation and computational aspects. *J. Mech. Phys. Solids.*, **4**2(10), 1533–1550.

Diani, J., Brieu, M., Vacherand, J. M., and Rezgui, A. (2004). Directional model isotropic and anisotropic hyperelastic rubber-like materials. *Mech. Mater.*, **3**6, 313–321.

Diani, J., Brieu, M., and Vacherand, J. M. (2006a). A damage directional constitutive model for the Mullins effect with permanent set and induced anisotropy. *Eur. J. Mech. A/Solids*, **2**5, 483–496.

Diani, J., Brieu, M., and Gilormini, P. (2006b). Observation and modeling of the anisotropic visco-hyperelastic behavior of a rubberlike material. *Int. J. Solids Struct.*, **4**3, 3044–3056.

Diani, J., Fayolle, B., and Gilormini, P. (2009). A review on the Mullins effect. *Eur. Polym. J.*, **4**5, 601612.

Diani, J., Gilormini, P., Merckel, Y., and Vion-Loisel, F. (2013). Micromechanical modeling of the linear viscoelasticity of carbon-black filled styrene butadiene rubbers: The role of the fillers rubber interphase. *Mech. Mater.*, **5**9, 65 – 72.

Doi, M. and Edwards, S. F. (1986). *The theory of polymer dynamics*. Oxford University Press, New-York.

Dorfmann, A. and Ogden, R. W. (2004). A constitutive model for the Mullins effect with permanent set in particule-reinforced rubber. *Int. J. Solids Struct.*, **4**1, 1855–1878.

Dorfmann, A. and Pancheri, F. (2012). A constitutive model for the Mullins effect with changes in material symmetry. *Int. J. Solid Struct.*, **4**7, 874 – 887.

Dunlop, J. W. and Fratzl, P. (2013). Multilevel architectures in natural materials. *Scripta Mater.*, **6**8, 8 – 12.

Ehret, A. E. and Itskov, M. (2009). Modeling of anisotropic softening phenomena: application to soft biological tissues. *Int. J. Plast.*, **2**5, 901–919.

Epstein, E. and Munderloh, N. (1975). Isolation and characterisation of cnbr peptides of human $[\alpha_1(III)]_3$ collagen and tissue distribution $[\alpha_1(I)]_2\alpha_2$ and $[\alpha_1(III)]_3$ collagen. *J. Biol. Chem*, **2**50, 9304–12.

Federico, S., Grillo, A., Imatani, S., Giaquinta, G., and Herzog, W. (2008). An energetic approach to the analysis of anisotropic hyperelastic materials. *Int. J. Eng. Sci.*, **4**6, 164–181.

Flory, P. J. (1944). Network structure and the elastic properties of vulcanized rubber. *Chem. Rev.*, **3**5, 51–75.

Franceschini, G., Bigoni, D., Regitnig, P., and Holzapfel, G. A. (2006). Brain tissue deforms similarly to filled elastomers and follows consolidation theory. *J. Mech. Phys. Solids*, **5**4, 2592–2620.

Fung, Y. C. (1993). *Biomechanics, Mechanical properties of living tissues*. Springer, New York, 2nd edition edition.

Fung, Y. C., Fronek, K., and Patitucci, P. (1979). Pseudoelasticity of arteries and the choice of its mathematical expression. *Am. Phys/ Soc.*, **2**37, H620–H631.

Gasser, T. C., Ogden, R. W., and Holzapfel, G. A. (2006). Hyperelastic modelling of arterial layers with distributed collagen fibre orientations. *J. R. Soc. Interface*, **3**, 15–35.

Gillibert, J., Brieu, M., and Diani, J. (2010). Anisotropy of direction-based constitutive models for rubber-like materials. *Int. J. Solids Struct.*, **4**7, 640 – 646.

Göktepe, S. and Miehe, C. (2005). A micro-macro approach to rubber-like materials. Part III: The micro-sphere model of anisotropic Mullins-type damage. *J. Mech. Phys. Solids*, **5**3, 2259–2283.

Göktepe, S., S. N. S. Acharya, J. W., and Kuhl, E. (2010). Computational modeling of passive myocardium. *Int. J. Numer. Meth. Biomed. Engng.*, **2**7, 1–12.

Govindjee, S. and Simo, J. C. (1991). A micro-mechanically continuum damage model for carbon black filled rubbers incorporating Mullins effect. *J. Mech. Phys. Solids*, **3**9, 87–112.

Govindjee, S. and Simo, J. C. (1992). Mullins effect and the strain amplitude dependence of the storage modulus. *Int. J. Solids. Struct.*, **2**9(14-15), 1737–1751.

Gracia, L. A., Peña, E., Royo, J. M., Pelegay, J. L., and Calvo, B. (2009). A comparison between pseudo-elastic and damage models for modelling the Mullins effect in industrial rubber components. *Mech. Res. Comm.*, **3**6, 769 – 776.

Gras, L.-L., Mitton, D., Viot, P., and Laporte, S. (2012). Hyperelastic properties of the human sternocleidomastoideus muscle in tension. *J. Mech. Behav. Biomed. Mater.*, **1**5, 131 – 140.

Green, A. and Rivlin, R. (1957). The mechanics of non-linear materials with memory; Part I. *Arch. Ration. Mech. Anal.*, **1**, 1–21.

Green, M. S. and Tobolsky, A. V. (1946). A new approach for the theory of relaxing polymeric media. *J. Chem. Phys.*, **1**4, 87–112.

Groves, R. B., Coulman, S. A., Birchall, J. C., and Evans, S. L. (2013). An anisotropic, hyperelastic model for skin: experimental measurements, finite element modelling and identification of parameters for human and murine skin. *J. Mech. Behav. Biomed. Mater.*, **1**8, 167 – 180.

Guo, Z. Y., Peng, X. Q., and Moran, B. (2006). A composites-based hyperelastic constitutive model for soft tissue with application to the human annulus fibrosus. *J. Mech. Phys. Solids*, **5**4, 1952–1971.

Gurtin, M. E. and Francis, E. C. (1981). Simple rate-independent model for damage. *J. Spacecraft*, **1**8(3), 285–286.

Guth, E. and Mark, J. E. (1934). Zur innermoleckularen statistik, insbesondere bei kettenmolekülen I. *Monatsh Chem.*, **6**5, 93–121.

Hanson, D. E., Hawley, M., Houlton, R., Chitanvis, K., Rae, P., Orler, E. B., and Wrobleski, D. A. (2005). Stress softening experiments in silica-filled polydimethylsiloxane provide insight into a mechanism for the Mullins effect. *Polymer*, **4**6, 10989–10995.

Harwood, J. A. C. and Payne, A. R. (1966). Stress softening in natural rubber vulcanizates. part 4. unfilled vulcanizates. *J. Appl. Polym. Sci.*, **1**0, 1203–1211.

Harwood, J. A. C., Mullins, L., and Payne, A. R. (1965). Stress softening in natural rubber vulcanizates. Part 2. Stress softening effects in pure gum and filler loaded rubbers. *J. Appl. Polym. Sci.*, **9**, 3011–3021.

Haupt, P. and Sedlan, K. (2001). Viscoplasticity of elastomeric materials: experimental facts and constitutive modelling. *Arch. Appl. Mech.*, **7**1, 89–109.

Heinrich, K. and Kaliske, M. (1997). Theoretical and numerical formulation of a molecular based constitutive tube model of rubber elasticity. *Comput. Theor. Polym. Sci.*, **7**(3-4), 227–241.

Holzapfel, G. A. (2000). *Nonlinear solid mechanics - A continuum approach for engineering.* John Wiley and Sons, LTD.

Holzapfel, G. A. and Gasser, T. C. (2001). A viscoelastic model for fiber-reinforced composites at finite strains: continuum basis, computational aspects and applications. *Comput. Methods Appl. Mech. Engrg*, **1**90, 4379–4403.

Holzapfel, G. A. and Simo, J. C. (1996). A new viscoelastic constitutive model for continuous media at finite thermomechanical changes. *Int. J. Solids Struct.*, **3**3, 3019–3034.

Holzapfel, G. A., Gasser, T. C., and Ogden, R. W. (2000). A new constitutive framework for arterial wall mechanics and a comparative study of material models. *J. Elast.*, **6**1, 1–48.

Holzapfel, G. A., Stadler, M., and Schulze-Bauer, C. A. J. (2002). A layer-specific three-dimensional model for the simulation of balloon angioplasty using magnetic resonance imaging and mechanical testing. *Annals. Biomed. Engrg.*, **3**0, 752–767.

Horgan, C. O. and Saccomandi, G. (2005). A new constitutive theory for fiber-reinforced incompressible nonlinearly elastic solids. *J. Mech. Phys. Solids*, **5**3, 1985–2015.

Hostettler, A., George, D., Rémond, Y., Nicolau, S. A., Soler, L., and Marescaux, J. (2010). Bulk modulus and volume variation measurement of the liver and the kidneys in vivo using abdominal kinetics during free breathing. *Comput. Meth. Prog. Biomed.*, **1**00, 149–157.

Huber, A. and Tsakmakis, C. (2000). Finite deformation viscoelasticity laws. *Mech. Mater.*, **3**2, 1–18.

Humphrey, J. D. (2002). *Cardiovascular solid mechanics. Cells, Tissues and Organs.* Springer, New York.

Humphrey, J. D. and Yin, F. C. P. (1987). On constitutive relations and finite deformations of passive cardiac tissue: I. a pseudo strain-energy approach. *ASME J. Biomech. Engrg.*, **1**09, 298–304.

Itskov, M., Haberstroh, E., Ehret, A. E., and Vohringer, M. C. (2006). Experimental observation of the deformation induced anisotropy of the Mullins effect in rubber. *KGK-Kaut. Gummi Kunst.*, **5**9(3), 93–96.

Itskov, M., Ehret, A., Kazakeviciute-Makovska, R., and Weinhold, G. (2010). A thermodynamically consistent phenomenological model of the anisotropic Mullins effect. *ZAMM - J. Appl. Math. Mech.*, **9**0, 370–386.

James, H. M. and Guth, E. (1943). Theory of the elastic properties of rubber. *J. Chem. Phys.*, **1**1, 455–481.

Jang, D., Meza, L. R., Greer, F., and Greer, J. R. (2013). Fabrication and deformation of three-dimensional hollow ceramic nanostructures. *Nat. mater.*, **1**2, 893–898.

Kaliske, M. (2000). A formulation of elasticity and viscoelasticity for fibre reinforced material at small and finite strains. *Comput. Methods Appl. Mech. Engrg*, **1**85, 225–243.

Kaliske, M. and Rothert, H. (1998). Constitutive approach to rate independent properties of filled elastomers. *Int. J. Solids. Struct.*, **3**5, 2057–2071.

Kaliske, M., Nasdala, L., and Rothert, H. (2001). On damage modelling for elastic and viscoelastic materials at large strain. *Comput. Struct.*, **7**9, 2133–2141.

Kaster, T., Sack, I., and Samani, A. (2011). Measurement of the hyperelastic properties of ex vivo brain tissue slices. *J. Biomech.*, **4**4, 1158–1163.

Kluppel, M. and Schramm, J. (2000). A generalized tube model of rubber elasticity and stress softening of filled reinforced elastomers systems. *Macromol. Theor. Sim.*, **9**, 742–754.

Kroon, M. and Holzapfel, G. A. (2008). A new constitutive model for multilayered collagenous tissues. *J. Biomech.*, **4**1, 2766–2771.

Kuhl, E., Garikipati, K., Arruda, E. M., and Grosh, K. (2005). Remodeling of biological tissue: mechanically induced reorientation of atransversely isotropic chain network. *J. Mech. Phys. Solids*, **5**3, 1552–1573.

Kuhn, W. and Grün, F. (1942). Beziehunger zwichen elastischen konstanten und dehnungsdoppelbrechung hochelastischerstoffe. *Kolloideitschrift*, **1**01, 248–271.

Lakes, R. (1993). Materials with structural hierarchy. *Nature*, **3**61, 511–515.

Lanir, Y. (1979). A structural theory for the homogeneous biaxial stress-strain relationshipin flat collagenous tissues. *J. Biomech.*, **1**2, 423–436.

Lanir, Y. (1983). Constitutive equations for fibous connective tissues. *J. Biomech.*, **1**6, 1–12.

Laraba-Abbes, F. (1998). *Comportements hyperélastique et viscoélastique de deux élastomères de deux types NR et PDMS par extensométrie Optique bidimensionnelle*. Ph.D. thesis, Ecole Centrale de Paris.

Laraba-Abbes, F., Ienny, P., and Piques, R. (2003). A new Taylor-made methodology for the mechanical behaviour analysisof rubber like materials: II. application of the hyperelastic behaviour characterization of a carbon-black filled natural rubber vulcanizate. *Polymer*, **4**4, 821–840.

Li, D. and Robertson, A. M. (2009). A structural multi-mechanism constitutive equation for cerebral arterial tissue. *Int. J. Solid Struct.*, **4**6, 2920 – 2928.

Li, W., Hill, N., Ogden, R., Smythe, A., Majeed, A., Bird, N., and Luo, X. (2013). Anisotropic behaviour of human gall bladder walls. *J. Mech. Beh. Biomed. Mater.*, **2**0, 363 – 375.

Li, Z. and Kleinstreuer, C. (2006). Analysis of biomechanical factors affecting stent-graft migration in an abdominal aortic aneurysm model. *J. Biomech.*, **3**9, 2264–2273.

Limbert, G., Taylor, M., and Middleton, J. (2004). Three-dimensional finite element modelling of the human ACL: simulation of passive knee flexion with a stressed and stress-free ACL. *J. Biomech.*, **3**7, 1723–1731.

Lion, A. (1996). A constitutive model for carbon black filled rubber: Experimental investigations and mathematical representation. *Continuum Mech. Thermodyn.*, **8**, 153–169.

Lion, A. (1997a). On the large deformation behaviour of reinforced rubber at different temperatures. *J. Mech. Phys. Solids*, **4**5(11-12), 1805–1834.

Lion, A. (1997b). A physically based method to represent the thermo-mechanical behavior of elastomers. *Acta Mech.*, **1**23, 1–25.

Lion, A., Diercks, N., and Caillard, J. (2013). On the directional approach in constitutive modelling: a general thermomechanical framework and exact solutions for Mooney Rivlin type elasticity in each direction. *Int. J. Solid Struct.*, **5**0, 2518 – 2526.

Lister, K., Gao, Z., and Desai, J. P. (2011). Development of in vivo constitutive models for liver: application to surgical simulation. *Ann. Biomed. Eng.*, **3**9, 1060–1073.

Lubliner, J. (1985). A model of rubber viscoelasticity. *Mech. Research Comm.*, **1**2, 93–99.

Machado, G. (2011). *Contribution à l'étude de l'anisotropie induite par l'effet Mullins dans les élastoméres silicones chargés*. Ph.D. thesis, Université de Grenoble.

Machado, G., Chagnon, G., and Favier, D. (2010). Analysis of the isotropic models of the Mullins effect based on filled silicone rubber experimental results. *Mech. Mater.*, **4**2, 841–851.

Machado, G., Favier, D., and Chagnon, G. (2012a). Determination of membrane stress-strain full fields of bulge tests from SDIC measurements. Theory, validation and experimental results on a silicone elastomer. *Exp. Mech.*, **5**2, 865–880.

Machado, G., Chagnon, G., and Favier, D. (2012b). Induced anisotropy by the Mullins effect in filled silicone rubber. *Mech. Mater*, **5**0(0), 70 – 80.

Machado, G., Chagnon, G., and Favier, D. (2014). Theory and identification of a constitutive model of induced anisotropy by the Mullins effect. *J. Mech. Phys. Solids*, **6**3, 29 – 39.

Maher, E., Creane, A., Lally, C., and Kelly, D. J. (2012). An anisotropic inelastic constitutive model to describe stress softening and permanent deformation in arterial tissue. *J. Mech. Behav. Biomed. Mater.*, **1**2, 9 – 19.

Marckmann, G. and Verron, E. (2006). Comparison of hyperelastic models for rubber-like materials. *Rubber Chem. Technol.*, **7**9, 835–858.

Marckmann, G., Verron, E., Gornet, L., Chagnon, G., Charrier, P., and Fort, P. (2002). A theory of network alteration for the Mullins effect. *J. Mech. Phys. Solids.*, **5**0, 2011–2028.

Marieb, E. and Hoehn, K. (2010). *Human Anatomy & Physiology*. Pearson Education.

Mayer, J. and Mayer, M. (1940). *Statistical Mechanics*, **J**onh Wiley and Sons edition.

Menzel, A. and Steinmann, P. (2001). permanent set in vulcanized rubber. *Int. J. Solid Struct.*, **3**8, 9505–9523.

Merckel, Y. (2012). *Experimental characterization and modeling of the mechanical behavior of filled rubbers under cyclic loading conditions*. Ph.D. thesis, Ecole centrale de Lille.

Merckel, Y., Diani, J., Roux, S., and Brieu, M. (2011). A simple framework for full-network hyperelasticity and anisotropic damage. *J. Mech. Phys. Solids*, **5**9, 75 – 88.

Merckel, Y., Brieu, M., Diani, J., and Caillard, J. (2012). A Mullins softening criterion for general loading conditions. *J. Mech. Phys. Solids*, **6**0, 1257 – 1264.

Merckel, Y., Diani, J., Brieu, M., and Caillard, J. (2013). Constitutive modeling of the anisotropic behavior of Mullins softened filled rubbers. *Mech. Mater*, **5**7, 30 – 41.

Merodio, J. and Ogden, R. W. (2005). Mechanical response of fiber-reinforced incompressible non-linearly elastic solids. *Int. J. Non-linear Mech.*, **4**0, 213–227.

Meunier, L. (2011). *Contribution à la conception, l'expérimentation et la modélisation de membranes hyperélastiques architecturées anisotropes*. Ph.D. thesis, Université de Grenoble.

Meunier, L., Chagnon, G., Favier, D., Orgéas, L., and Vacher, P. (2008). Mechanical experimental characterisation and numerical modelling of an unfilled silicone rubber. *Polym. Test.*, **2**7, 765–777.

Miehe, C. (1995). Discontinuous and continuous damage evolution in Ogden type large strain elastic materials. *Eur. J. Mech., A/Solids*, **1**4, 697–720.

Miehe, C. and Göktepe, S. (2005). A micro-macro approach to rubber-like materials. Part II: The micro-sphere model of finite rubber viscoelasticity. *J. Mech. Phys. Solids*, **5**3, 2231–2258.

Miehe, C. and Keck, J. (2000). Superimposed finite elastic-viscoelastic-plastoelastic stress response with damage in filled rubbery polymers. Experiments, modelling and algorithmic implementation. *J. Mech. Phys. Solids*, **4**8, 323–365.

Miehe, C., Göktepe, S., and Lulei, F. (2004). A micro-macro approach to rubber-like materials - Part I: the non-affine micro-sphere model of rubber elasticity. *J. Mech. Phys. Solids*, **5**2, 2617–2660.

Miller, K. (2000). Constitutive modeling of abdominal organs. *J. Biomech.*, **3**3, 367–373.

Miller, K. and Chinzei, K. (1997). Constitutive modelling of brain tissue: Experiment and theory. *J. Biomech.*, **3**0, 1115 – 1121.

Mooney, M. (1940). A theory of large elastic deformation. *J. Appl. Phys.*, **1**1, 582–592.

Muhr, A. H., Gough, J., and Gregory, I. H. (1999). Experimental determination of model for liquid silicone rubber: Hyperelasticity and Mullins effect. In *Proceedings of the First European Conference on Constitutive Models for Rubber*, pages 181–187.

Mullins, L. (1948). Effect of stretching on the properties of rubber. *Rubber Chem. Technol.*, **2**1, 281–300.

Mullins, L. (1969). Softening of rubber by deformation. *Rubber Chem. Technol.*, **4**2, 339–362.

Mullins, L. and Tobin, N. R. (1957). Theoretical model for the elastic behavior of filler-reinforced vulcanized rubbers. *Rubber Chem. Technol.*, **3**0, 551–571.

Natali, A. N., Pavan, P. G., Carniel, E. L., and Dorow, C. (2003). A transversally isotropic elasto-damage constitutive model for the peridontal ligament. *Comput. Methods Biomech. Biomed. Eng.*, **6**(5-6), 329–336.

Natali, A. N., Pavan, P. G., Carniel, E. L., Lucisano, M. E., and Taglialavoro, G. (2005). Anisotropic elasto-damage constitutive model for the biomechanical analysis of tendons. *Med. Engrg. Phys.*, **2**7, 209–214.

Natali, A. N., Carniel, E. L., and Gregersen, H. (2009). Biomechanical behaviour of oesophageal tissues: material and structural configuration, experimental data and constitutive analysis. *Med. Eng. & Phys.*, **3**1, 1056–1062.

Nerurkar, N. L., Mauck, R. L., and Elliott, D. M. (2011). Modeling interlamellar interactions in angle-ply biologic laminates for annulus fibrosus tissue engineering. *Biomech. Model. Mechan.*, **1**0, 973–984.

Ogden, R. W. (1972). Large deformation isotropic elasticity - on the correlation of theory and experiment for incompressible rubber like solids. *Proc. R. Soc. Lond. A*, **3**26, 565–584.

Ogden, R. W. (1997). *Non-linear Elastic Deformations*. Dover Publications, New York.

Ogden, R. W. (2003). *Nonlinear elasticity, anisotropy, material stability and residual stresses in soft tissue.*, chapter Holzapfel GA, Ogden RW (eds) Biomechanics of soft tissue in cardiovascular system. CISM Courses and lecture Series, vol 441. Springer, Wien New York.

Ogden, R. W. (2004). Mechanics of rubberlike solids. In *XXI ICTAM*, Warsaw, Poland.

Ogden, R. W. and Roxburgh, D. G. (1999). An energy based model of the Mullins effect. In Dorfmann & Muhr, editor, *Constitutive Models for Rubber I*. A. A. Balkema.

Papageorgiou, G. L. and Jones, N. B. (1988). Circumferential and longitudinal viscoelasticity of human iliac arterial segments in vitro. *J. Biomed. Eng.*, **1**0, 82–90.

Parente, M. P. L., Natal Jorge, R. M., Mascarenhas, T., Fernandes, A. A., and Martins, J. A. C. (2009). The influence of the material properties on the biomechanical behavior of the pelvic floor muscles during vaginal delivery. *J. Biomech.*, **4**2, 1301–1306.

Park, B. H. and Hamed, G. R. (2000). Anisotropy in gum and black filled SBR and NR vulcanizates due to large deformation. *Korea Polym. J.*, **8**, 268–275.

Passera, S., Baylòn, K., Fiorentino, A., Ceretti, E., Elías, A., and Rodrèguez, C. (2013). A preliminary material model to predict stress softening and permanent set effects of human vaginal tissue. *Proc. Eng.*, **5**9, 150 –157.

Pawelski, H. (2001). Softening behaviour of elastomeric media after loading in changing directions. *Constitutive models for rubber, Besdo, Schuster & Ihleman (eds)*, pages 27–34.

Peña, E. (2011). Prediction of the softening and damage effects with permanent set in fibrous biological materials. *J. Mech. Phys. Solids*, **5**9, 1808–1822.

Peña, E. and Doblaré, M. (2009). An anisotropic pseudo-elastic approach for modelling Mullins effect in fibrous biological materials. *Mech. Res. Comm.*, **3**6, 7847–90.

Peña, E., Calvo, B., Martinez, M. A., and Doblaré, M. (2007). An anisotropic visco-hyperelastic model for ligaments at finite strains. Formulation and computational aspects. *Int. J. Solids Struct.*, **4**4, 760–778.

Peña, E., Calvo, B., Martinez, M. A., and Doblaré, M. (2008). On finite strain damage of viscoelastic fibred materials. Application to soft biological tissues. *Int. J. Numer. Meth. Engrg*, **7**4, 1198–1218.

Peña, E., Peña, J. A., and Doblaré, M. (2009). On the Mullins effect and hysteresis of fibered biological materials: A comparison between continuous and discontinuous damage models. *Int. J. Solids Struct.*, **4**6, 1727–1735.

Peña, E., Calvo, B., Martínez, M. A., Martins, P., Mascarenhas, T., Natal Jorge, R. M., Ferreira, A., and Doblaré, M. (2010). Experimental study and constitutive modeling of the viscoelastic mechanical properties of the human prolapsed vaginal tissue. *Biomech. Model. Mechan.*, **9**, 35–44.

Peña, E., Martins, P., Mascarenhasd, T., Natal Jorge, R. M., Ferreirae, A., Doblaré, M., and Calvo, B. (2011). Mechanical characterization of the softening behavior of human vaginal tissue. *J. Mech. Beh. Biomed. Mater.*, **4**, 275–283.

Peng, X. Q., Guo, Z. Y., and Roman, B. (2006). An anisotropic hyperelastic constitutive model with fiber-matrix shear interaction for the human annulus fibrosus. *J. Appl. Mech. Trans ASME*, **7**3, 815–824.

Petiteau, J.-C., Verron, E., Othman, R., Sourne, H., Sigrist, J.-F., and Barras, G. (2012). Large strain rate-dependent response of elastomers at different strain rates: convolution integral vs. internal variable formulations. *Mech Time-Dep. Mat.*, pages 1–19.

Pinsky, P. M., van der Heide, D., and Chernyak, D. (2005). Computational modeling of mechanical anisotropy in the cornea and sclera. *J Cataract Refract Surg*, **3**1, 136–145.

Pioletti, D. P. and Rakotomanana, L. R. (2000). Non-linear viscoelastic laws for soft biological tissues. *Eur. J. Mech. A. Solids*, **1**9(5), 749 – 759.

Pioletti, D. P., Rakotomanana, L. R., Benvenuti, J.-F., and Leyvraz, P.-F. (1998). Viscoelastic constitutive law in large deformations: application to human knee ligaments and tendons. *J. Biomech.*, **3**1, 753–757.

Raghavan, M., Webster, M., and Vorp, D. (1996). Ex vivo biomechanical behavior of abdominal aortic aneurysm: assessment using a new mathematical model. *Ann. Biomed. Eng.*, **2**4(5), 573–582.

Raghupathy, R. and Barocas, V. H. (2009). A closed-form structural model of planar fibrous tissue mechanics. *J. Biomech.*, **4**2, 1424–1428.

Rebouah, M. (2011). Dispositif de gonflement de tube. Master's thesis, Université Joseph Fourier.

Rebouah, M. and Chagnon, G. (2014). Extension of classical viscoelastic models in large deformation to anisotropy and stress softening. *Int. J. non-linear Mech.*, **6**1(0), 54 – 64.

Rebouah, M. and Chagnon, G. (2013). Permanent set and stress-softening constitutive equation applied to rubber-like materials and soft tissues. *Acta Mechanica*, **2**24, 1–14.

Rebouah, M., Machado, G., Chagnon, G., and Favier, D. (2013). Anisotropic Mullins stress softening of a deformed silicone holey plate. *Mech. Res. Commun.*, **4**9, 36 – 43.

Reese, S. and Govindjee, S. (1998). A theory of finite viscoelasticity and numerical aspects. *Int. J. Solids Struct.*, **3**5(26-27), 3455–3482.

Reese, S. and Wriggers, P. (1997). Material instabilities of an incompressible elastic cube under triaxial tension. *Int. J. Solids Struct.*, **3**4(26), 3433–3454.

Reese, S., Raible, T., and Wriggers, P. (2001). Finite element modelling of orthotropic material behaviour in pneumatic membranes. *Int. J. Solids Struct.*, **3**8, 9525–9544.

Rey, T., Chagnon, G., Le Cam, J.-B., and Favier, D. (2013). Influence of the temperature on the mechanical behaviour of filled and unfilled silicone rubbers. *Polym. Test.*, **3**2(3), 492 – 501.

Rey, T., Chagnon, G., Favier, D., and Cam, J.-B. L. (2014). Hyperelasticity with rate-independent microsphere hysteresis model for rubberlike materials. *Comp. Mat. Sci.*, **9**0, 89 – 98.

Rhodin, J. (1980). Architecture of the vessel wall. in H.V. Sparks Jr., D.F. Bohr, A.D. Somlyo and S.R. Geiger (eds). *Handbook of Physiology, The Cardiovascular System*, **2**, 1–31.

Rickaby, S. and Scott, N. (2013). A cyclic stress softening model for the Mullins effect. *Int. J. Solid Struct.*, **5**0(1), 111 – 120.

Rigbi, Z. (1980). Reinforcement of rubber by carbon black. *Adv. Polym. Sci.*, **3**6, 21–68.

Robisson, A. (2000). *Comportement mécanique d'un élastomère chargé en silice. Etude de l'influence des charges et modélisation par une loi visco-hyperélastique endommageable.* Ph.D. thesis, Ecole Nationale Supérieure des Mines de Paris.

Sarva, S. S., Deschanel, S., Boyce, M. C., and Chen, W. (2007). Stress strain behavior of a polyurea and a polyurethane from low to high strain rates. *Polymer*, **4**8(8), 2208 – 2213.

Schröder, J., Neff, P., and Balzani, D. (2005). A variational approach for materially stable anisotropic hyperelasticity. *Int. J. Solids. Struct.*, **4**2, 4352–4371.

Schwenninger, D., Schumann, S., and Guttmann, J. (2011). In vivo characterization of mechanical tissue properties of internal organs using endoscopic microscopy and inverse finite element analysis. *J.J. Biome.*, **4**4(3), 487 – 493.

Seibert, D. J. and Schöche, N. (2000). Direct comparison of some recent rubber elasticity models. *Rubber Chem. Technol.*, **7**3, 366–384.

Shariff, M. H. B. M. (2006). An anisotropic model of the Mullins effect. *J. Eng. Math.*, **5**6, 415–435.

Shin, T. J., Vito, R. P., Johnson, L. W., and McCarey, B. E. (1997). The distribution of strain in the human cornea. *J. Biomech.*, **3**0, 497–503.

Sidoroff, F. (1974). Un modèle viscoélastique non linéaire avec configuration intermédiaire. *J. Mec*, **1**3(4), 679–713.

Silver F.H., D. C. and Buntin, C. (1989). Mechanical properties of the aorta: a review. *Critical Reviews in Biomed. Engr*, **1**7, 323–358.

Simo, J. C. (1987). On a fully three-dimensional finite-strain viscoelastic damage model: formulation and computational aspects. *Comp. Meth. Appl. Mech. Engng*, **6**0, 153–173.

Spencer, A. J. M. (1971). *Theory of Invariants.* Continuum Physics, C. Eringen Academic Press.

Sun W, S. M. (2005). Finite element implementation of a generalized Fung-elastic constitutive model for planar soft tissues. *Biomech Model Mechan.*

Taylor, Z., Comas, O., Cheng, M., Passenger, J., Hawkes, D., Atkinson, D., and Ourselin, S. (2009). On modelling of anisotropic viscoelasticity for soft tissue simulation: numerical solution and GPU execution. *Med. Image Anal.*, **1**3, 234 – 244.

Tobolsky, A. V., Prettyman, I. B., and Dillon, J. H. (1944). Stress relaxation of natural and synthetic rubber stocks. *J. Appl. Phys.*, **1**5(4), 380–395.

Tong, P. and Fung, Y. C. (1976). The stress-strain relationship for the skin. *J. Biomech*, **9**, 649–657.

Trabelsi, O., Pérez del Palomar, A., López-Villalobos, J. L., Ginel, A., and Doblaré, M. (2010). Experimental characterization and constitutive modeling of the mechanical behavior of the human trachea. *Med. Eng. Phys.*, **3**2, 76–82.

Treloar, L. R. G. (1943). The elasticity of a network of long chain molecules (I and II). *Trans. Faraday Soc.*, **3**9, 36–64 ; 241–246.

Treloar, L. R. G. (1946). The statistical length of long-chain molecules. *Trans. Faraday Soc.*, **4**2, 77–82.

Treloar, L. R. G. and Riding, G. (1979). A non-Gaussian theory of rubber in biaxial strain. I. Mechanical properties. *Proc. R. Soc. Lond. A.*, **3**69, 261–280.

Triantafyllidis, N. and Abeyaratne, R. C. (1983). Instability of a finitely deformed fiber-reinforced elastic material. *J. Appl. Mech.*, **5**0, 149156.

Vahapoglu, V. and Karadeniz, S. (2006). Constitutive equations for isotropic rubber-like materials using phenomenological approach: a bibliography (1930-2003). *Rubber Chem. Technol.*, **7**9, 489–499.

Vande Geest, J. P., Sacks, M. S., and Vorp, D. A. (2006). The effects of aneurysm on the biaxial mechanical behavior of human abdominal aorta. *J. Biomech.*, **3**9, 1324–1334.

Weiss, J. A., Maker, B. N., and Govindjee, S. (1996). Finite implementation of incompressible, transversely isotropic hyperelasticity. *Comput. Methods Appl. Mech. Engrg.*, **1**35, 107–128.

Wu, P. D. and Giessen, E. V. D. (1993). On improved network models for rubber elasticity and their applications to orientation hardening in glassy polymers. *J. Mech. Phys. Solids*, **4**1(3), 427–456.

Yi, J., Boyce, M. C., Lee, G. F., and Balizer, E. (2006). Large deformation rate-dependent stress-strain behavior of polyurea and polyurethanes. *Polymer*, **4**7, 319–329.

Zapas, L. and Craft, T. (1965). Correlation of large longitudinal deformations with different strain histories. *Res. Natl. Bur. Stand*, **6**9A, 541–546.

Zuñiga, A. E. and Beatty, M. F. (2002a). Constitutive equations for amended non-gaussian network models of rubber elasticity. *Int. J. Eng. Sci.*, **4**0, 2265–2294.

Zuñiga, A. E. and Beatty, M. F. (2002b). A new phenomenological model for stress-softening in elastomers. *Z. Angew. Math. Phys.*, **5**3, 794–814.

Zulliger, M. A., Fridez, P., Hayashi, K., and Stergiopulos, N. (2004). A strain energy function for arteries accounting for wall composition and structure. *J. Biomech.*, **3**7, 989–1000.